

**THREE DIMENSIONAL RECONSTRUCTION OF PLANT ROOTS
VIA LOW ENERGY X-RAY COMPUTED TOMOGRAPHY**

A Thesis presented to
the Faculty of the Graduate School
at the University of Missouri

In Partial Fulfillment
of the Requirements for the Degree
Master of Science

by
Shashank Chary Avusali
Dr. Alina Zare, Thesis Supervisor
JULY 2018

The undersigned, appointed by the Dean of the Graduate School, have examined
the thesis entitled:

THREE DIMENSIONAL RECONSTRUCTION OF PLANT ROOTS
VIA LOW ENERGY X-RAY COMPUTED TOMOGRAPHY

presented by Shashank Chary Avusali,
a candidate for the degree of Master of Science and hereby certify that, in their
opinion, it is worthy of acceptance.

Dr. Alina Zare

Dr. Scott Kovaleski

Dr. Felix Fritschi

ACKNOWLEDGMENTS

I would like to thank Dr. Alina Zare, my thesis advisor, who guided me by providing constructive criticism in the research directions, lab presentations.

I would like to thank my thesis committee, Dr. Scott Kovaleski, Dr. Felix Fritschi, for their help and invaluable suggestions, to further improve my research.

I would also like to thank Anand Seethepalli, who laid the foundation for this work, Isaac Zachary, who developed the X-ray system setup and collected data for this study.

I would also like to thank all of the TigerSense and GatorSense lab members, who helped me over the years. I am grateful for the knowledge that I gained through the weekly presentations.

Finally, I would like to express my most profound gratitude to my parents, family, and friends for their continuous motivation and support over the years of the study. Without their constant support, this study would not have been possible.

TABLE OF CONTENTS

ACKNOWLEDGMENTS	ii
LIST OF TABLES	v
LIST OF FIGURES	vi
ABSTRACT	xi
CHAPTER	
1 Introduction	1
1.1 Goal of the study	2
1.2 Assumptions	3
2 Literature Review	5
2.1 Studying root system architecture	5
2.1.1 Destructive methods	6
2.1.2 Non-destructive methods	6
2.2 Three-dimensional reconstruction	9
3 Image Segmentation	12
3.1 Evolutionary approach to root extraction	12
3.2 Matched-guided filtering	20
3.2.1 Two-dimensional matched filtering	20
3.2.2 Structure transferring	25
3.3 Multi-scale matched filtering	27
3.3.1 Beam hardening correction	27
3.3.2 Denoising	30
3.3.3 Segmentation	38

4 Three-dimensioinal Reconstruction	43
4.1 Cross-sectional slice generation	43
4.1.1 Radon transform	44
4.1.2 Fourier transform and Fourier-slice theorem	46
4.1.3 Filtered back projection	48
4.2 Three-dimensional model generation	50
5 Results and Analysis	51
5.1 Performance analysis	51
5.1.1 Air sample	52
5.1.2 Soil sample	59
5.2 Experiments	73
5.2.1 Changing angular resolution ($\Delta\theta$)	73
5.2.2 Changing filter length (L)	81
6 Summary and concluding remarks	93
BIBLIOGRAPHY	95

LIST OF TABLES

Table	Page
5.1 Contrast metrics	59
5.2 Performance metrics of multi-scale matched filtering on soil sample dataset.	67
5.3 Soil image segmentation performance metrics	67
5.4 Contrast measure obtained at various angular resolutions	75
5.5 Area under the ROC curve for the soil sample data obtained from the images enhanced through multi-scale matched filtering with the filter banks created at different angular resolution.	80
5.6 Contrast metrics between the root and non-root from the models obtained with various filter banks.	84
5.7 Contrast metric between root and adjacent non-root voxels measured at different values of L	85
5.8 Performance metrics of filter banks consisting of filters with various lengths.	88
5.9 Effect of filter length on rolling bottom soil images.	90
5.10 Effect of filter length on rolling bottom soil images.	91
5.11 Effect of filter length on filtered field soil images.	92

LIST OF FIGURES

Figure	Page
1.1 The purpose of the study is to generate a three-dimensional model from two-dimensional projections. (a) Two-dimensional image stack obtained from various view points. (b) Segmented image stack. (c) Three-dimensional model of the root system.	3
1.2 An example root image obtained through the lab built X-ray system.	4
3.1 Sine waves extraction using genetic algorithm.	13
3.2 Calculating a fitness score. (a) Binary image, E , generated for a random candidate wave. (b) Absolute residual intensity with random candidate wave. (c) Binary image, E , generated for an optimal wave obtained after 1000 generations. (d) Absolute residual intensity with optimal wave.	15
3.3 Sine waves extraction using genetic algorithm.	18
3.4 Result of segmentation through sine wave extraction.	19
3.5 A matched filter with $\sigma = 10$ and $L = 11$ visualized in three-dimensional space	22
3.6 Matched filtering response for different orientational filters.	23
3.7 Orientational matched filtering a root image.	24
3.8 Binary mask obtained through thresholding.	25
3.9 Structure transferring using guided filter with $w = 21, \epsilon = 0.01^2$. . .	26

3.10	Plant root image captured in rolling bottom soil at 35keV	28
3.11	Intensity profiles of a row from the orginal image	29
3.12	Column level minimum intensities.	29
3.13	Beam hardening correction	30
3.14	An example <i>sym4</i> wavelet	31
3.15	Illustration of one-dimensional signal denoising in wavelet domain. . .	34
3.16	Illustration of one-dimensional signal denoising in wavelet domain. . .	35
3.17	A log-Gabor wavelet	35
3.18	Wavelet denoising the plant root images	38
3.19	Matched filtering responses	39
3.20	Matched filtering responses for different scales	40
3.21	Enhanced image with multi-scale matched filtering	41
3.22	RSA extraction through multi-scale matched filtering	42
4.1	A sample sinogram image	44
4.2	Geometry of a parallel-ray beam	45
4.3	Illustration of Fourier-slice theorem.	47
4.4	Reconstructed cross-section through filter back projection	49
4.5	Three-dimensional model generated though filter back projection . . .	50
5.1	Example images from the air sample dataset. The plant root images are captured from different rotational viewpoints using the X-ray system.	53
5.2	Generated three-dimensional model through the proposed pipeline of matched-guided filtering and filtered back projection.	54
5.3	Comparison of two-dimensional projections. (a) Original two-dimensional projection from the dataset. (b) Two-dimensional projection obtained from the three-dimensional model.	54
5.4	Cross-sectional slices generated from the pre-processed images.	56

5.5	Extracted root (<i>highlighted in brown</i>) in each slice through RooTrak.	56
5.6	Cross-sectional slices generated from the raw images.	57
5.7	Extracted root (<i>highlighted in brown</i>) in each slice generated from the raw images through RooTrak.	57
5.8	Probability density functions of voxel intensities corresponding to root (<i>orange</i>) and background (<i>blue</i>) in the three-dimensional models. . .	58
5.9	A plant root imaged in top soil at different energy levels.	61
5.10	A plant root imaged in rolling bottom soil at different energy levels. .	62
5.11	A plant root imaged in filtered field soil at different energy levels. . .	63
5.12	Enhanced root segments in top soil images following the proposed multi-scale matched filtering.	64
5.13	Enhanced root segments in rolling bottom soil images following the proposed multi-scale matched filtering.	64
5.14	Enhanced root segments in filtered field soil images following the proposed multi-scale matched filtering.	65
5.15	ROC curves corresponding to top soil images enhanced with multi-scale matched filtering.	66
5.16	ROC curves corresponding to rolling bottom soil images enhanced with multi-scale matched filtering.	66
5.17	ROC curves corresponding to filtered field soil images enhanced with multi-scale matched filtering.	66
5.18	Segmented RSA from the top soil images following the proposed multi-scale matched filtering method.	68
5.19	Segmented RSA from the rolling bottom soil images following the proposed multi-scale matched filtering method.	68
5.20	Segmented RSA from the filtered field soil images following the proposed multi-scale matched filtering method.	69

5.21 Isolated RSA from the top soil images following the proposed multi-scale matched filtering method.	69
5.22 Isolated RSA from the rolling bottom soil images following the proposed multi-scale matched filtering method.	70
5.23 Isolated RSA from the filtered field soil images following the proposed multi-scale matched filtering method.	70
5.24 Segmentation result of top soil images obtained through Otsu's thresholding.	71
5.25 Segmentation result of rolling bottom soil images obtained through Otsu's thresholding.	71
5.26 Segmentation result of filtered field soil images obtained through Otsu's thresholding.	72
5.27 Probability density functions of voxel intensities corresponding to the root (<i>orange</i>) and background (<i>blue</i>) in the three-dimensional models obtained with various filter banks.	75
5.28 Binary masks obtained by thresholding the enhanced images from various filter banks.	76
5.29 A top soil image enhanced through multi-scale matching with the filter banks consisting of filters created at various angular resolution.	78
5.30 ROC curves corresponding to top soil images enhanced with the filter banks created at various angular resolution.	79
5.31 ROC curves corresponding to rolling bottom soil images enhanced with the filter banks created at various angular resolution.	79
5.32 ROC curves corresponding to filtered field soil images enhanced with the filter banks created at various angular resolution.	80

5.33 Probability density functions of voxel intensities corresponding to the root (<i>orange</i>) and background (<i>blue</i>) in the three-dimensional models obtained with various filter banks.	83
5.34 Result of structure transferring the images enhanced with various filter banks.	84
5.35 ROC curves pertaining to top soil images enhanced with various filter banks.	86
5.36 ROC curves related to rolling bottom soil images enhanced with various filter banks.	87
5.37 ROC curves corresponding to filtered field soil images enhanced with various filter banks.	87
5.38 An image enhanced through multi-scale matched filtering with the filter banks consisting filters of various lengths (L)	88
5.39 An example of manually segmented image and corresponding root and non-root regions obtained by dilating with a disk of radius 15px. . . .	90
5.40 Color-coded binary images, representing true positives (<i>green</i>), false positives in the root (<i>red</i>) and non-root regions (<i>dark brown</i>), and classified negatives (<i>light brown</i>), obtained through thresholding. . . .	91

ABSTRACT

Plant roots are vital organs for water and nutrient uptake. The structure and spatial distribution of plant roots in the soil affects a plant's physiological functions such as soil-based resource acquisition, yield and its ability to live under abiotic stress. Visualizing and quantifying roots' configuration below the ground can help in identifying the phenotypic traits responsible for a plant's physiological functions. Existing efforts have successfully employed X-ray computed tomography to visualize plant roots in three-dimensions and to quantify their complexity in a non-invasive and non-destructive manner. However, they used expensive and less accessible industrial or medical tomographic systems. This research uses an inexpensive, lab-built X-ray computed tomography (CT) system, operating at lower energy levels (30kV-40kV), to obtain two-dimensional projections of a plant root from different viewpoints. I propose image processing pipelines to segment roots and generate a three-dimensional model of the root system architecture from the two-dimensional projections.

Observing that a Gaussian-shaped curve can approximate the cross-sectional intensity profile of a root segment, I propose a novel multi-scale matched filtering with a two-dimensional Gaussian kernel to enhance the root system. The filter assumes different orientations to highlight the root segments grown in different directions. The roots are isolated from the background by manual thresholding, followed by a mathematical morphological process to reduce spurious noise. The segmented images are filtered back projected to generate a three-dimensional model of the plant root system.

The results from the research conducted show that the proposed method yields a structurally consistent three-dimensional model of the plant root image set obtained in the air, whereas alternate methods could not process the image set. For plant root images collected in the air, the three-dimensional model generated from the proposed

matched-guided filtering and filtered back projection has a better contrast measure (0.0036) compared to the contrast measure (0.099) of the three-dimensional model created from raw images. For plant root images captured in the soil, proposed multi-scale matched filtering resulted in better receiver operating characteristic curves than the raw images. Compared to Otsu's thresholding, multi-scale root enhancement and thresholding have reduced the average false positive rate from 0.344 to 0.042, and improved the average F_1 score from 0.4 to 0.775. Experimental results show that the proposed root enhancement methods are robust to the number of orientational filters chosen, and are sensitive to the filter length selected. Small size filters are preferred, since increasing the filter length increases the number of false positives around root segments.

Chapter 1

Introduction

Roots play a crucial role in a plant's growth. They are the primary source of water and nutrient acquisition from the soil [1–9], and provide anchorage against uprooting forces [1]. Root system architecture (RSA) refers to the spatial arrangement of roots in a growth medium [1, 3–5]. The complexity of RSA affects roots' physiological functions such as water and nutrient uptake [10–14], carbon storage [1, 3], and ability to adjust to abiotic stress [3, 5, 6, 15–17], and influences plant yield [5, 18, 19]. Thus, there is a need to examine and understand the roots thoroughly to develop cultivars that have high yield under resource limiting environments to address the global issue of food security [2, 20]. Visualization and quantification of complex RSA are crucial to discover phenotypic traits that contribute to a plant's resistance towards abiotic stress [3, 6, 9, 17, 20]. Accordingly, some researchers have focused on analyzing RSAs, but most of the work has been carried out in the two-dimensional space [21, 22]. While these studies offered some valuable insights, they lacked the accuracy of a three-dimensional analysis. For a better understanding of the three-dimensional structure, the three-dimensional visualization of the root *in situ* is essential.

Existing efforts towards non-destructive and non-invasive three-dimensional visualization of plant roots grown in soil have extensively applied X-ray computed

tomography (CT) [8, 9, 17, 23–35]. These studies succeeded in visualizing and quantifying RSA. However, they employed expensive industrial or medical CT scanners operating at high energy levels ($> 100\text{kV}$). These scanners produce high-resolution and high-contrast images, easing the image processing efforts, but their low accessibility confines this type of research to a smaller group. This work aims to take this research to a broader audience by utilizing an inexpensive lab-built X-ray CT scanner, operating at lower energy (30kV-40kV) [36], and proposing a novel image processing pipeline, mainly designed for root images obtained from such scanners. The scanner collects two-dimensional projections of a plant supported in the air and various soil types at different angular intervals, and the image processing pipeline generates a three-dimensional model.

1.1 Goal of the study

The primary goal of this work is to create an automated image processing pipeline that produces an accurate three-dimensional model of a plant root from several two-dimensional X-ray images – captured at low energy levels, and regular rotational viewpoints. In order to do so, a lab-built X-ray CT system operating at 30kV-40kV is used [36]. Additionally, the proposed study intends to generate the three-dimensional model from few projections (180) of the plant root. Figure 1.1 summarizes the purpose of this study. Given a stack of two-dimensional projections, this study aims to highlight and isolate the root system from the background in low signal-to-noise-ratio (SNR) images and generate a three-dimensional model that is consistent with the segmented root system concerning root segments' width, height, and branching structure. Having a system capable of producing an exact three-dimensional model from low SNR images allows spatiotemporal analysis of the plant root in a non-invasive and non-destructive manner, and reduces the dependency on expensive industrial or

medical CT system for such analysis. Moreover, such a system makes it feasible to calculate complex phenotypic traits such as convex hull volume [20], or solidity [5].

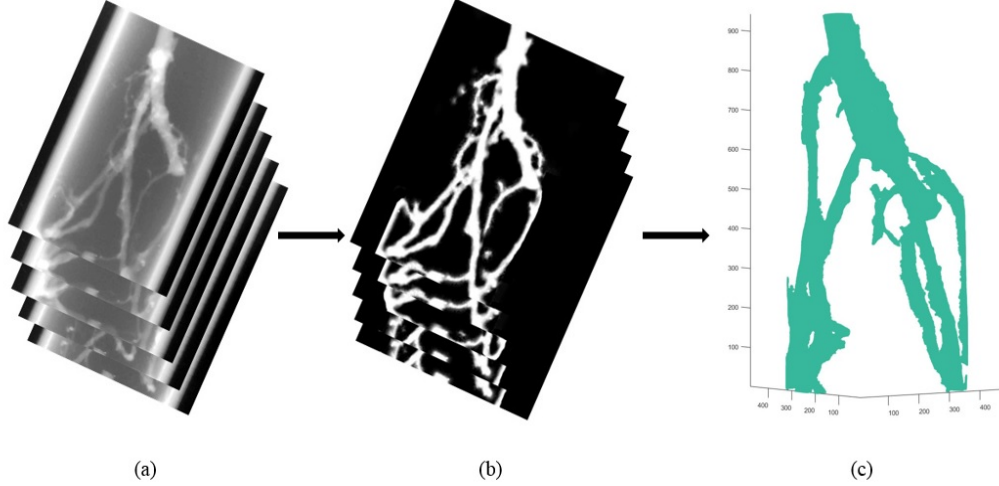
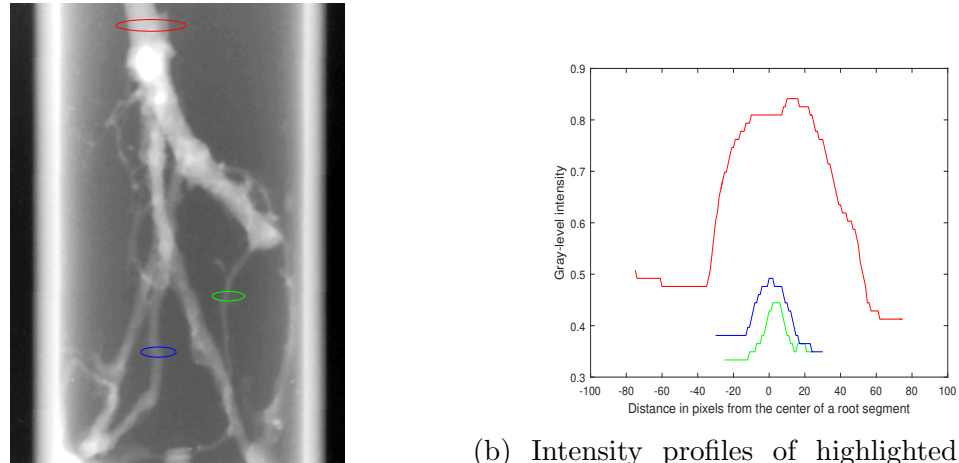


Figure 1.1: The purpose of the study is to generate a three-dimensional model from two-dimensional projections. (a) Two-dimensional image stack obtained from various view points. (b) Segmented image stack. (c) Three-dimensional model of the root system.

1.2 Assumptions

This study believes that piece-wise linear segments may approximate the root segments as they have a small curvature and their edges run anti-parallel – i.e., the edges are point-wise parallel, and the gradient along the edges have opposite signs [37]. Additionally, it is assumed that a Gaussian-shaped curve can approximate the cross-sectional intensity profile of a root segment. Figure 1.2a presents an example two-dimensional projection of a plant root obtained using the lab built X-ray imaging system. Figure 1.2b shows the cross-sectional intensity profiles of the highlighted root segments from the Figure 1.2a. In this Figure, it can be seen that Gaussian-shaped curves approximate them. Furthermore, it is also assumed in this study that a root system is the largest object present in the images, and only preserves the largest

component and removes all other components to isolate the root system from the background.



(a) A plat root imaged in air

Figure 1.2: An example root image obtained through the lab built X-ray system.

Chapter 2

Literature Review

This chapter presents the existing efforts to build a three-dimensional model of plant roots. At first, various studies related to understanding RSA, such as designing growth environments and imaging technologies leveraged are discussed. Later, image segmentation and three-dimensional reconstruction works are presented.

2.1 Studying root system architecture

Many approaches to observe and understand roots [1–7, 18, 20, 38–43] have been developed in the literature. They can be broadly classified into two categories, destructive [38, 39] and non-destructive [1–7, 18, 20, 40–43]. The non-destructive methods are further divided based on the growth media and imaging media. This section details about these categories and provides the advantages and disadvantages of these approaches.

2.1.1 Destructive methods

A common destructive method of studying RSAs is “root-washing” [38, 39]. In root-washing, a plant grown in natural soil is excavated and washed under a jet to isolate roots and, then, analyzed. Even though, this method provides accurate information about growth; many root segments are lost during the excavation process [1, 25, 26, 32]. Additionally, the excavation process is laborious and time-consuming [1, 25, 26]. Moreover, some of the three-dimensional topology (i.e., the relative positioning of root segments to each other) is lost due to excavation [34], limiting the collection of few phenotypic traits such as root angles. Washing often leads to root breakage, resulting in an underestimation of fine roots [1, 25, 32]. Furthermore, it is impossible to perform temporal analysis of the same plant.

2.1.2 Non-destructive methods

Considering the drawbacks of destructive methods of studying RSA, the research community has developed some of the non-destructive methods [1–8, 17, 18, 20, 23–35, 40–43] to allow spatiotemporal analysis of the RSA. Some of these works have used an artificial growth media (such as clear soil, gellan gums, etc.) [1–6, 18, 20, 40] and used digital imaging to study roots. Others have grown plants in natural soil and used advanced image processing techniques such as magnetic resonance imaging (MRI) and X-ray CT to understand RSA [8, 17, 23–35]. The following subsections discuss some of the proposed non-destructive methods, their advantages, and disadvantages.

Artificial growth media

Using artificial growth media has been popular among researchers [1–6, 18, 20, 40] to facilitate non-destructive studies. Widely used growth media include transparent soils, hydroponics, semi-transparent agars, and gellan gums. These media with high

optical clarity has overcome the problem of visibility of roots [20], eased imaging, and allowed spatiotemporal analysis. Digital imaging and three-dimensional laser scanning are some of the imaging techniques used with transparent media. Digital imaging is cost-efficient and easily accessible in many laboratories. In 2011, Clark et al. [20] proposed a novel imaging and software platform for high-throughput phenotyping. Three-dimensional reconstruction of two rice genotypes grown in gellan gum was generated from 40 two-dimensional images using their custom developed software, RootReader3D. A correlation was found between phenotypic traits measured from the three-dimensional model and two-dimensional images [20]. However, the authors admitted that the plant roots grown in gellan gum had significant morphological differences from the ones grown in hydroponics and sand. Piñeros et al. [3] developed a significantly improved growth and imaging system than RootReader3D [20], with the root supported by plastic mesh discs. This hydroponic-based mesh system allows easy replacement or replenishment of growth media, enabling advanced experiments imposing nutrient deficiency or drought stress to determine their effects on RSA traits. The designed system was more cost-effective than gellan gum based systems, had an improved image resolution, and hence, a better three-dimensional reconstruction [3]. However, the traits of cultivars grown in hydroponics were significantly different from the ones grown in soil [9, 20]. Even though these methods are widely adopted, mostly considering their cost-effectiveness and easy accessibility, it is still believed that artificial growth media is not an exact representation of plants' natural habitat [32].

Natural growth media

Considering that the artificial growth media may not be a good representation of soil, researchers have grown plants in their natural habitat and used advanced imaging technologies to visualize roots [8, 17, 23–35]. Rhizotrons, mini-rhizotrons, MRI and

X-ray CT imaging, constitute some of the state-of-the-art imaging techniques.

Rhizotrons and mini-rhizotrons allow studying roots in a non-destructive manner. They are extensively used to study the functions of fine roots in plant communities [7, 41–43]. In this type of imaging, a set of round transparent glass or plastic tubes are installed into the rooting zone [7] to monitor roots and capture images over time, allowing temporal analysis. Tube installation is critical, as they cause a disturbance in soil and creates a non-natural environment around them [7]. Usually, tube installation followed by a waiting period before image collection, to let the soil return to pre-disturbance level. Sometimes the installed tubes restrict the growth of roots around them. In this modality only a fraction of the root system is visible. Additionally, the observation is restricted to the root boundaries [7]; not allowing three-dimensional analysis.

X-ray CT and MRI are the modalities that allow observation of root's internal structure along with the surrounding soil matrix [25]. MRI, in particular, nuclear magnetic resonance (NMR), has been applied to study the plant roots grown in soil non-destructively. However, MRI imaging is expensive, and presence of paramagnetic components in soil leads to susceptibility artifacts caused by local magnetic field inhomogeneities [25, 44].

Unlike NMR, X-ray CT is not affected by the presence of paramagnetic components in soil [25]. It allows visualizing the RSA in three-dimensional space *in situ*, due to its non-destructive and non-invasive data collection procedure. Hence, it is deemed as one of the appropriate techniques to examine roots, and it is widely adopted in research community [8, 17, 23–35]. Heeraman et al. [23] were one of the early adopters to use X-ray CT to study root-soil interactions. In 2006, Kaestner et al. [27] imaged a synthetic root-like structure in a random background that represents soil texture to create an artificial three-dimensional image dataset. The three-dimensional structure is recovered from the image set using thresholding and mathematical morphology. A

significant limitation pointed out by Kaestner et al. [27] is that the overlapping attenuation values between roots and soil makes it difficult to distinguish them. In 2012, Mairhofer et al. [32] grew wheat, maize, and tomato plants in various soils like sand, loamy sand, and clay loam; and successfully extracted three-dimensional models of the root by tracking them in a μ -CT image using custom-designed software, RooTrak. However, RooTrak fails to recover upward-growing (plagiotropic) root segments. This issue is addressed in their later paper [33] by adding a ‘look-back’ step. Most of these existing methods [17, 26, 28, 34, 35, 44] were successful in extracting the RSAs and validating the phenotypical traits obtained from three-dimensional model against the features measured by the destructive excavation of the roots. Previous works employed either an industrial CT scanner or a medical CT scanner, which are capable of collecting high-resolution images, operating at high energy levels ($>100\text{kV}$). Not only these scanners are expensive, but they are also not accessible to a vast portion of the research community. This study uses an inexpensive lab-built X-ray CT scanner, operating at lower energy levels ($\leq 40\text{kV}$) built especially to examine roots. Such a system produces low-resolution and low SNR images. The growth media for plants consists of Haymond silt loam soil (rolling bottom soil), topsoil, and soil from a local field. This work mainly focuses on examining RSA using an inexpensive X-ray CT scanner.

2.2 Three-dimensional reconstruction

The previous section introduced the methods used to image roots, study and understand them. Some tried to understand roots from two-dimensional images [21, 22], while others examined a three-dimensional model [29, 32–34]. Three-dimensional analysis has been the trend of recent literature. This section provides an overview of methods developed to generate a three-dimensional model of a plant root system.

A vital step in generating a three-dimensional model is to detect and isolate roots from the soil. Global thresholding and region growing by adaptive thresholding are the two main approaches adopted to isolate roots from the soil in images. In global thresholding, a threshold value is determined based on the image histogram [24]. Region growing starts with seed locations or hotspots, most often a result of manual thresholding [8, 17, 31, 34], and iteratively adds nearby data items which meet some pre-determined requirements until there is no change in consecutive steps. Lontoc-Roy et al. [8] located large roots manually and used them as seed points, while Koebernick et al. [34] selected seed points by manual thresholding. However, thresholding often leads to misclassification of pixels (voxels) clustered in small groups. A post-processing step usually follows thresholding to remove such groups. Kaestner et al. [27] applied morphological dilation by reconstruction as a post-processing step to clear out speckle noise. Due to similar grayscale values of root and soil pixels, these methods often struggle to segment root correctly, i.e., they often misclassify root pixels as background and vice-versa [9].

The methods that considered just the attenuation values failed to extract root accurately [9]. Prior information, such as their appearance needs to be incorporated to reduce the complexity of the problem at hand [9]. One way is to consider the cross-sectional image stack as a sequence of images in which root cross-sections appear elliptic [24], and move around as the image stack is traversed. Those movements reflect the shape of the scanned root [32]. Tracing those ellipses could successfully recover the complete RSA. Pierret et al. [24] tracked elliptical objects under three-dimensional connectivity constraints in a top-down manner. Mairhofer et al. [32] developed another top-down system, RooTrak. RooTrak employs a level-set [45] based tracking algorithm. The tracking algorithm consists of an appearance model and a motion model. The appearance model includes the intensity distribution of a root segment in a cross-sectional slice. The motion model keeps track of the position

of a root segment in a cross-sectional slice. A user initiates the tracking algorithm by selecting a seed point belonging to a root segment in the 1st slice. The user provides multiple seed points to track different root segments. The level-set segmentation method identifies the root segment in the cross-sectional slice. An appearance model is generated based on the determined root. The motion model specifies the expected position of the root segment in the 2nd slice based on its location in the 1st slice. The level-set method searches around the spot suggested by the motion model for a region whose intensity distribution matches with that of the appearance model. If such a region is found, it is identified as root region. The appearance and motion models are updated to reflect the intensity distribution and location of the identified root region in the 2nd slice. These appearance and motion models along with the level-set method are applied to determine the root segment in the 3rd slice. The process of updating appearance and motion models, root identification through level-set segmentation, is repeated for each slice until the end of an image stack is reached. This tracking produced a three-dimensional model of the root. RooTrak successfully extracted the three-dimensional structure of wheat, maize and tomato roots from various soils [32]. However, as with any top-down connectivity search, this approach disregards upward-growing (plagiotropic) roots [9]. Mairhofer et al. [33] extended RooTrak to account for upward growing roots by adding a ‘look-back’ and ‘backward-pass’ steps. The ‘look-back’ step identifies and marks the plagiotropic roots while the ‘backward-pass’ step tracks them. While these methods succeeded in generating an accurate three-dimensional model of the plant roots, they used high-resolution images acquired through an industrial or medical CT.

Chapter 3

Image Segmentation

The purpose of this chapter is to introduce the image processing concepts proposed and employed in this work to enhance and isolate the root segments from the background (air or soil) in the images. Section 3.1 presents a novel method proposed to segment roots using an evolutionary approach. Section 3.2 discusses a matched-guided filtering method to enhance and isolate root segments, while section 3.3 presents a multi-scale matched filtering method to enhance and segment the roots of various widths.

3.1 Evolutionary approach to root extraction

When the one-dimensional projections of a plant root's cross-section collected from different view points are displayed as an image, it is referred as a sinogram [46]. Figure 3.1a shows an example sinogram image. It is observed from the image that the root segments appear as bright waves in sinogram domain and sinewaves can approximate them. Based on this observation, the root extraction problem is redefined as extracting the sinewaves from the sinogram images. Where, the amplitude (A) of a

sinewave represents the distance between the axis of rotation and the center of the root segment in a cross-section, while the phase (ϕ) represents the angle between the incident X-rays and the line connecting the axis of rotation and the center of the root segment. The width (w) of the sinewave denotes the width of the root segment. As the RSA contains root segments of various widths, orientation, and appear at different distances from the axis of rotation, the resulting sinewaves have different amplitude (A), phase (ϕ), and width (w). The sinewave extraction starts with estimating the parameters (A, ϕ, w) for each sinewave present in the image. The parameters can be estimated following any search mechanism (grid search or evolutionary approach) in the parametric space. In this study an evolutionary approach, more specifically a genetic algorithm, is used to find the parameters.

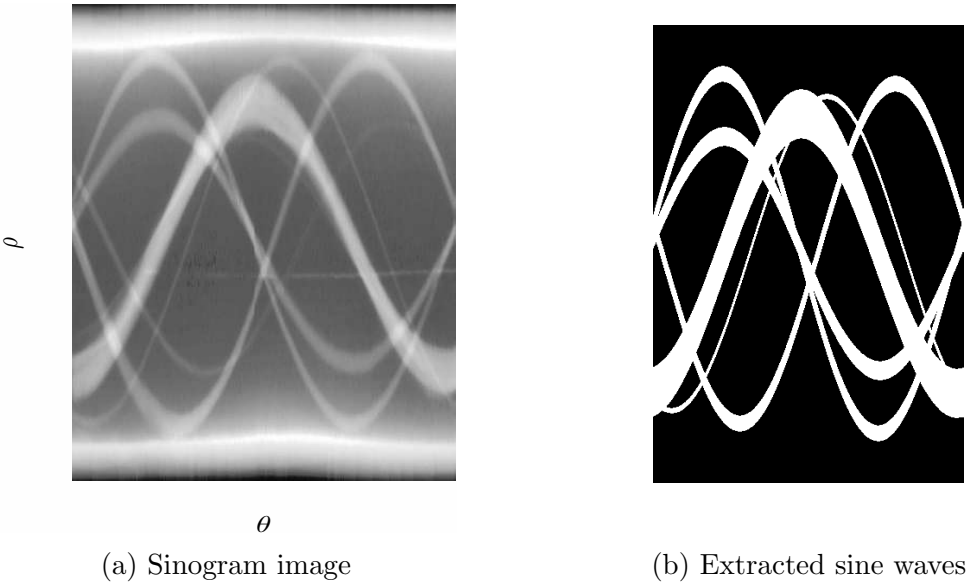


Figure 3.1: Sine waves extraction using genetic algorithm.

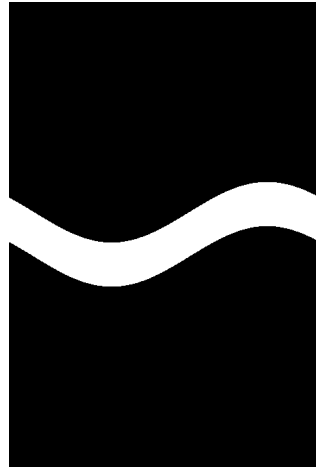
A genetic algorithm is an evolutionary approach to find solutions to constrained and unconstrained optimization problems, following the natural selection process [47, 48]. The fundamental idea behind the genetic algorithm can be stated as follows: Given a population of individuals, the environmental pressure causes the natural selection (survival of the fittest), which in turn rises the fitness of the population

with the environment over following generations [49–51]. Given an objective function to maximize, a set of random candidate solutions are generated. The function value for these candidate solutions represents a fitness measure – the higher, the better. Some candidates from the group are selected to be parents based on a probability proportional to their fitness scores. These parent candidates are crossed-over and mutated to produce a new generation of candidate solutions (children). Based on the fitness value, only some of these children candidates are retained to generate new off-springs. This process continues until a predefined number of iterations is reached or until a candidate with sufficient quality is found [49,50]. Hence, the expected result of this iterative process is that the population evolves towards the desired solution over generations. Furthermore, a genetic algorithm consists of the following four components:

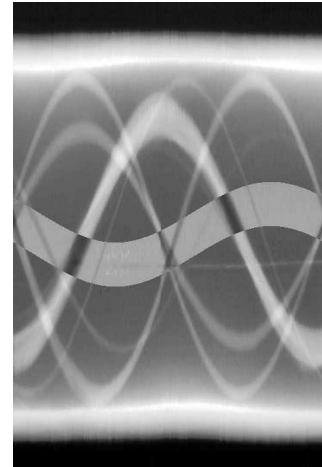
1. **Fitness function:** The fitness function is the function to be optimized (minimized or maximized), where the function value for a given candidate represents the candidate’s fitness score. Since we are searching for sinusoidal parameters that overlap with the ones of waves generated by root segments, we define the fitness function as reciprocal to the residual intensity in the sinogram image (I) after removing the candidate sine-wave, and seek for candidates that maximize it. To calculate the score, we begin by creating a binary image E (Figures 3.2a, and 3.2c) with only the pixels belonging to the candidate sinusoid set to 1 (Equation 3.2). We find the pixel-wise difference between E and I (Figures 3.2b, and 3.2d), and consider the reciprocal of the sum of absolute differences as the fitness score (F). The following equation provides a mathematical representation of this fitness function F :

$$F = \frac{1}{\sum_i |E_i - I_i|} \quad (3.1)$$

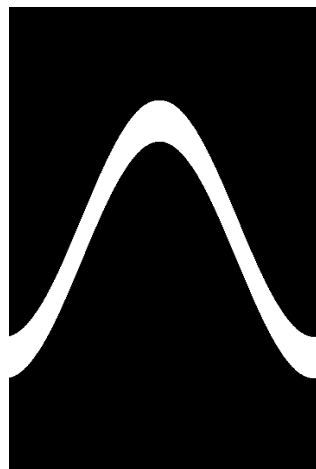
$$E(x, y) = \begin{cases} 1, & \text{if } y \in [A \sin(x + \phi) - \frac{w}{2}, A \sin(x + \phi) + \frac{w}{2}] \\ 0, & \text{otherwise} \end{cases} \quad (3.2)$$



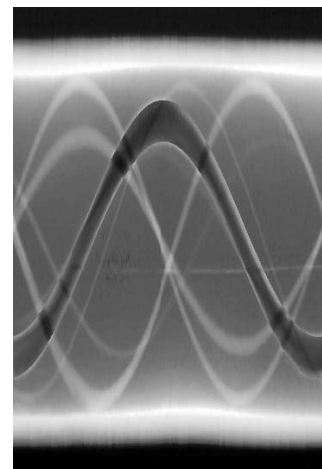
(a) Random candidate solution



(b) $F = 99676$



(c) Optimal solution.



(d) $F = 93485$

Figure 3.2: Calculating a fitness score. (a) Binary image, E , generated for a random candidate wave. (b) Absolute residual intensity with random candidate wave. (c) Binary image, E , generated for an optimal wave obtained after 1000 generations. (d) Absolute residual intensity with optimal wave.

When the candidate sinewave aligns with the background (low-intensity pixels)

the absolute residual intensity (Figure 3.2b) is more compared to when it aligns with the actual sinewave in the sinogram as the sinewave appear bright (Figure 3.2d).

2. **Selection criteria:** Selection criteria defines the guidelines, often based on fitness score, to select a candidate for cross-over. In this case, we used stochastic universal sampling (SUS) [52–54] as our selection criteria to choose the candidates from a population P to be the parents in each generation. Our implementation of SUS maps each candidate solution from the population to contiguous segments of a line. The length of the segment corresponding to a candidate is equal to the probability of its selection p_i (Equation 3.3). n equally spaced pointers are placed over the line to select n individuals from the population, where the distance between the pointers is $1/n$. A random number generated in the range of $[0, 1/n]$ determines the position of the first pointer. The individuals corresponding to the segments pointed by the pointers are selected for cross-over.

$$p_i = \frac{F_i}{\sum_{j \in P} F_j} \quad \forall i \in P \quad (3.3)$$

3. **Cross-over:** Cross-over operates on selected candidates, it swaps a portion of parameters between a pair of solutions to generate new off-springs. Five candidates are selected to produce the next generation of candidates from the population of individuals based on the selection criteria. Every pair of candidates ($parent1, parent2$) generates two children ($child1, child2$). The first child, $child1$, receives phase (ϕ) and width information (w) from $parent1$, and amplitude (A) from $parent2$. And inversely, $child2$ inherits phase (ϕ) and width information (w) from $parent2$, and amplitude (A) from $parent1$.

4. Mutation: As the process of changing the characteristics of a population over time, we use mutation to change the characteristics of the offspring produced by cross-over. It creates diversity in the group and ensures exploring different parts of the solution space [49, 50]. To create mutations, we add some noise, η in Equation 3.4, to the parameters of each candidate (Equations 3.5, 3.6, and 3.7). As the population evolves towards an optimal solution over the generations, the amount of noise added as a part of mutation reduces over the iterations.

$$\eta = 10 - \log_2(i) \quad (3.4)$$

$$A = \begin{cases} A - \eta, & \text{if } r < 0.5 \\ A + \eta, & \text{otherwise} \end{cases} \quad (3.5)$$

$$\phi = \begin{cases} \phi - \eta, & \text{if } r < 0.5 \\ \phi + \eta, & \text{otherwise} \end{cases} \quad (3.6)$$

$$w = \begin{cases} w - \eta, & \text{if } r < 0.5 \\ w + \eta, & \text{otherwise} \end{cases} \quad (3.7)$$

Where, i is the iteration number and r is a random number generated between 0 and 1.

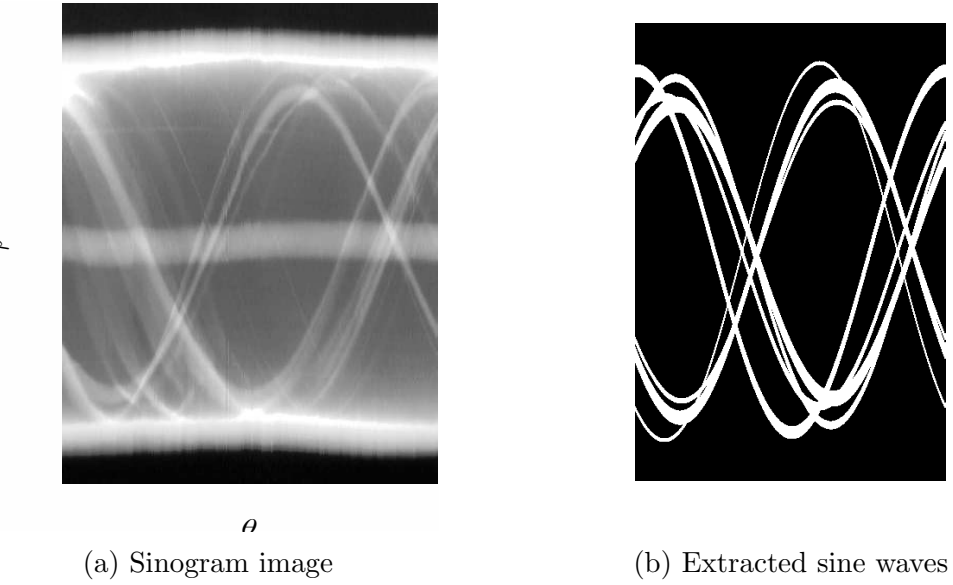
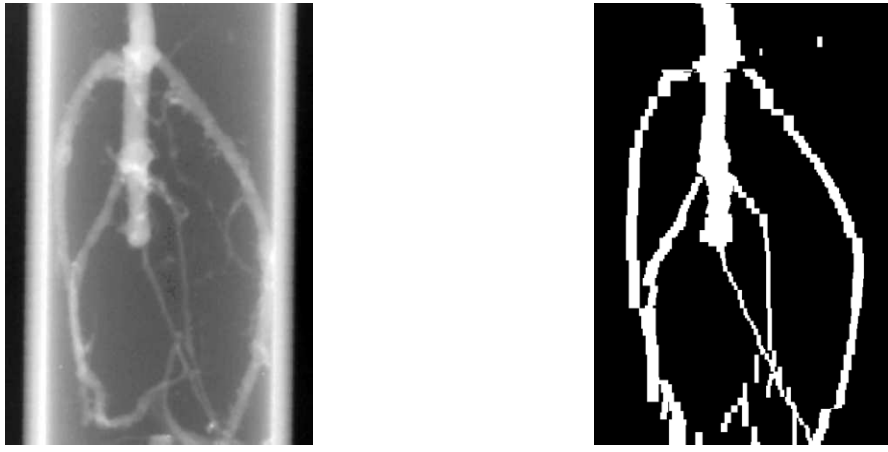


Figure 3.3: Sine waves extraction using genetic algorithm.

This genetic algorithm implementation starts with a random initial population of 20 individuals and computes fitness scores for each candidate. Five candidates are selected to produce new generation according to our selection criteria defined above. Every pair of chosen candidates produces two children following the cross-over and mutation methods mentioned. Overall, the five parents produce 20 children for the next generation, and this process is repeated a thousand times. Ultimately, the parameters of the candidate with the best fitness score (F) are selected to be the parameters of one sine-wave.



(a) Raw two-dimensional projection (b) Segmented two-dimensional projection

Figure 3.4: Result of segmentation through sine wave extraction.

To segment a sinogram image, we manually supplied the number of sinusoids existing in it. If there are multiple waves, we fit one at a time. Calculating a fitness score for a candidate wave considers all of the previously estimated waves, i.e., the created binary image (E) consists of already fitted sinusoids and the current sinusoid. The pseudocode of the implemented genetic algorithm is presented in Algorithm 1 . While this worked well for sinograms where the root segments are brighter and distinguishable from the background (Figure 3.1), it fails when background and sinusoids have similar intensities (Figure 3.3). In Figure 3.3, the algorithm fits only brighter sinusoids, missing portions of the root segments. As the segmented sinogram have step edges, instead of ramp edges, the root segments in the resultant two-dimensional projections contains jagged edges (Figure 3.4). Even though the jagged edges can be smoothed following morphological post-processing, the method failed to detect thin root segments. Moreover, the number of sine-waves in the sinogram image has to be specified manually.

Algorithm 1 A Genetic algorithm for sinogram image segmentation

```
1: procedure SEGMENT_SINOGRAM(sinogram, wavecount)
2:   for count  $\leftarrow$  1 : wavecount do
3:     population  $\leftarrow$  RANDOM_GENERATION()
4:     scores  $\leftarrow$  COMPUTE_SCORES(population)
5:     for iter = 1 : 1000 do
6:       parents  $\leftarrow$  SELECTION(population, scores)
7:       population  $\leftarrow$  CROSSOVER(parents)
8:       population  $\leftarrow$  MUTATE(population)
9:       scores  $\leftarrow$  COMPUTE_SCORES(population)
10:      end for
11:      selected_candidates  $\leftarrow$  selected_candidates  $\cup$  population{0}
12:    end for
13:    return selected_candidates
14: end procedure
```

3.2 Matched-guided filtering

An image processing pipeline of two-dimensional matched, and guided filtering, and morphological processing to enhance root segments is presented. The container edges in the images are identified and removed by applying Hough transform for straight line detection before passing them through the enhancement pipeline.

3.2.1 Two-dimensional matched filtering

A matched filter is a linear filter that maximizes the signal-to-noise ratio (SNR) in images [55, 56]. It involves correlating a known signal, or template, with an unknown signal to detect the presence of the template in the unknown signal [55, 56]. Matched filtering is one of the well-known methods for vessel enhancement in retinal images [57–60]. Chaudhuri et al. [57] designed a two-dimensional Gaussian filter bank to enhance the highlighting of blood vessels in retinal images, using thresholding to give the vascular structure. The same method is adapted here to highlight roots considering its commonalities with blood vessels. Like blood vessels, plant root's cross-sectional intensity exhibit a Gaussian profile given that they are also piecewise

linear segments having small curvatures.

Assuming that the intensity profile of a root segment is symmetric about a straight line passing through the center of it. The following equations represent a one-dimensional Gaussian function $g(x)$ and the corresponding matched filter kernel $K(x, y)$ [57].

$$g(x) = \frac{1}{\sqrt{2\pi}\sigma} e^{-x^2/2\sigma^2} \quad (3.8)$$

$$K(x, y) = \begin{cases} \frac{1}{\sqrt{2\pi}\sigma} e^{-x^2/2\sigma^2}, & \text{if } |y| \leq L/2 \\ 0, & \text{otherwise} \end{cases} \quad (3.9)$$

Here, L is the length of the segment for which the root is assumed to have a fixed orientation and σ defines the spread of the intensity profile.

A Gaussian filter is a point-spread function—spreads the intensity of a pixel around its neighborhood defined by the filter mask—and it has infinitely large non-zero tails (i.e. $x \in (-\infty, \infty)$). For the digital implementation, the kernel size is set to cover three standard deviations from the mean, on either side, as it covers 99.7% of the Gaussian distribution. Based on this we define the neighborhood N as

$$N = \{(x, y) | |x| \leq 3\sigma, |y| \leq L/2\} \quad (3.10)$$

$$K(x, y) = \frac{1}{\sqrt{2\pi}\sigma} e^{-x^2/2\sigma^2} \quad \forall \{|x| \leq 3\sigma, |y| \leq L/2\} \quad (3.11)$$

Equation 3.11 gives the filter mask with neighborhood N . This filter should yield a positive response to Gaussian intensity profiles in the image, and its response is expected to be zero in the areas of constant intensity. To ensure that, the weights of $K(x, y)$ are adjusted to have a mean of zero by subtracting the mean. The following

equation presents the mean adjusted matched filter.

$$K'(x, y) = K(x, y) - \frac{\sum_{p \in N} K(x, y)}{|N|} \quad (3.12)$$

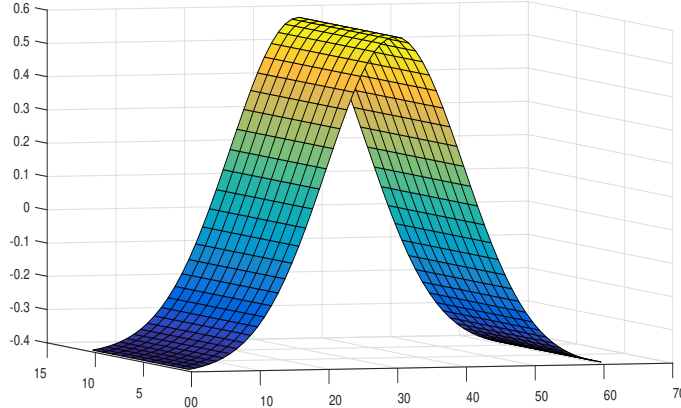


Figure 3.5: A matched filter with $\sigma = 10$ and $L = 11$ visualized in three-dimensional space

The pre-processed images are convolved with the filter (Figure 3.5) to enhance the RSA. A matched filter produces peak response when its orientation matches with that of a root segment. As roots grow in random directions, the kernel has to be rotated and convolved with the image in all possible angles to highlight the entire system. In our work, we used an angular resolution of 30° to enhance the root system. To cover all possible orientations at an angular resolution of 30° , we need six such kernels.

We designed a filter given by Equation 3.12 and rotated it by θ to create new filters at different orientations. The results of convolving Figure 3.7a with a kernel of $\sigma = 10, L = 11$ rotated at $\theta = -90^\circ, -60^\circ, -30^\circ, 0^\circ, 30^\circ$, and 60° are shown in Figure 3.6. The responses are compared, and only a maximum value per pixel is retained to generate a final enhanced image (Figure 3.7b). The value of σ is selected based on trial and error process. It is found that $\sigma \in [5, 10]$ preserved the width of both thin and thick root segments in the mask for this dataset. $\sigma < 5$ retained only the width of the fine roots (Figure 3.7c), while $\sigma > 10$ preserved the thickness of wider roots

only (Figure 3.7d).

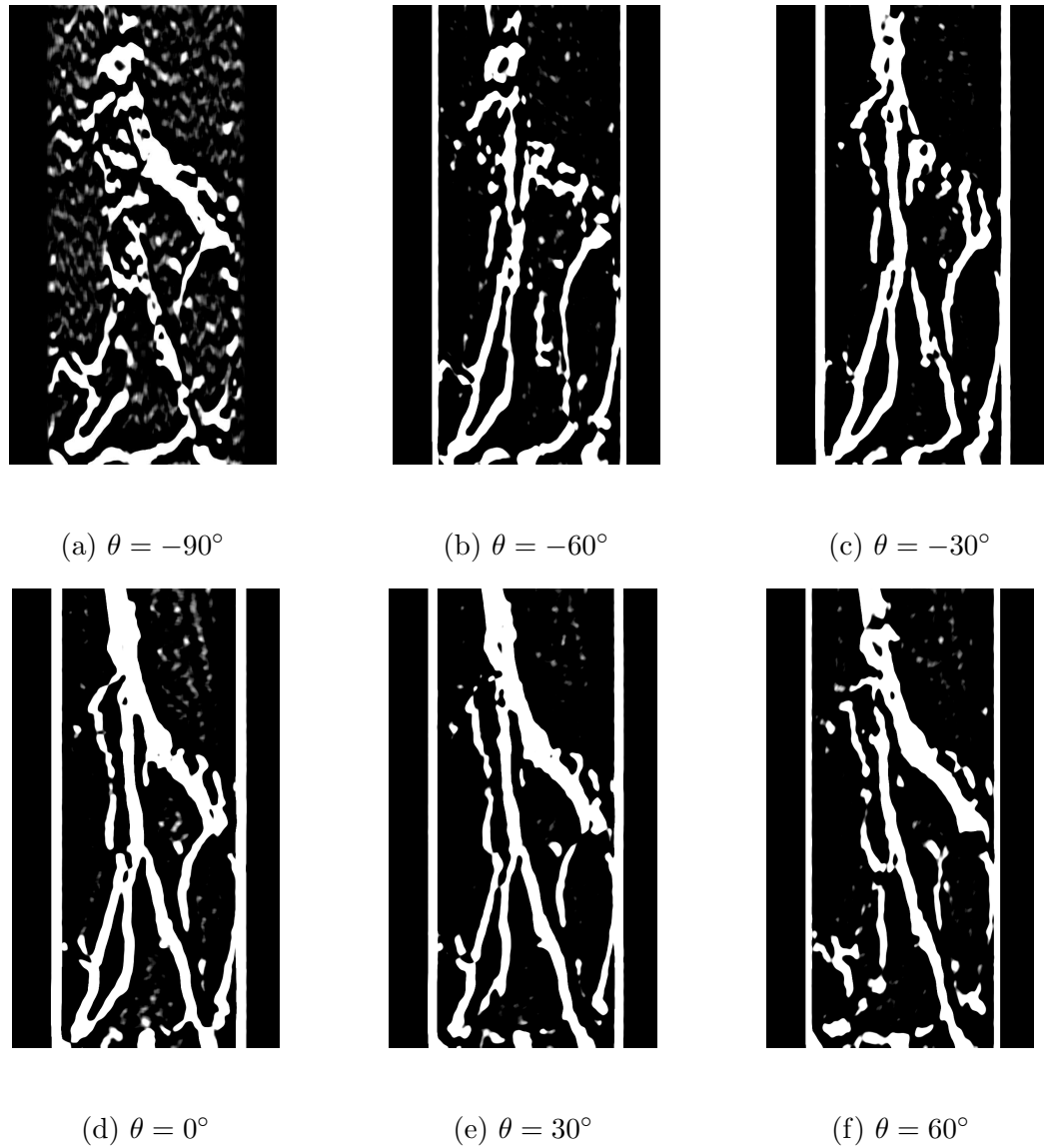


Figure 3.6: Matched filtering response for different orientational filters.

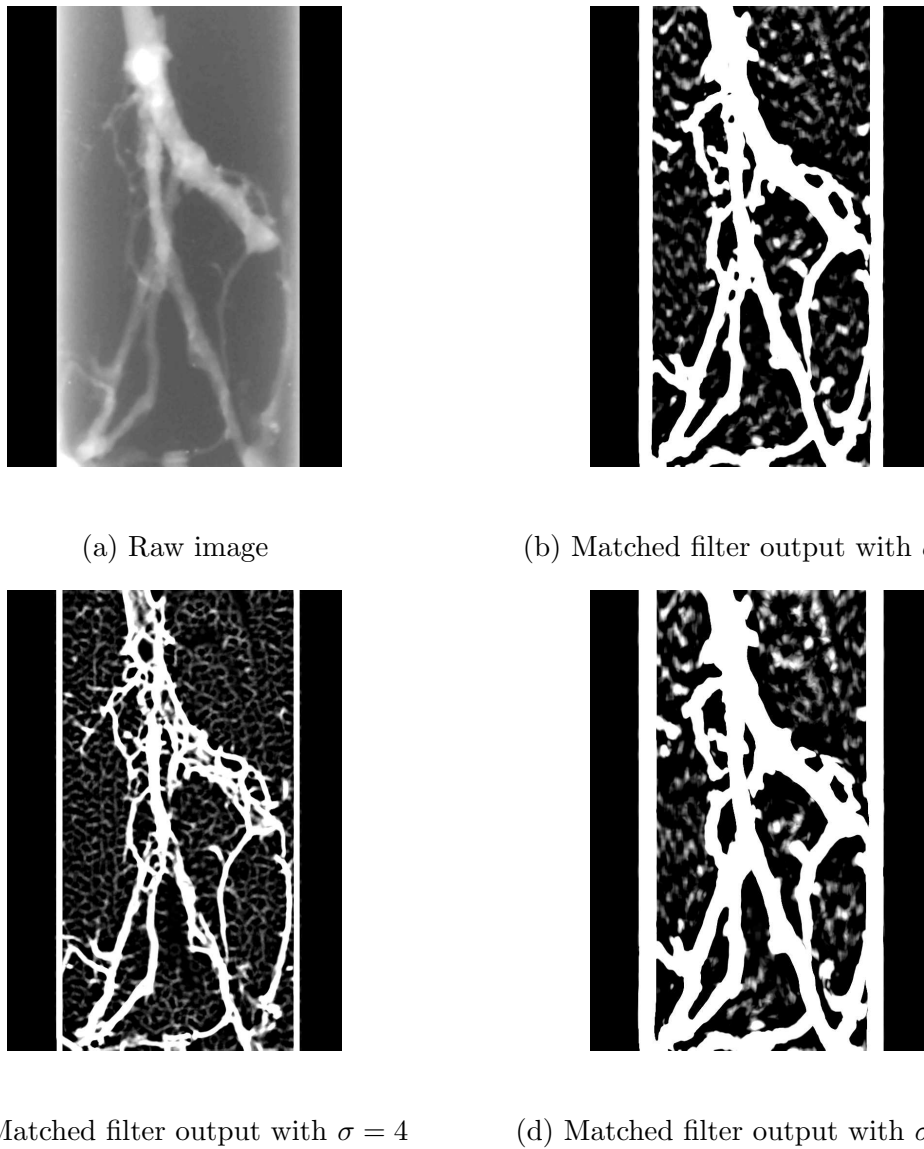


Figure 3.7: Orientational matched filtering a root image.

The goal is to obtain a binary mask that contains the root system. To achieve this, the matched filter response (Figure 3.7b) is thresholded. The threshold value is manually chosen such that most of the root system is labeled as foreground. Figure 3.8 presents the thresholded mask. It is observed that some small background components are misclassified as foreground. Morphological closing and opening are employed to get rid of such noise (Figure 3.9b).

It can be seen that the mask (Figure 3.9b) is not an exact representation of the

root system. We have performed guided filtering [61] to refine the mask. The following section introduces the concept of guided filtering.

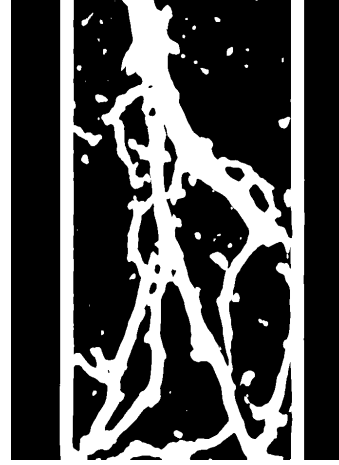


Figure 3.8: Binary mask obtained through thresholding.

3.2.2 Structure transferring

A guided filter [61] has been extensively applied in edge aware smoothing [61, 62], detail enhancement, dehazing [63, 64] and image feathering [65]. The filter can transfer the characteristics or structures, such as edges, from one image (Guidance image I) to another image (input image p), producing an output image q containing a blend of input and guidance image characteristics. The filter assumes that the output image q is a local linear transformation, i.e. a locally scaled version of the guidance image.

The following equation represents the local linear transform of a window w_k centered on the k^{th} pixel, from guidance image to output image.

$$q_i = a_k I_i + b_k, \quad \forall i \in w_k \quad (3.13)$$

where a_k, b_k are the linear coefficients estimated to be constant over the window w_k .

It is also expected that the output should resemble the input image with subtracting
25

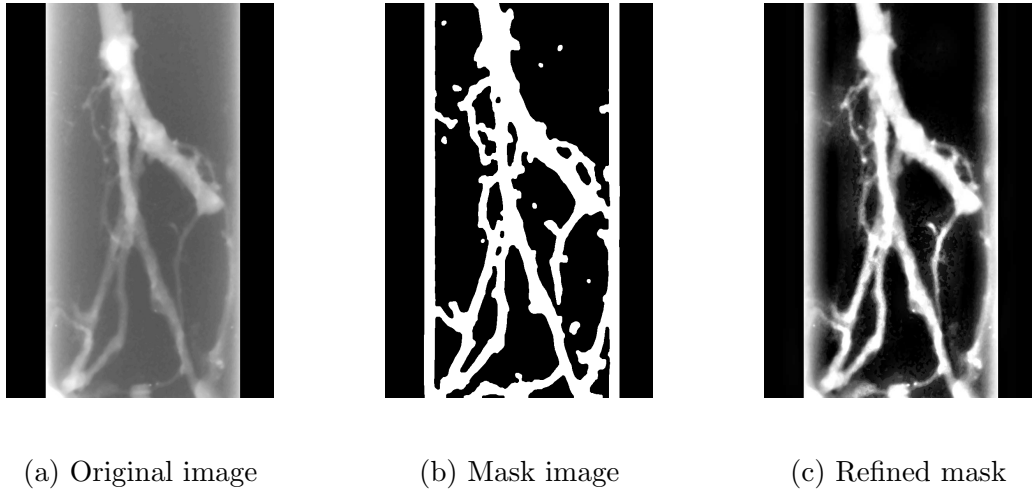


Figure 3.9: Structure transferring using guided filter with $w = 21, \epsilon = 0.01^2$

some noise, while adhering to the local linear transform (Equation 3.13). Obtaining the coefficients a_k and b_k involves minimizing a cost function that reduces the difference between the output and input images, and the cost function is expressed as follows:

$$E(a_k, b_k) = \sum_{i \in w_k} ((a_k I_i + b_k - p_i)^2 + \epsilon a_k^2) \quad (3.14)$$

where ϵ is the regularization parameter to penalize large values of a_k . Minimizing the cost with respect to a_k and b_k yields:

$$a_k = \frac{\frac{1}{|w|} \sum_{i \in w_k} I_i p_i - \mu_k \bar{p}_k}{\sigma_k^2 + \epsilon} \quad (3.15)$$

$$b_k = \bar{p}_k - a_k \mu_k \quad (3.16)$$

where μ_k and σ_k are the mean and variances of I in w_k . $|w|$ is the number of pixels in w_k and \bar{p}_k is the local mean of p in w_k .

The goal is to refine the binary mask image obtained through matched filtering to resemble the original root. To achieve this, we use the mask as the input image p ,

guided by the original image (Figure 3.7a). The following cases explain the structure transferring property of the guided filter:

1. When the window w is completely contained in the background of the mask, i.e. $p_i = 0 \forall i \in w$, we have $a_k = 0, \bar{p}_k = 0$ and $b_k = 0$. For such patches, the output image (q) would contain all zeros and preserves the background.
2. When the window w is positioned completely in the foreground of the mask, i.e. $p_i = 1 \forall i \in w$, we have $a_k = 0, \bar{p}_k = 1$ and $b_k = 1$. For such patches, the output image (q) would contain all 1s and preserves the foreground.
3. When the window w contains both foreground and background pixels of the mask, we have $a_k \neq 0$ and $b_k \neq 0$. Hence, a linear transformed version of the guidance image I is copied to the output image q producing a refined image (Figure 3.9c).

3.3 Multi-scale matched filtering

When plant roots are imaged in soil at lower energy levels, the acquired projections contain severe cupping artifacts and low signal-to-noise ratio (SNR). The following subsections discuss the methods employed to correct these artifacts and denoising through phase preservation in the wavelet domain. A multi-scale matched filtering to highlight the roots of various width and orientations is presented as well. Binarization of these images followed by refinement through the morphological processing yields segmented root structure.

3.3.1 Beam hardening correction

In general, laboratory X-ray systems produce a polychromatic beam [66–68]. When such a beam passes through a material, it is not attenuated evenly. Low-energy

photons are attenuated more easily or sometimes even absorbed entirely compared to high-energy photons [66, 68]. Though the overall intensity of the beam decreases as it passes through the material, the beam becomes harder (i.e. its mean energy increases) [66, 69]. The photons in the hardened beam get less attenuated, making the rays passing through the edge of a cylindrical object proportionally more attenuating than the rays passing through the center of the object [68].

Beam hardening produces cupping artifacts, where the edges of the cylindrical object appear brighter, creating a slowly varying artificial darkness as we move towards the center [67]. Figure 3.10a shows one of the plant roots imaged in Haymond silt loam soil (rolling bottom soil) at 35kV affected by cupping artifacts. The intensity profile of a row (Figure 3.11) illustrates that the central portion of the image has low-intensity pixels and pixels with a gradual increase in intensity as we move towards the edges.

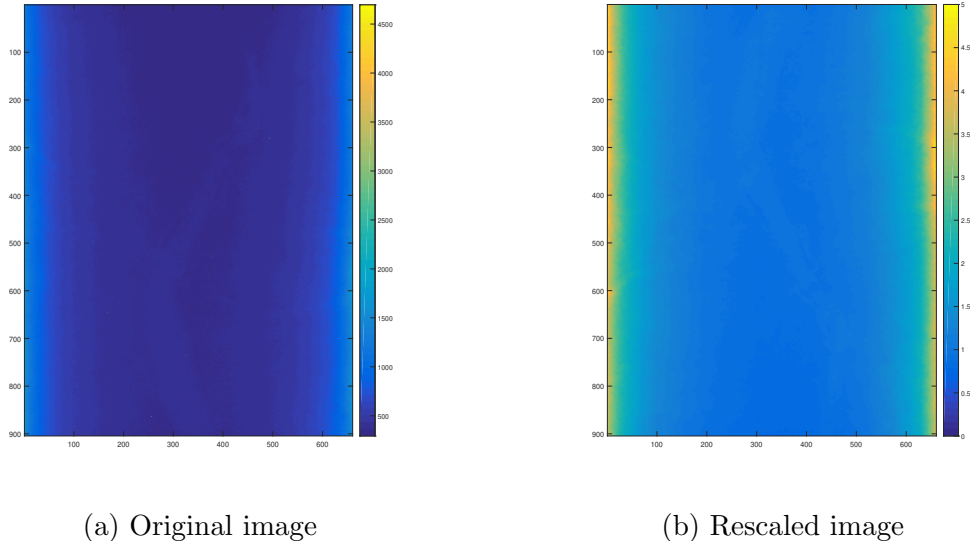


Figure 3.10: Plant root image captured in rolling bottom soil at 35keV

A new method based on modeling the slowly varying background is proposed to address cupping artifacts. Firstly, the original image is rescaled to have computed tomographic (CT) numbers in the range [0-5], to reduce the high variation in values

(Figure 3.10b). It is assumed that each column in the image would contain at least one background pixel (soil), except at the container edges. An approximation of the soil intensity across the whole image is obtained by taking minimum CT values from each column (Figure 3.12a). As there would be minor imperfections in the scintillator that result in CT numbers lower than that of the root, the minimum CT profile may not be a good approximation of the slowly varying background. A ninth order polynomial is fit to the minimum CT values to obtain a better model of the soil intensity profile (Figure 3.12a). Finally, the modeled background is subtracted from the original image to reduce cupping artifacts (Figure 3.13b).

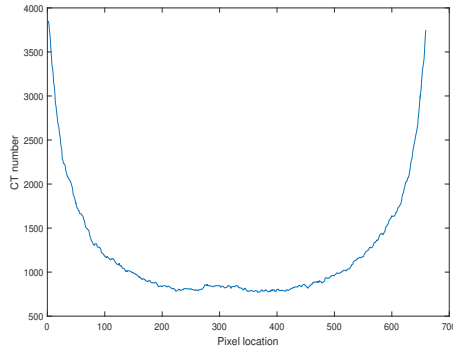


Figure 3.11: Intensity profiles of a row from the original image

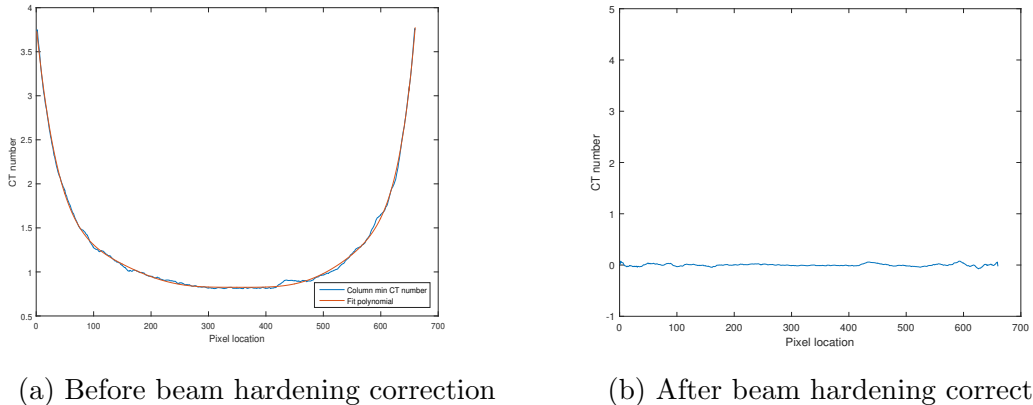
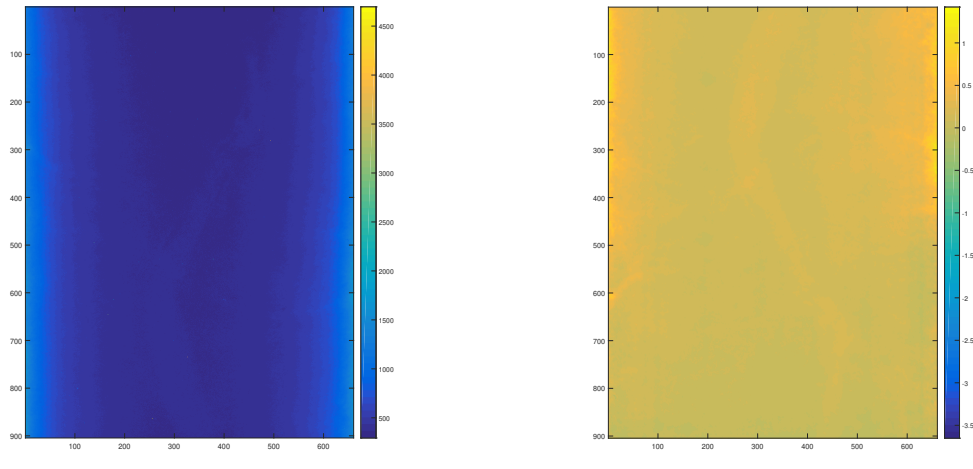


Figure 3.12: Column level minimum intensities.



(a) Original image

(b) Corrected image

Figure 3.13: Beam hardening correction

After beam hardening correction (Figure 3.13b), the CT number of a pixel is not affected by its distance from the central portion. It is only influenced by the composition of the material, i.e., root or soil. Figure 3.12b further illustrates this; it shows the minimum CT values across the image. Unlike in Figure 3.12a, the minimum CT values do not vary drastically as we move towards image edges.

We perform contrast stretching and adaptive histogram equalization on each image. Figure 3.18a shows the resultant image. The next step is to apply denoising methods to enhance the image.

3.3.2 Denoising

In general, denoising of a corrupted signal, image (two-dimensional signals) involves three steps. First, transforming the signal into some domain (Fourier domain, Wavelet domain, etc.), where the noise is distinguishable from the signal [70]. Second, applying a thresholding operation in the transformed domain to remove noise. And, lastly, using an inverse transform to reconstruct a noise-free signal. Studies have employed wavelet transforms extensively to denoise signals due to their effectiveness and sim-

plicity. In this work, a method based on wavelet transforms proposed by Kovesi [70] is used to denoise plant root images.

A wavelet transform provides a time-frequency (or spatial-frequency) representation of a signal (or images) using a series of short-lived functions called wavelets [71–73]. A wavelet is an oscillatory function of finite length that has a short burst of non-zero values and a value of zero everywhere else [71, 74]. Wavelets can be real or complex valued functions. Figure 3.14 shows a real-valued wavelet, *sym4* [71, 73].

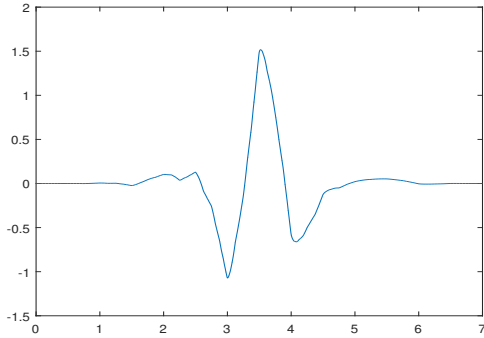


Figure 3.14: An example *sym4* wavelet

The wavelet transform of a signal is obtained by correlating it with a wavelet, and the correlation yields a real or complex value called wavelet coefficient. As wavelets are compact supported, (i.e., they have a non-zero value for only a short duration) one must repeatedly shift a chosen wavelet along the time axis to identify frequency bands at various time intervals throughout the signal in order to transform it [46, 72]. In order to represent the different frequency band, a wavelet is scaled and correlated with the signal to detect the presence of those bands, and the chosen wavelet is expanded (dilated) to represent low frequencies and compressed (contracted) to represent high-frequency bands [72]. The following equation expresses the time-frequency or wavelet domain representation of the entire signal:

$$\mathcal{W}_\psi(s, \tau) = \frac{1}{\sqrt{s}} \int_{-\infty}^{\infty} f(t) \psi\left(\frac{t-\tau}{s}\right) dt \quad (3.17)$$

where, $\psi(t)$ is the base wavelet or mother wavelet and $\mathcal{W}_\psi(s, \tau)$ are the wavelet coefficients as a function of scale and translation. The parameter τ represents the translation. The scale parameter, s , controls the amount of contraction or dilation. So, a wavelet is translated to detect a particular frequency band at different time intervals, and it is scaled to identify various frequency bands in a time interval. For a signal, $f(t)$, corrupted with some noise, a wavelet transform yields coefficients with large magnitude for pure signal, which stand-out from the coefficients corresponding to noise.

As a next step, hard or soft thresholding is employed to remove the noise coefficients. In hard thresholding, the coefficients with a magnitude less than the threshold value λ are set to zero, while other coefficients remain unchanged (Equation 3.18) [75].

$$\mathcal{W}_\psi(s, \tau) = \begin{cases} \mathcal{W}_\psi(s, \tau), & \text{if } |\mathcal{W}_\psi(s, \tau)| > \lambda \\ 0, & \text{otherwise} \end{cases} \quad (3.18)$$

Similar to hard thresholding, in soft thresholding the coefficients with a magnitude less than the threshold value λ are set to zero. However, other coefficients are reduced by an amount of λ towards zero (Equation 3.19) [75].

$$\mathcal{W}_\psi(s, \tau) = \begin{cases} \text{sign}(\mathcal{W}_\psi(s, \tau))(|\mathcal{W}_\psi(s, \tau)| - \lambda), & \text{if } |\mathcal{W}_\psi(s, \tau)| > \lambda \\ 0, & \text{otherwise} \end{cases} \quad (3.19)$$

After thresholding, a denoised signal is reconstructed by performing an inverse wavelet transform. Equation 3.20 mathematically expresses the inverse wavelet transform [46].

$$f(t) = \frac{1}{C_\psi} \int_0^\infty \int_{-\infty}^\infty \mathcal{W}_\psi(s, \tau) \frac{\psi(\frac{t-\tau}{s})}{s^2} d\tau ds \quad (3.20)$$

Where,

$$C_\psi = \int_{-\infty}^{\infty} \frac{|\Psi(\mu)|^2}{|\mu|} d\mu \quad (3.21)$$

μ represents frequency variable and $\Psi(\mu)$ is the Fourier transform [76] of the wavelet.

As an example, consider the one-dimensional signal ‘‘bumps’’ available in MATLAB [73]. Figure 3.15 shows a plot of the signal. To illustrate the effectiveness of wavelet denoising, I add Gaussian noise, $\mathcal{N}(0, 1)$, to the original signal. The noise-corrupted signal is shown in the second plot of Figure 3.15. The goal is to remove the noise from the corrupted signal and obtain a close approximation of the original noise-free signal. Wavelet denoising is performed to achieve that. First, the noisy signal is transformed into wavelet domain by correlating it with the *sym4* wavelet (Figure 3.14) at four scales corresponding to $1, \frac{1}{2}, \frac{1}{4}$ and $\frac{1}{8}$ following Equation 3.17. Figure 3.15 presents the wavelet coefficients obtained at $s = \frac{1}{4}$. It is apparent that the coefficients corresponding to the signal have large magnitudes compared to the coefficients corresponding to the noise. Moreover, the coefficients corresponding to the signal are localized, whereas the coefficients from the noise are distributed. Soft thresholding (Equation 3.19) is performed at all levels to remove the noise, setting the coefficients that are less than the threshold value to zero and shrinking the remaining coefficients towards zero. Figure 3.15 presents the shrunken coefficients at $s = \frac{1}{4}$. The non-zero coefficients correspond to the high frequencies in the pure signal. Finally, adding non-zero coefficients from all the levels and performing an inverse wavelet transform (Equation 3.20) reconstructs a denoised signal. Figure 3.16 plots the original signal in red, and the denoised signal in blue for comparison purposes. It is noticeable from the plot that denoising has removed a considerable amount of noise while preserving the sharp features in the signal.

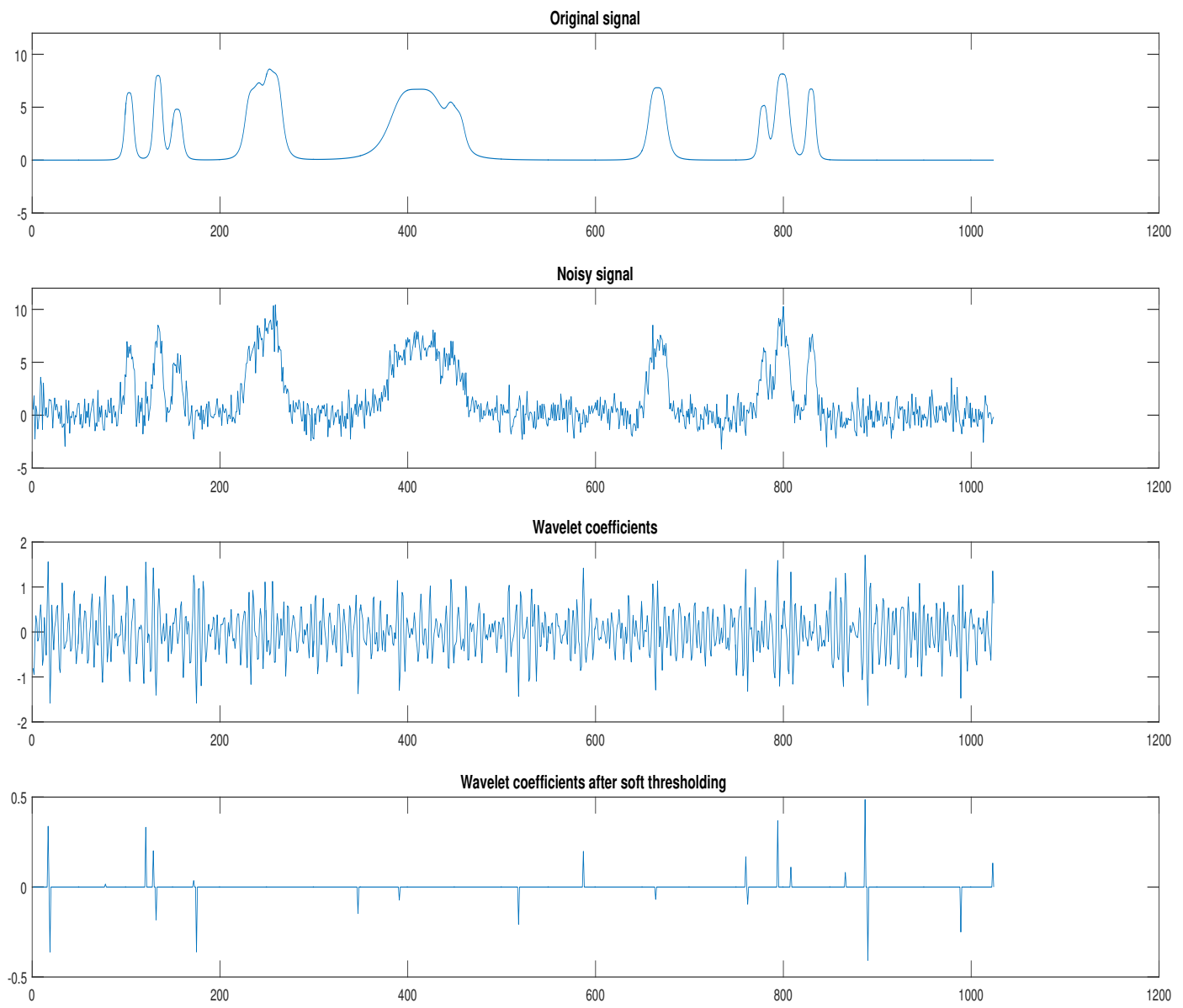


Figure 3.15: Illustration of one-dimensional signal denoising in wavelet domain.

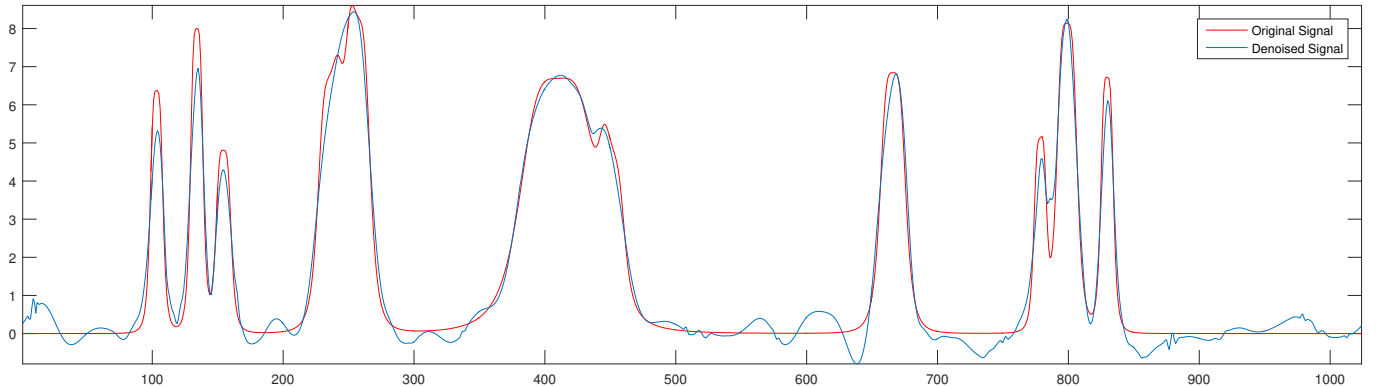


Figure 3.16: Illustration of one-dimensional signal denoising in wavelet domain.

The denoising method proposed by [70] is used to denoise images. Instead of the real-valued wavelet used in the previous example, a complex valued wavelet called log-Gabor is used to convert the image into a wavelet domain. It is not possible to derive an analytical expression of log-Gabor filter in a spatial or time domain []. The reasons are out of the scope of this study. The filter is first designed in a frequency domain, and then an inverse transform is performed to give the wavelet representation in the time domain. In the frequency domain the log-Gabor filter is expressed as

$$G(f) = e^{\frac{-(\log(f/f_0))^2}{2(\log(\sigma/f_0))^2}} \quad (3.22)$$

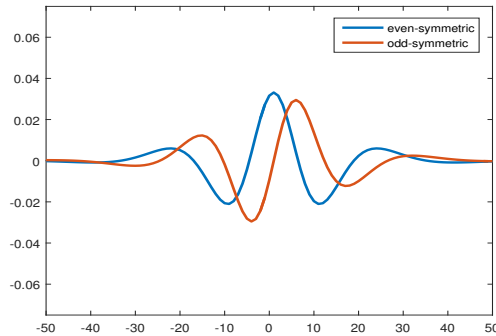


Figure 3.17: A log-Gabor wavelet

Figure 3.17 presents the log-Gabor wavelet in spatial or time domain. The blue

curve is the real part of the wavelet, while the red curve represents the imaginary part. The real part is symmetric around the central axis (i.e. $f(t) = f(-t)$) and is called an even filter. The imaginary part is anti-symmetric with $f(t) = -f(-t)$ [70].

As mentioned earlier, a wavelet is scaled and translated to identify both low and high frequencies at every location. The image is convolved with the log-Gabor wavelet at different scales producing complex coefficients at every pixel. Letting M_n^e, M_n^o denote even-symmetric and odd-symmetric wavelets at a scale n , The image I is convolved with M_n^e, M_n^o to generate a response vector given by the following equation

$$E_n(x) + jO_n(x) = I(x) * M_n^e(x) + jI(x) * M_n^o(x) \quad (3.23)$$

where, the values $E_n(x), O_n(x)$ can be thought of as a real and imaginary part of complex-valued coefficients. These complex coefficients can be expressed in polar coordinates as $A_n(x)e^{j\Phi(x)}$, where $A_n(x)$ is the magnitude calculated as

$$A_n(x) = \sqrt{E_n(x)^2 + O_n(x)^2} \quad (3.24)$$

and $\Phi(x)$ is the phase angle expressed as

$$\Phi_n(x) = \text{atan2}(O_n(x), E_n(x)) \quad (3.25)$$

The next step in denoising involves thresholding the magnitude of complex coefficients. As Kovesi points out, the magnitude of these complex coefficients follows a Rayleigh distribution while the coefficient themselves follow a 2D Gaussian distribution with mean zero and variance σ_g^2 in the complex plane [70]. Equation 3.26 represents the Rayleigh distribution

$$R(x) = \frac{x}{\sigma_g^2} e^{\frac{-x^2}{2\sigma_g^2}} \quad (3.26)$$

The mean μ and variance σ^2 of the Rayleigh distribution are given as

$$\mu = \sigma_g \sqrt{\frac{\pi}{2}} \quad (3.27)$$

$$\sigma^2 = \frac{4 - \pi}{2} \sigma_g^2 \quad (3.28)$$

Where σ_g^2 is the variance of the 2D Gaussian distribution in the complex plane.

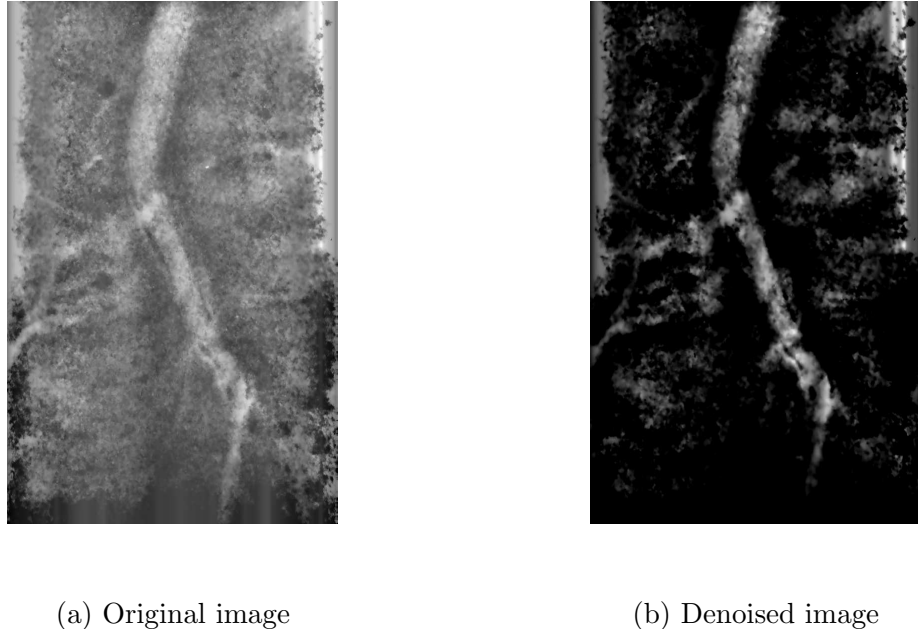
The estimate of the mean is empirically calculated using the median as

$$\mu = \frac{1}{2} \sqrt{\frac{-\pi}{\ln \frac{1}{2}}} \text{median} \quad (3.29)$$

And finally the threshold value is defined as

$$\tau = \mu + k\sigma \quad (3.30)$$

The threshold τ is set to some number (k) of standard deviations beyond the mean of the magnitude distribution 3.30, in this case $k = 3$. After thresholding, the real part of the coefficients are summed over all scales to obtain an estimate of the denoised signal in the wavelet domain, which is transformed back to the spatial domain to obtain a denoised image (Figure 3.18b).



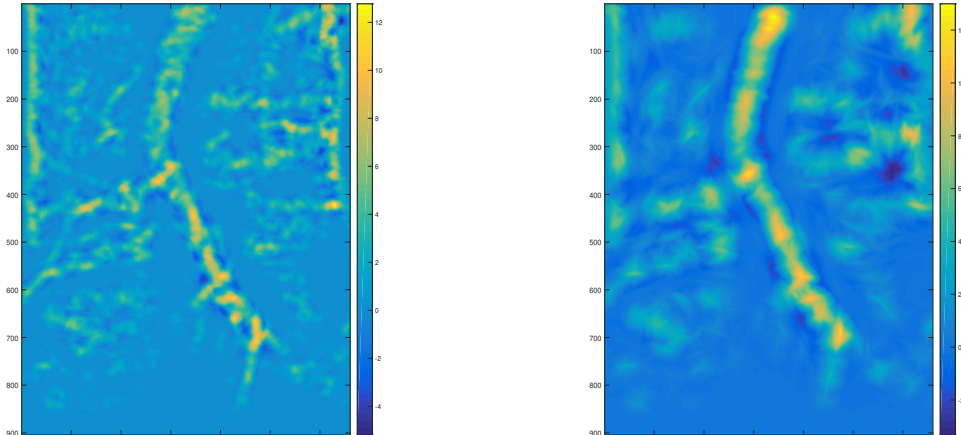
(a) Original image

(b) Denoised image

Figure 3.18: Wavelet denoising the plant root images

3.3.3 Segmentation

We applied two-dimensional matched filtering, discussed in section 3.2.1, to highlight the RSA. Figure 3.19 presents the result of matched filtering Figure 3.18b with $\sigma = 10$ and 30. From these images, we observe that only thin roots were enhanced at $\sigma = 10$, while $\sigma = 30$ highlighting the thick roots. This is due to the extreme noise levels present in the images. At large values of σ , matched filtering suppresses the noise by blurring, only preserving the broader roots. Thin roots are blent into the background. Smaller σ slightly blurs the image, cleaning the noise on thin roots without changing the wider roots. Due to this, we propose a multi-scale matched filtering approach to extract the complete RSA irrespective of the width. To do that, we create a filter bank consisting of matched filters (Equation 3.12) with various scales (σ). Each of these filters highlights the root segments whose diameter matches with its σ . A kernel with smaller σ enhances thin fragments while the ones with larger σ highlighting the broader roots.



(a) $\sigma = 10$

(b) $\sigma = 30$

Figure 3.19: Matched filtering responses

Selecting right scales for matched filtering involves a lot of trial and error process which is time-consuming. Moreover, root segments do not have a constant width instead they change slowly, further complicating the task, as we cannot choose σ values based on a portion of root segment. To avoid the time-consuming trial and error process, we create multiple filters in the range of $[\sigma_{min}, \sigma_{max}]$ with a resolution of $\Delta\sigma$. σ_{min} and σ_{max} are set to half of the thin and thick root respectively. In our experiments we considered $\Delta\sigma$ to be 5. For Figure 3.18b, σ_{min} and σ_{max} are estimated as 12 and 40 respectively.

Figure 3.20 shows the responses for scales in the range $[\sigma_{min}, \sigma_{max}]$. A single image per scale is obtained as specified in the previous section. Observing them reveals that they have a different range of values. Next, we rescale images to have values in the range [0 1]. To obtain a final image, we retain a maximum value per pixel from different scale responses. The Figure 3.21 shows the final image with roots of all widths enhanced.

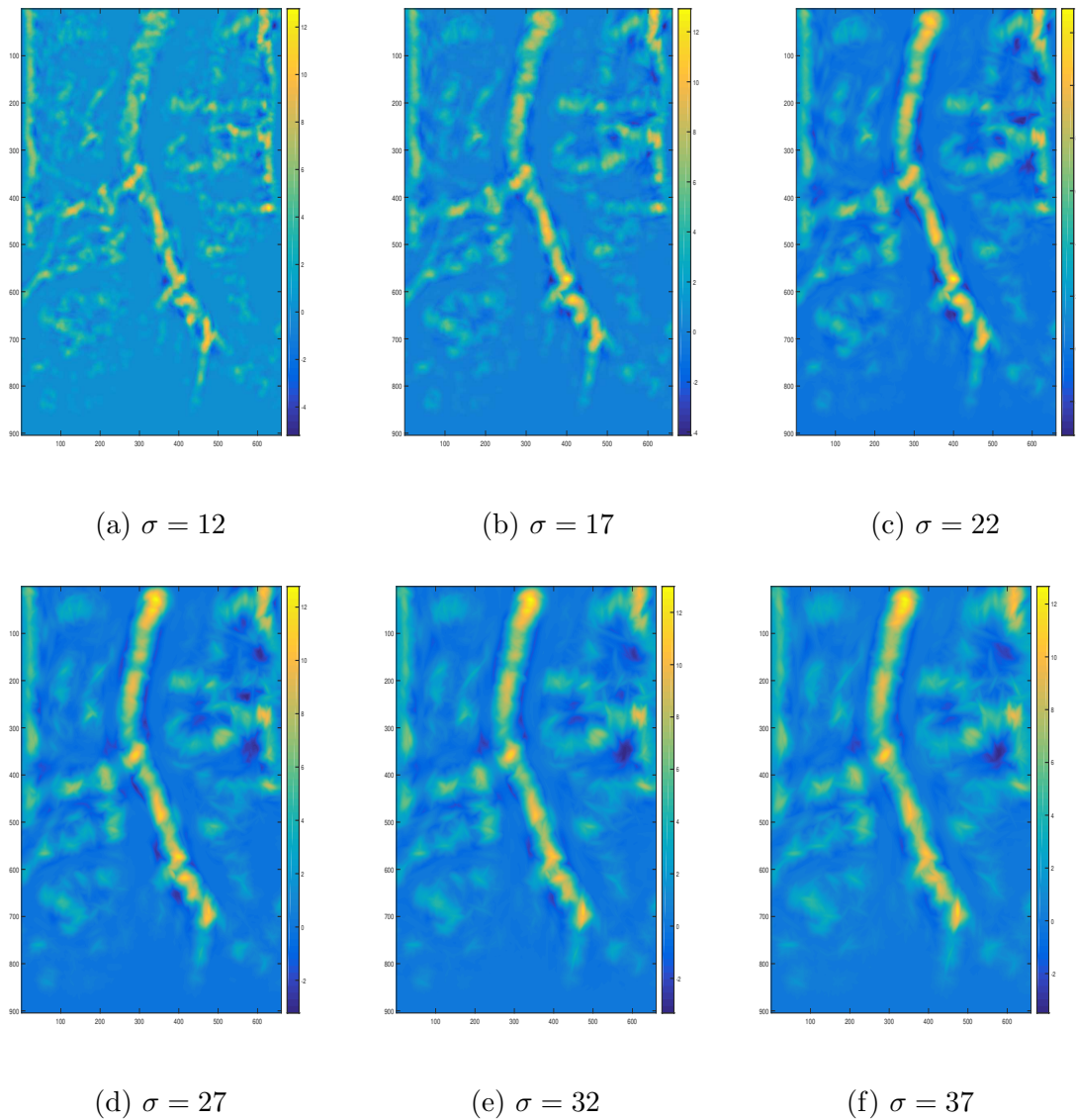


Figure 3.20: Matched filtering responses for different scales

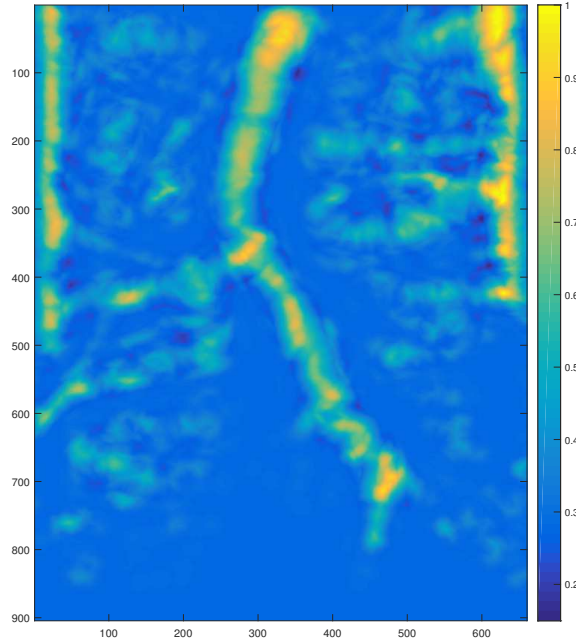


Figure 3.21: Enhanced image with multi-scale matched filtering

To isolate roots from the background, we employ thresholding. We visually inspect the images and select a threshold value, τ . The pixels with intensity larger than τ are assigned a value of 1 and considered to be a part of some root segment, otherwise, set a value of 0 and assumed to be soil pixels. τ is selected such that most of the RSA is assigned a value of 1. Note that this step may result in misclassification of background pixels as root, depending on the quality of images. However, this is necessary to lose as little RSA as possible. Moreover, such speckle noise can be removed later in a post-processing step.

Figure 3.22a shows the grayscale version of the enhanced image (Figure 3.21) obtained in the previous step. In our case, we chose $\tau = 0.4$ for image. Figure 3.22b presents the results of thresholding. As mentioned, some of the soil pixels are misclassified as root pixels. Assuming that root would be the largest connected component in the binary image, we remove all other components to obtain an isolated root (Figure

3.22c).



(a) Enhanced grayscale image (b) Result of thresholding (c) Isolated root

Figure 3.22: RSA extraction through multi-scale matched filtering

Chapter 4

Three-dimensional Reconstruction

In the previous chapter, we dealt with enhancing and extracting root segments in the two-dimensional projections. This chapter details the concepts behind generating a three-dimensional rendition from these projections.

4.1 Cross-sectional slice generation

The goal of this work is to obtain a three-dimensional representation of the plant root from two-dimensional projections. The two-dimensional projections are obtained from different directions by placing the container containing the plant root against an X-ray detector and illuminating it with X-rays. As X-rays pass through a cross-section, energy of the beam is absorbed, some rays are entirely absorbed, while others pass through and impinge the detector to produce a one-dimensional signal (absorption profile) [46]. The intensity of the obtained one-dimensional signal is proportional to the absorption values of the material. When the one-dimensional profiles obtained from different viewpoints are viewed as an image, it is called a sinogram image [46].

Figure 4.1 presents an example sinogram image.

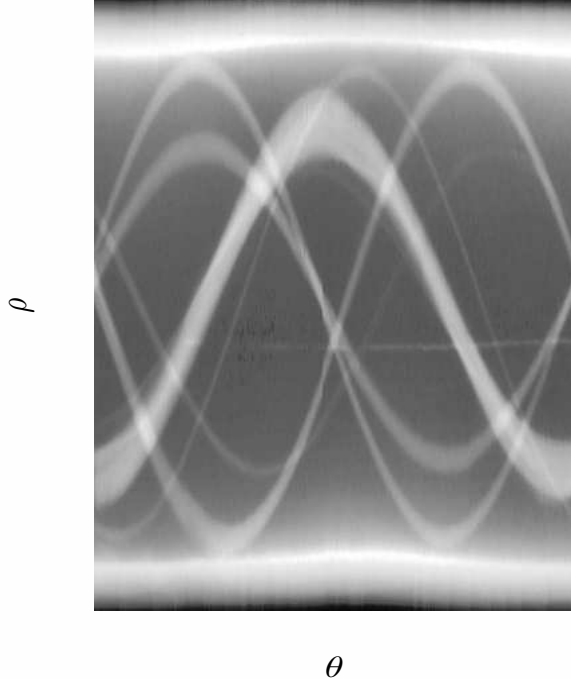


Figure 4.1: A sample sinogram image

4.1.1 Radon transform

Consider the parallel beam X-ray CT geometry presented in Figure 4.2 (inspired from [46]). The X-rays are incident at an angle θ with the x-axis. Let $f(x, y)$ be a spatial function representing the absorption values of the cross-section at any point (x, y) and $g_\theta(\rho)$ be the obtained one-dimensional profile. The intensity at a point, $g_\theta(\rho_j)$ (Figure 4.2), on the one-dimensional profile can be viewed as the total absorption suffered by the X-ray beam impinging that point. The total absorption is given as the line integral along the line $x \cos \theta + y \sin \theta = \rho_j$. The line integral is mathematically expressed as:

$$g_\theta(\rho_j) = \int_{-\infty}^{\infty} \int_{-\infty}^{\infty} f(x, y) \delta(x \cos \theta + y \sin \theta - \rho_j) dx dy \quad (4.1)$$

where, $\delta(t)$ is an impulse function given as:

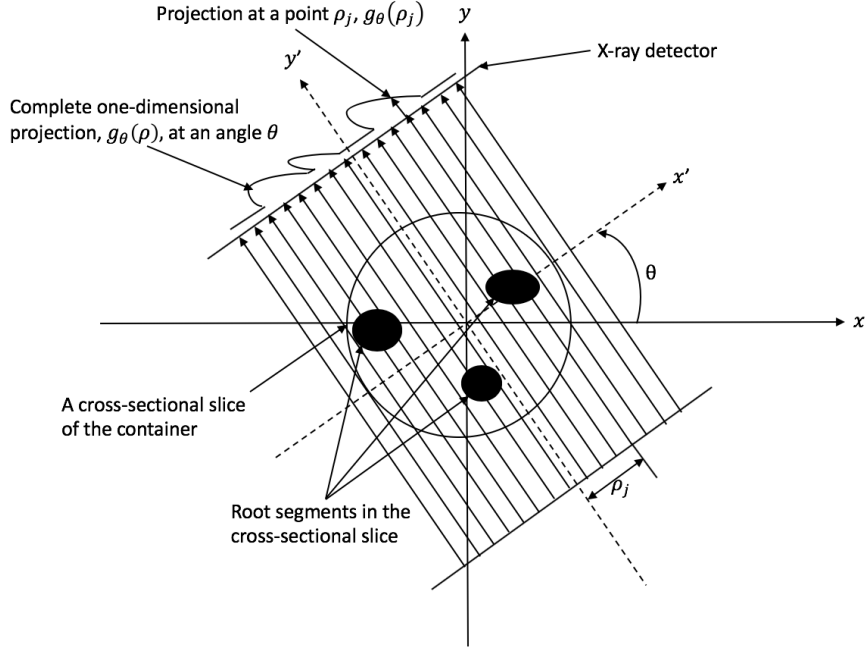


Figure 4.2: Geometry of a parallel-ray beam

$$\delta(t) = \begin{cases} \infty, & \text{if } t = 0 \\ 0, & \text{if } t \neq 0 \end{cases} \quad (4.2)$$

The impulse function, $\delta(t)$, ensures that the sum is performed only along the line $x \cos \theta + y \sin \theta = \rho_j$.

Generalizing it to any point ρ on the one-dimensional signal, the Equation 4.1 can be restated as:

$$g_\theta(\rho) = \int_{-\infty}^{\infty} \int_{-\infty}^{\infty} f(x, y) \delta(x \cos \theta + y \sin \theta - \rho) dx dy \quad (4.3)$$

This equation, which gives the one-dimensional projection of $f(x, y)$ is regarded as the *Radon transform* [46].

4.1.2 Fourier transform and Fourier-slice theorem

A fundamental concept behind reconstructing a cross-sectional slice from its one-dimensional projections is the *Fourier-slice theorem*. A brief introduction of Fourier transform is required to understand the Fourier slice theorem. The basic idea behind the Fourier transform is that any continuous function $f(t)$, often referred as a function of time (t), can be expressed as an integral of sines and/or cosines [46, 76, 77]. The Fourier transform decomposes the function into the frequencies of the sines and/or cosines that make up the function [46, 76, 77]. The decomposed representation is called as a frequency domain representation. The following equation defines the Fourier transform of $f(t)$:

$$F(\mu) = \int_{-\infty}^{\infty} f(t) e^{-j2\pi\mu t} dt \quad (4.4)$$

where, μ is a continuous variable representing frequency.

The original function, $f(t)$, can be recovered without any loss of information from its frequency domain representation through an inverse Fourier transform [46, 76]. The inverse Fourier transform is written as:

$$f(t) = \int_{-\infty}^{\infty} F(\mu) e^{j2\pi\mu t} d\mu \quad (4.5)$$

Similarly, the Fourier and inverse Fourier transforms of a two-dimensional function $f(t, z)$ are given by the expressions

$$F(u, v) = \int_{-\infty}^{\infty} \int_{-\infty}^{\infty} f(t, z) e^{-j2\pi(ut+vz)} dt dz \quad (4.6)$$

and

$$f(t, z) = \int_{-\infty}^{\infty} \int_{-\infty}^{\infty} F(u, v) e^{j2\pi(ut+vz)} du dv \quad (4.7)$$

where u and v are the frequency variables. The variables t and z are interpreted as two-dimensional spatial variable when referring to images.

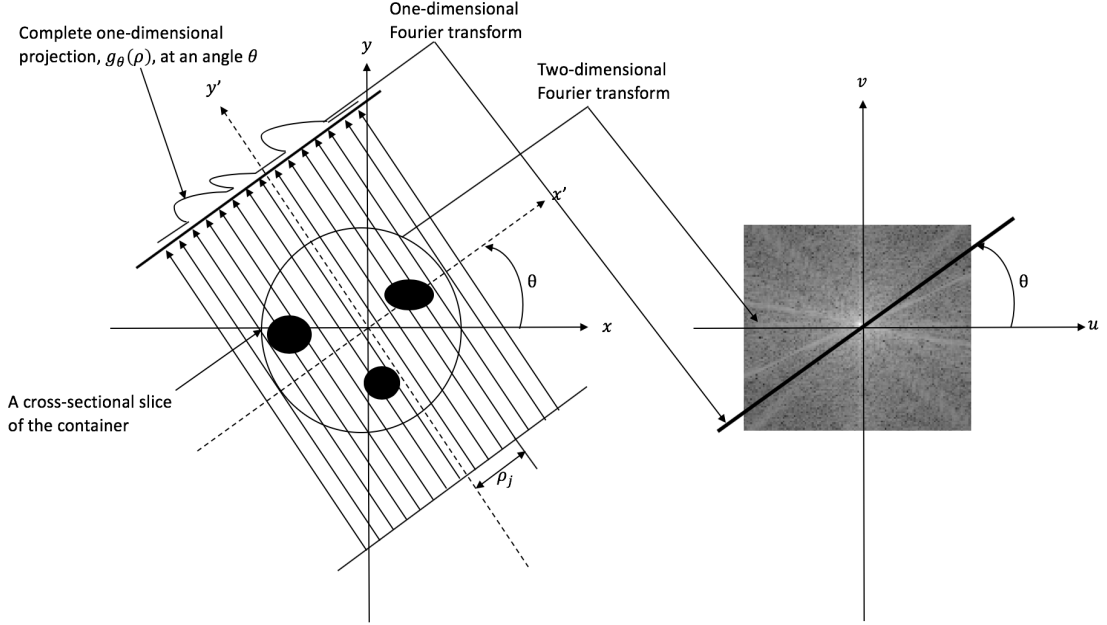


Figure 4.3: Illustration of Fourier-slice theorem.

The Fourier-slice theorem states that the one-dimensional projection $g_\theta(\rho)$ of the two-dimensional function $f(x, y)$ acquired at an angle θ can also be obtained by extracting the values of $F(u, v)$ along the line, $v = u \tan \theta$, passing through the origin and oriented at an angle θ (Figure 4.3) [46]. That is,

$$G_\theta(\omega) = [F(u, v)]_{v=u \tan \theta} = F(\omega \cos \theta, \omega \sin \theta) \quad (4.8)$$

where, $F(u, v)$ denotes the two-dimensional Fourier transform of $f(x, y)$, ω is the frequency variable ($\omega = \sqrt{u^2 + v^2}$), and $(\omega \cos \theta, \omega \sin \theta)$ represent the set of points along the line $v = u \tan \theta$. $G_\theta(\omega)$ is the one-dimensional Fourier transform of the projection $g_\theta(\rho)$, given as

$$G_\theta(\omega) = \int_{-\infty}^{\infty} g_\theta(\rho) e^{-j2\pi\omega\rho} d\rho \quad (4.9)$$

4.1.3 Filtered back projection

Assuming that $F(u, v)$ is given, an inverse Fourier transform reconstructs $f(x, y)$ as

$$f(x, y) = \int_{-\infty}^{\infty} \int_{-\infty}^{\infty} F(u, v) e^{j2\pi(ux+vy)} du dv \quad (4.10)$$

using the polar coordinate representation of (u, v) . The Equation 4.10 is restated as

$$f(x, y) = \int_0^{2\pi} \int_{-\infty}^{\infty} \omega F(\omega \cos \theta, \omega \sin \theta) e^{j2\pi\omega(x \cos \theta + y \sin \theta)} d\omega d\theta \quad (4.11)$$

Then using the Fourier-slice theorem,

$$f(x, y) = \int_0^{2\pi} \int_{-\infty}^{\infty} \omega G_\theta(\omega) e^{j2\pi\omega(x \cos \theta + y \sin \theta)} d\omega d\theta \quad (4.12)$$

Based on the fact that the one-dimensional projections obtained at angles θ and $\theta + 180^\circ$ are mirror images of each other [46], i.e., $G_\theta(\omega) = G_{\theta+180^\circ}(-\omega)$, Equation 4.12 can be expressed as

$$f(x, y) = \int_0^\pi \int_{-\infty}^{\infty} |\omega| G_\theta(\omega) e^{j2\pi\omega(x \cos \theta + y \sin \theta)} d\omega d\theta \quad (4.13)$$

In the integration with respect to ω , the term $x \cos \theta + y \sin \theta$ is a constant, which we recognize as ρ , from the equation of a line $x \cos \theta + y \sin \theta = \rho$. Thus, Equation 4.13 can be written as:

$$f(x, y) = \int_0^\pi \left[\int_{-\infty}^{\infty} |\omega| G_\theta(\omega) e^{j2\pi\omega\rho} d\omega \right]_{\rho=x \cos \theta + y \sin \theta} d\theta \quad (4.14)$$

The inner integral is the one-dimensional inverse Fourier transform (see Equation 4.5), with an added ramp filter function ($|\omega|$). The above equation states that the reconstruction of a cross-section from its one-dimensional projections involves following steps.

1. Obtain Fourier transform of one-dimensional projections.
2. Multiply the transformed signals with a windowed ramp filter; we have used Hann windowing in our work.
3. Compute inverse Fourier transform of the filtered projections.
4. Integrate (sum) all the inverse transforms from step 3.

Figure 4.4 shows the reconstructed slice of sinogram (Figure 4.1). The reconstructed cross-section contains several CT artifacts (noise), namely, ring artifacts, and streak artifacts. Ring artifacts appear as bright and dark rings centered on the axis of rotation. A defective X-ray detector creates these rings [78]. Fixing the detector reduces such artifacts. Streak artifacts appear as bright and dark streaks between two high attenuating objects (roots). These streaks appear due to the scattering of X-rays. Using an anti-scatter grid or estimating the scatter and subtracting it from the detector measurements reduces streak artifacts [78].

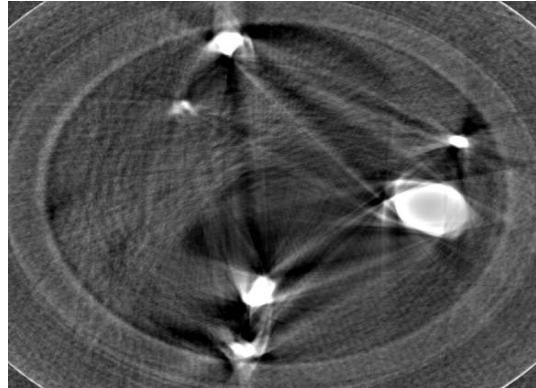


Figure 4.4: Reconstructed cross-section through filter back projection

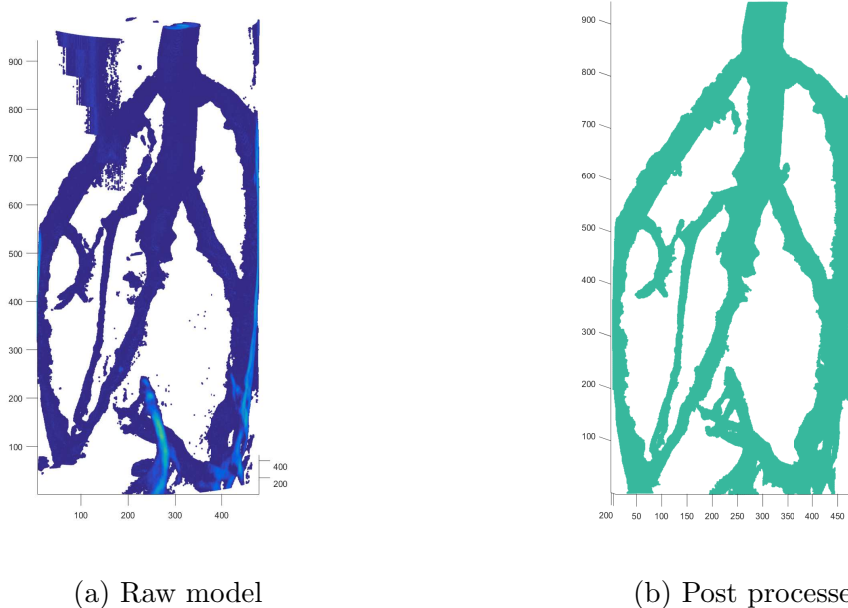


Figure 4.5: Three-dimensional model generated though filter back projection

4.2 Three-dimensional model generation

The cross-sectional images corresponding to the complete root system are generated through the filtered back projection mechanism as discussed in the previous section. The cross-sectional images are stacked in the z-direction to create a three-dimensional image set. The image set is thresholded to extract a three-dimensional model of the root system (Figure 4.5a). The threshold value is selected manually. It is noticeable that the three-dimensional model contains a lot of noise (a result of CT artifacts), specifically, around the container edges. Assuming that root segments are a giant group of pixels that follow three-dimensional connectivity, a connected component analysis is performed in three-dimensions using MATLAB function `bwconncomp()` [79]. The largest component is retained to isolate the root system architecture. Figure 4.5b presents the three-dimensional model after noise removal.

Chapter 5

Results and Analysis

This chapter discusses the effectiveness of the proposed methods on root system enhancement. Since template matching is the core of the proposed matched-guided filtering and multi-scale matched filtering, experiments are conducted to understand the effect of changing different parameters of the two-dimensional matched filter on root system enhancement, segmentation, and three-dimensional model generation. The experimental results and conclusions drawn are also discussed in this chapter.

5.1 Performance analysis

The proposed root enhancement and segmentation methods are applied on two different datasets, namely, air sample, and soil sample datasets. The matched-guided filtering is applied on the air sample dataset to generate a three-dimensional model. The multi-scale matched filtering is applied on the soil sample dataset to segment roots. Since the matched filtering at a single scale (σ) could not enhance the whole root system in the images collected in soil (discussed in Section 3.3.3), the matched-guided filtering is not applied on the soil sample dataset. The results obtained from

the proposed methods are compared with the existing approaches. The following subsections provides details on the datasets used and the results obtained.

5.1.1 Air sample

The air sample dataset collected by Isaac [36] is used in this study. The dataset consists of two-dimensional projections of a Soybean plant (*Glycine max*) grown in a three-dimensional printed polyvinyl chloride (PVC) container containing soil from local fields for two weeks under controlled lab environment. Later, roots are excavated and washed with care to prevent any root breakage. The root system was placed in a PVC container with an outer diameter of 26.25cm, and an inner diameter of 22cm. The X-ray system was operated at the 40kV with an exposure time of 30 seconds. Two-dimensional projections captured from different rotational viewpoints with 1° apart produced 180 images.

To generate cross-sectional images from the 180 two-dimensional projections, matched guided filtering and filtered back projection are employed as discussed in Chapters 3, and 4. The cross-sectional images are stacked in the z-direction to obtain a three-dimensional image set which is then thresholded to extract RSA. The threshold value is selected manually. Figure 5.2b presents the frontal view of the three-dimensional model produced. Visual inspection of the model reveals that our method extracts thin roots along with the thick ones. Even though the overall root structure is preserved, the model is not entirely consistent with the two-dimensional projections. The root segments are broader in the three-dimensional model compared to the two-dimensional counterparts. A two-dimensional planar projection of the three-dimensional model is obtained by adding all the voxel intensities along the y-axis. Figure 5.3 presents the two-dimensional projection and the corresponding original image from the air sample dataset. It is noticeable from the figure that the root segments appear broader in the two-dimensional projection obtained from the

model compared to the original image. We believe that a slight tilt in the positioning of the container from projection to projection is resulting in overestimating the width of the root segments.

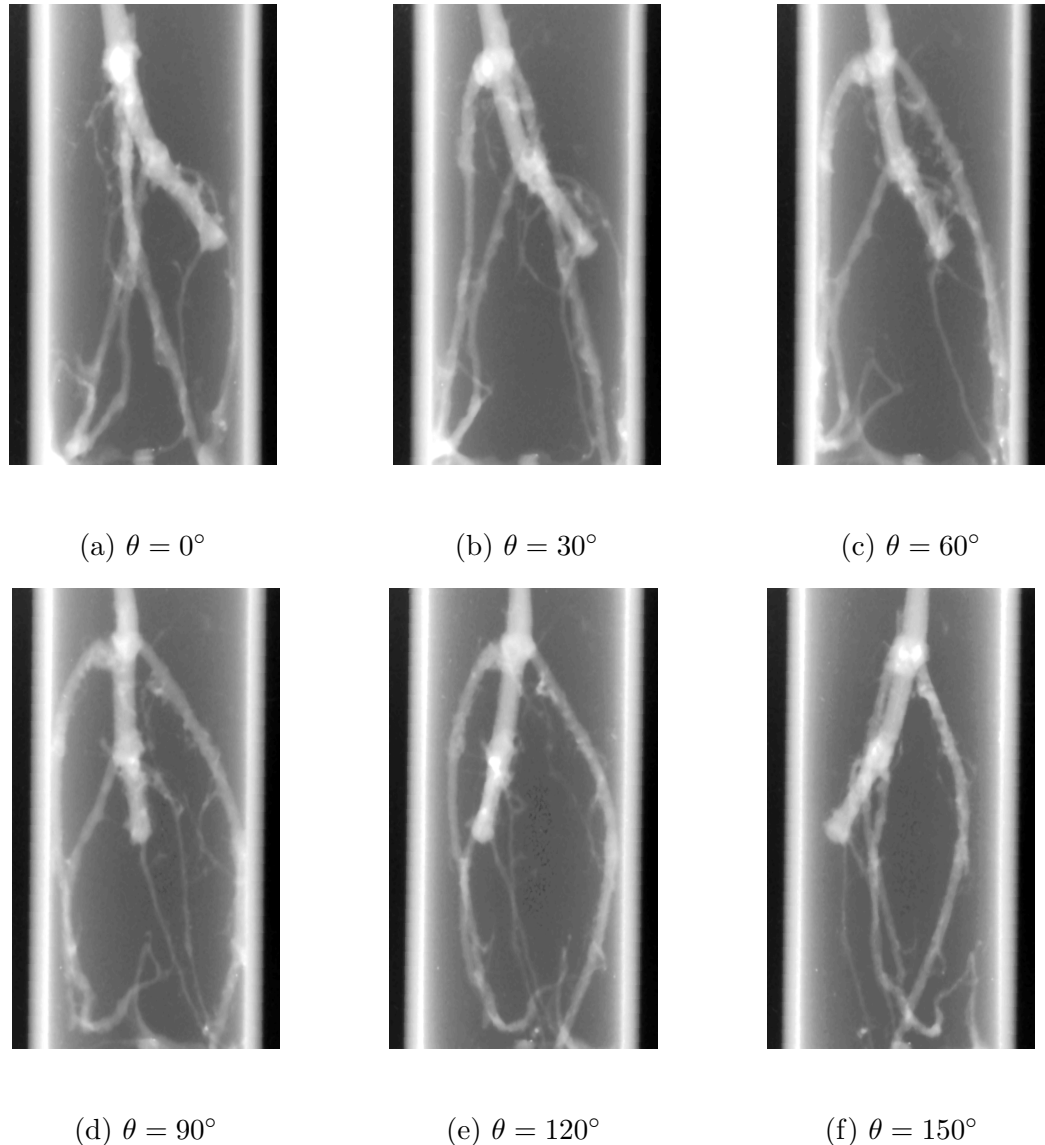


Figure 5.1: Example images from the air sample dataset. The plant root images are captured from different rotational viewpoints using the X-ray system.

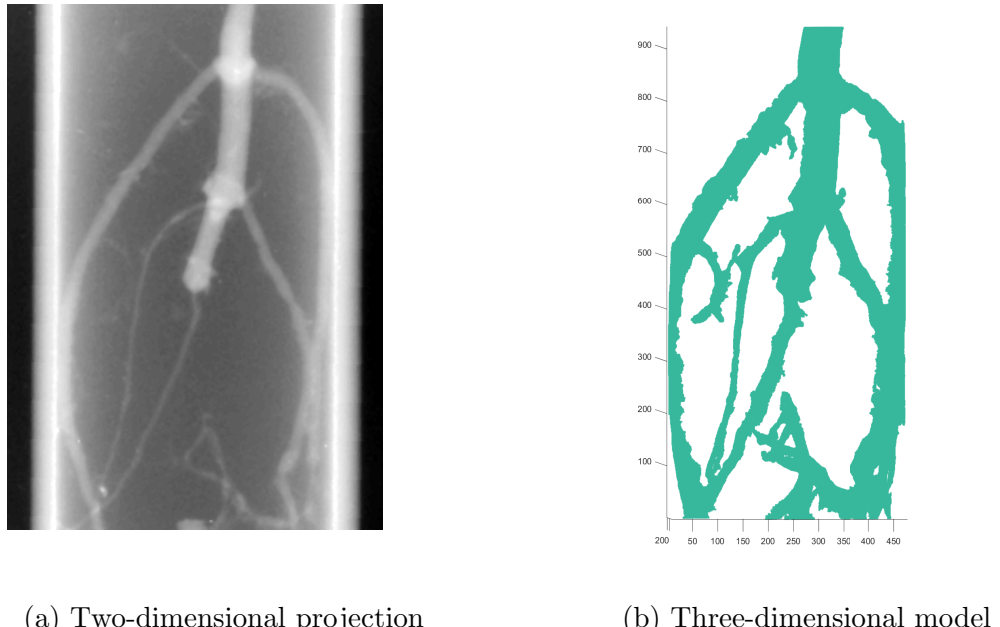


Figure 5.2: Generated three-dimensional model through the proposed pipeline of matched-guided filtering and filtered back projection..

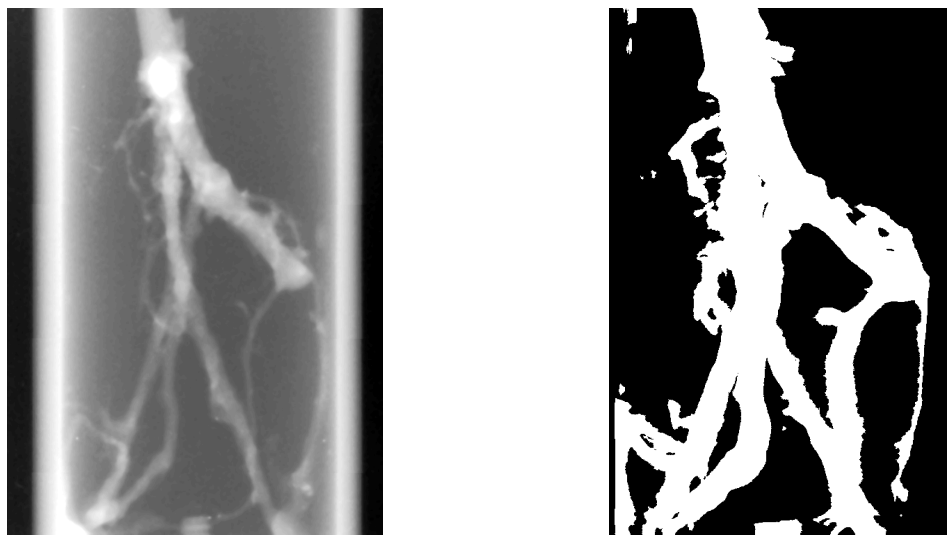


Figure 5.3: Comparison of two-dimensional projections. (a) Original two-dimensional projection from the dataset. (b) Two-dimensional projection obtained from the three-dimensional model.

To compare the accuracy of the three-dimensional reconstruction obtained through the proposed matched-guided filtering and filtered back projection mechanism with

other approaches, we generated a three-dimensional model using the latest version of the RooTrak software [32,33]. RooTrak employs a top-down approach and uses visual tracking of the root cross-sections in the z-direction, starting from a manually selected seed point in the top image. We provided RooTrak with two sets of cross-sectional images. The cross-sectional image set obtained after matched and guided filtering is the first set. Filtered back projection of the raw images without any preprocessing yielded the other collection. Figure 5.4 shows the cross-sectional images from the first set, while Figure 5.6 presents the slices from the second set. Selecting the brightest pixel in the top slice as a seed point initiated tracking. Figures 5.5 and 5.7 presents the RooTrak results from both sets. RooTrak could not process both of the datasets. Due to a variation in the root pixels' intensity, RooTrak could not completely identify the root segments within a slice, and gradually lost track of the root segments as the image stack was traversed. Additionally, it did not identify the branched out roots. The variation in intensity is because of the low-energy (30kV-40kV) X-ray imaging and using few (180) projections for generating cross-sectional slices. Mairhofer et al. [32,33] used an industrial μ CT operating at high energy (80kV - 130kV) to image roots. Additionally, they collected ≥ 1200 two-dimensional projections, whereas we obtained less than one-sixth of the projections (180) at a lower energy level (40kV).

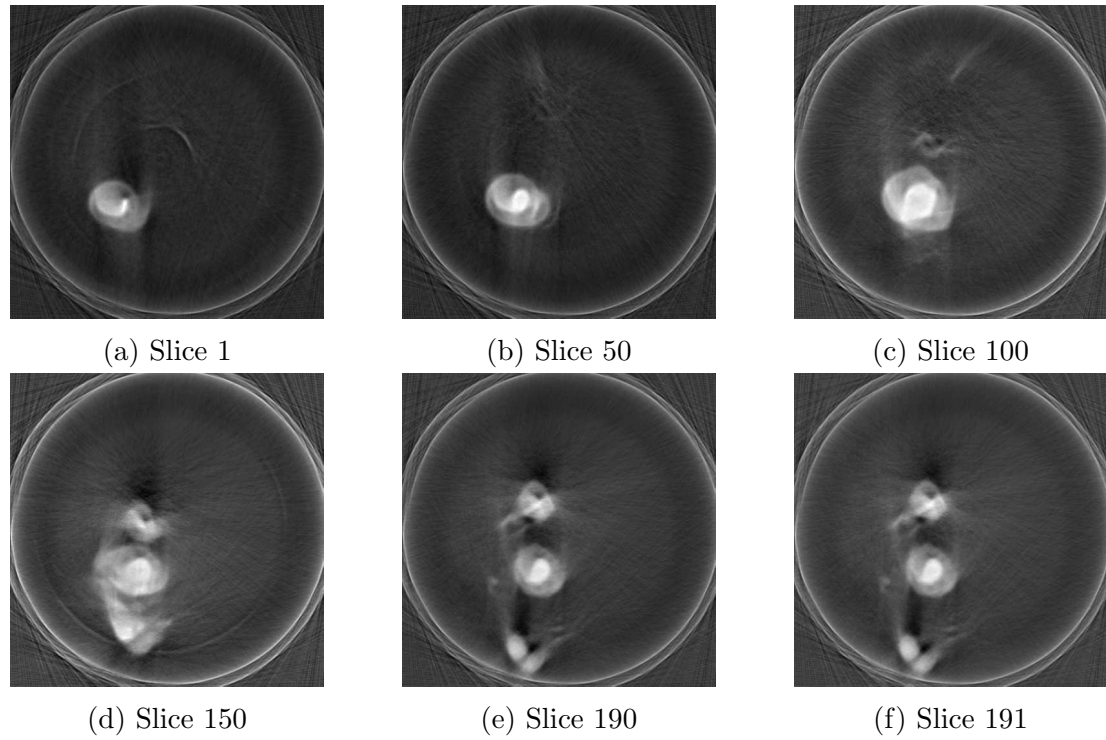


Figure 5.4: Cross-sectional slices generated from the pre-processed images.

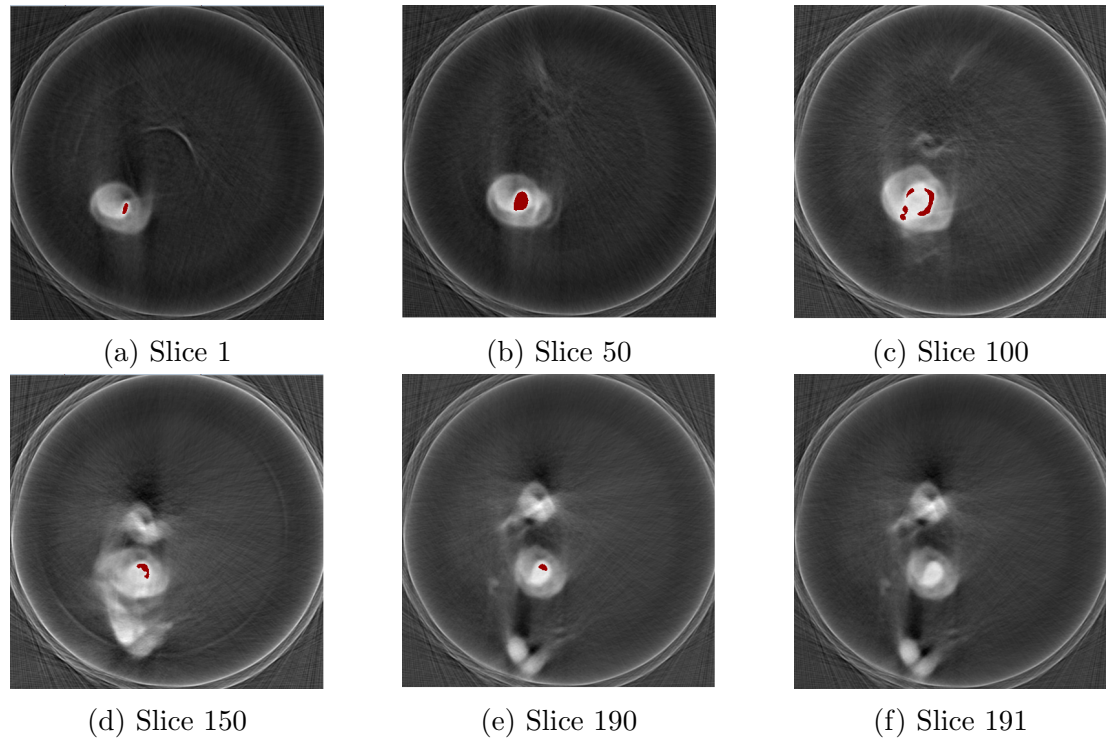


Figure 5.5: Extracted root (*highlighted in brown*) in each slice through RooTrak.

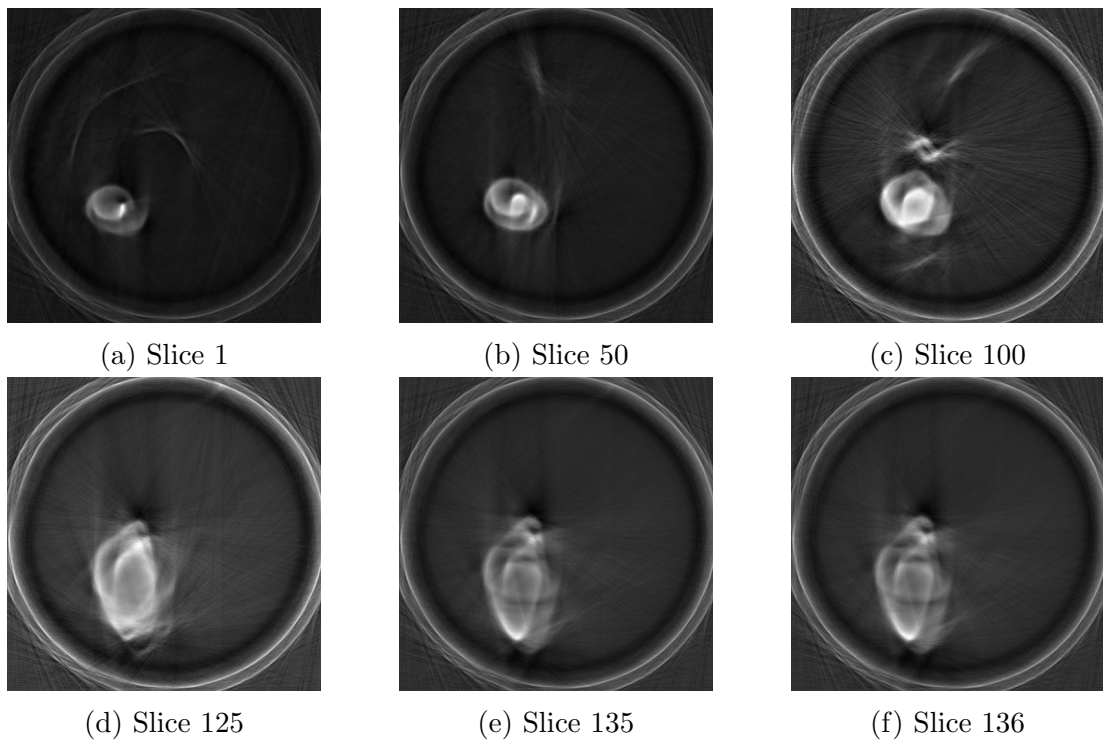


Figure 5.6: Cross-sectional slices generated from the raw images.

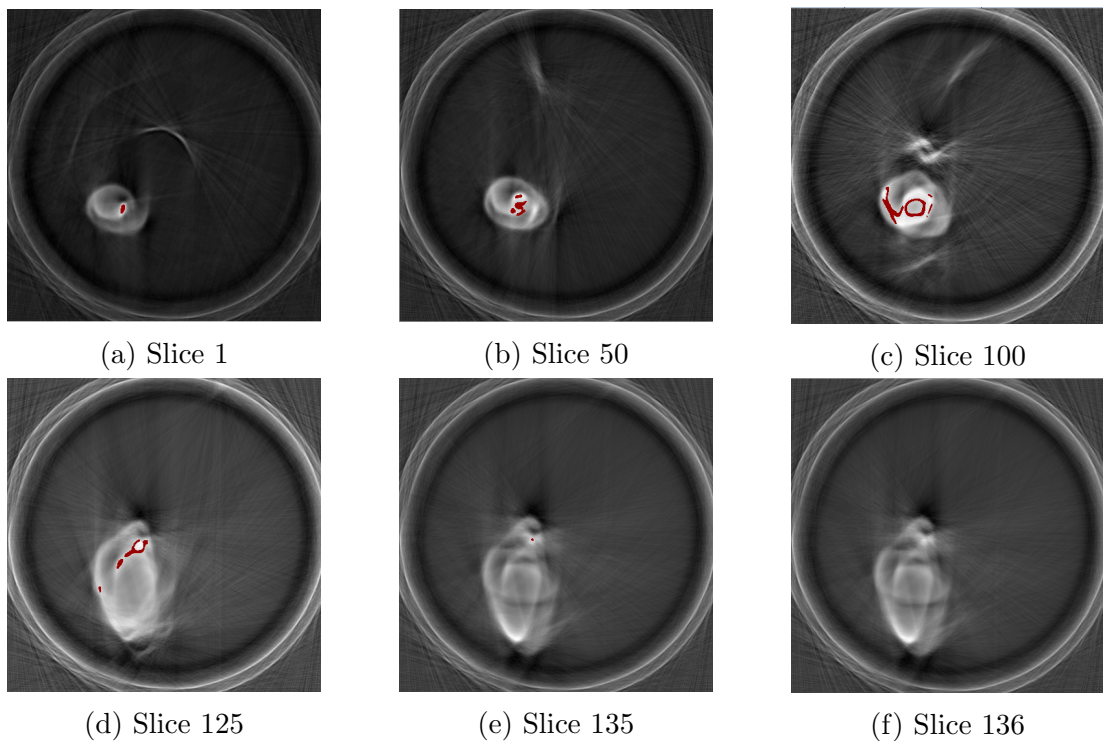


Figure 5.7: Extracted root (*highlighted in brown*) in each slice generated from the raw images through RooTrak.

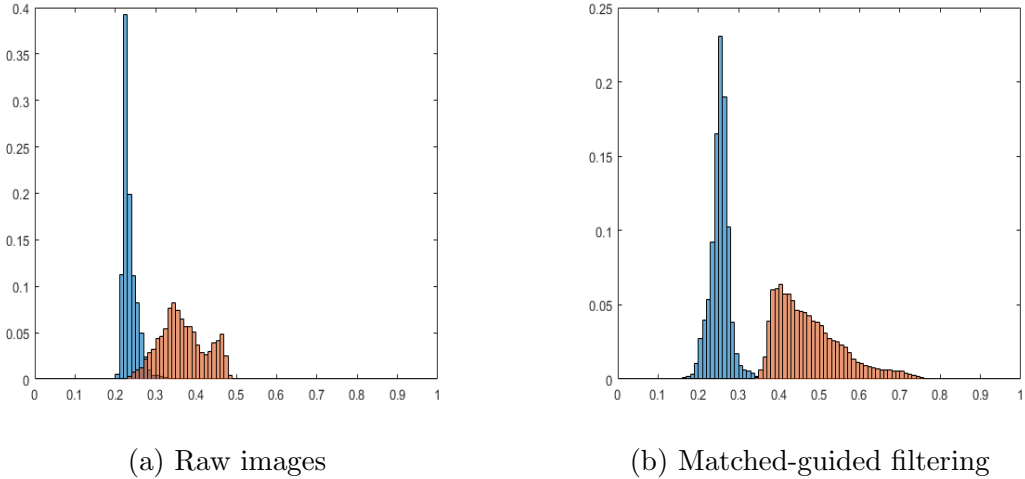


Figure 5.8: Probability density functions of voxel intensities corresponding to root (*orange*) and background (*blue*) in the three-dimensional models.

To quantitatively evaluate the accuracy of a plant root’s three-dimensional model, existing studies [17, 26, 28, 34, 35, 44] have compared manually extracted phenotypical features with the traits obtained from the three-dimensional model. As the imaged root was not accessible, we could not follow this approach in our study. However, the core part of the matched-guided filtering algorithm is the root segments enhancement in the low-energy X-ray images. Therefore, the quantitative metric in this research measures the contrast between root and background in the three-dimensional model.

An intersection measure (S_{IS}) between the intensity distributions of the root and the background is considered as a contrast measure. It is mathematically expressed as:

$$S_{IS} = \sum_i \min(p_i, q_i) \quad (5.1)$$

where, p and q are intensity distributions. If two distributions overlap entirely, S_{IS} would be 1. If there is no overlap, S_{IS} would be 0. So, if the contrast between the root and the background is low, their distributions will overlap significantly, and S_{IS} would be high. Otherwise, S_{IS} would be low.

	μ_{IS}	σ_{IS}
Raw images	0.099	0.0106
Matched-guided filtering	0.0036	0.0016

Table 5.1: Contrast metrics obtained from the three-dimensional models generated from raw images and the proposed matched-guided filtering method.

The raw images, as well as the enhanced images, were filtered back projected to generate three-dimensional models. Five hundred $5 \times 5 \times 5$ voxel cubes belonging to root and background were sampled from the three-dimensional models, and their intensity histograms were computed. The sampling process is repeated a hundred times to obtain an estimate of the contrast measure. Since there was no existing method to obtain a ground-truth three-dimensional model of the plant root, the model shown in Figure 5.2b was treated as a ground-truth in determining root and background voxel cubes. First, the voxel cubes belonging to the root were sampled from the ground-truth model, and their coordinates were found. Later, the voxel cube intensities at these coordinates from a three-dimensional model were recorded to give root intensity histogram for that model. The background voxel intensity histograms of a model was obtained similarly. Figure 5.8 presents the intensity histograms from both of the models. Table 5.1 reports the computed estimates of mean (μ_{IS}) and standard deviations (σ_{IS}) of contrast measures (Equation 5.1) obtained from these models. The significant overlap in root and non-root intensity histograms in Figure 5.8a (μ_{IS} of 0.099) compared to the distributions in Figure 5.8b (μ_{IS} of 0.0036) indicate that the proposed matched-guided filtering has improved the contrast between root and background considerably.

5.1.2 Soil sample

The soil sample dataset collected by Isaac [36] is used in this study. The dataset consists of two-dimensional projections of three Soybean plants grown in field soils

for two weeks in laboratory controlled environment. The roots were excavated and washed to extract the root systems. Each plant root system was imaged in a three-dimensional printed PVC containers containing different soil types, namely topsoil, Haymond silt loam soil (rolling bottom soil), and soil from local field. The PVC containers were with an inner and outer diameter of 30mm and 34.25mm respectively. The roots were imaged using a lab-built X-ray system operated at three different energy levels, namely 30kV, 35kV, and 40kV [36]. The dataset contains nine images, one image per every soil and energy level combination. Figure 5.9 shows the plant root images obtained in topsoil. The plant root images collected in Haymond silt loam soil (rolling bottom soil) are shown in Figure 5.10. Figure 5.11 displays a plant root's pictures obtained in field soil. Due to the low X-ray energy levels, the acquired images have a low signal-to-noise ratio (SNR), severely corrupted with noise and have blurry edges. Additionally, the soil is filled in the container after placing the root, resulting in the formation of pores due to which some soil pixels have attenuation values similar to that of the root. This effect can be observed clearly in the edges of the image. The edges have a lot of pores hence, a lot of bright pixels, some background pixels are even brighter than the root pixels.



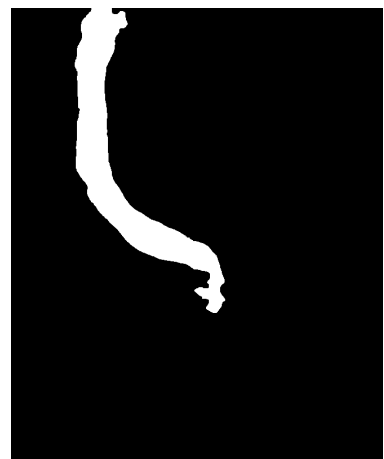
(a) 30kV



(b) 35kV



(c) 40kV



(d) Manual segmentation

Figure 5.9: A plant root imaged in top soil at different energy levels.



(a) 30kV



(b) 35kV



(c) 40kV



(d) Manual segmentation

Figure 5.10: A plant root imaged in rolling bottom soil at different energy levels.

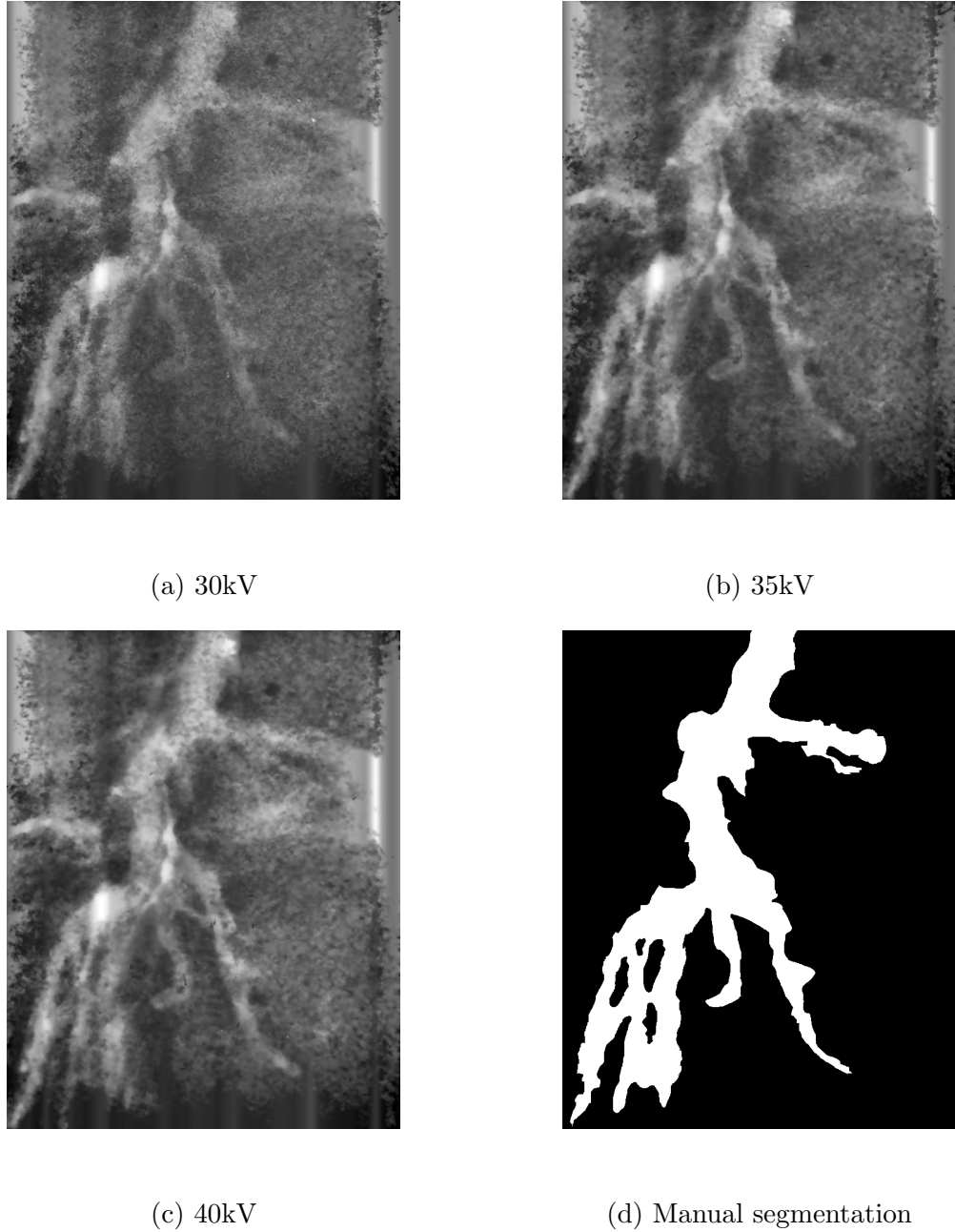


Figure 5.11: A plant root imaged in filtered field soil at different energy levels.

The multi-scale matched filtering method, proposed in Chapter 3, is employed to highlight and segment the root systems in the image set. Figures 5.12, 5.13, and 5.14 show the enhanced versions of Figures 5.9, 5.10, and 5.11 respectively. To provide a quantitative metric for the effect of the proposed image enhancement and segmentation methods, a human expert has manually labeled the images. Figures

5.9, 5.10, and 5.11 are presented with these manually labeled images. Due to the poor quality of images, a human expert might not have identified the complete root system. Some portion of the RSA might be missing in the human labeled data.

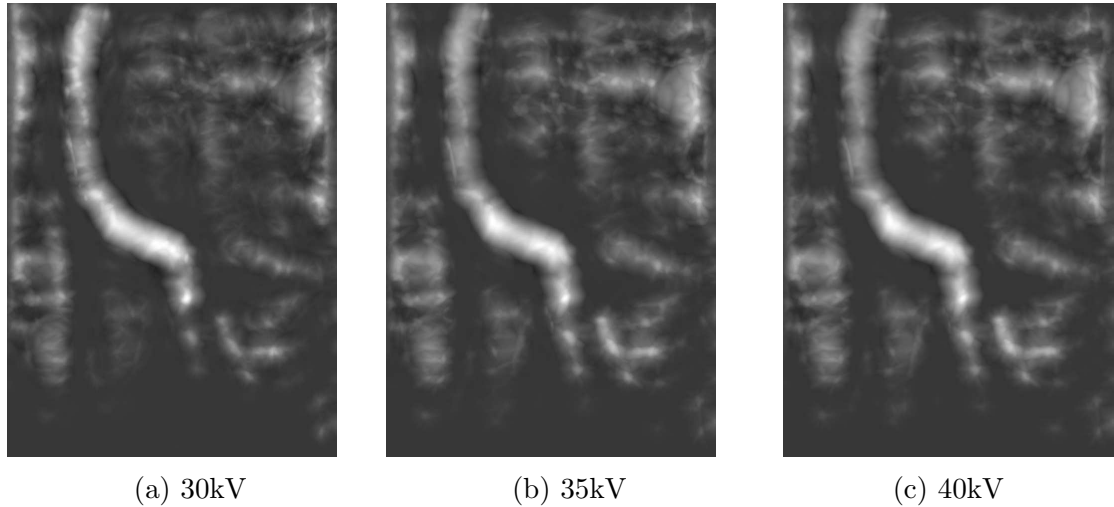


Figure 5.12: Enhanced root segments in top soil images following the proposed multi-scale matched filtering.

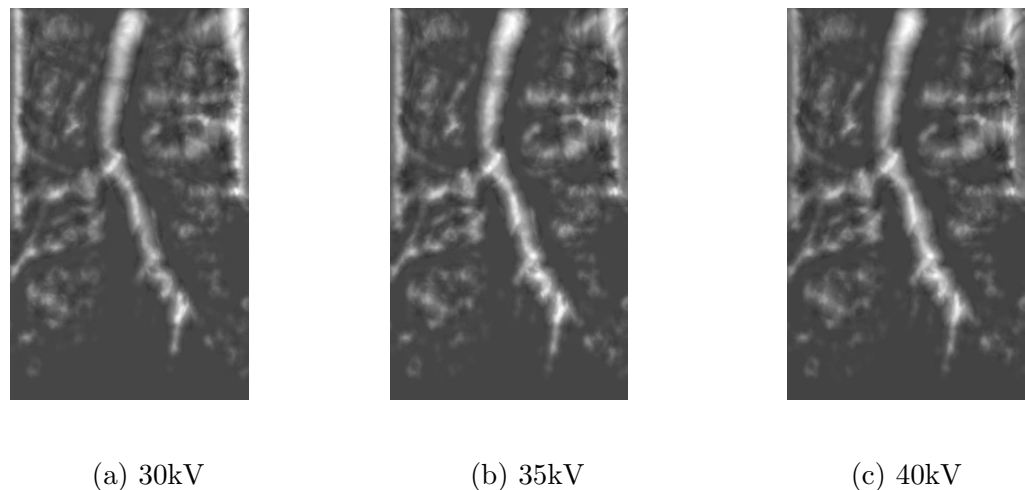


Figure 5.13: Enhanced root segments in rolling bottom soil images following the proposed multi-scale matched filtering.

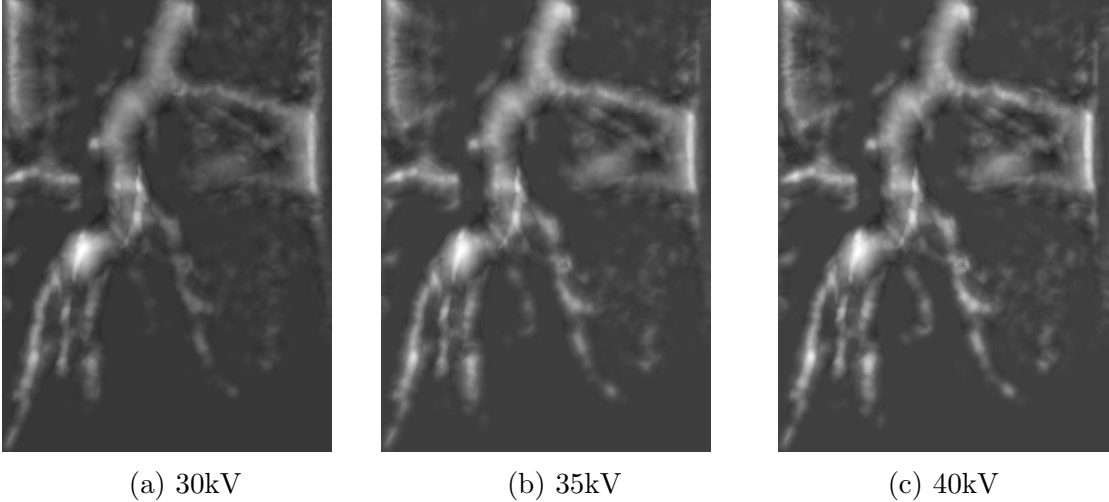


Figure 5.14: Enhanced root segments in filtered field soil images following the proposed multi-scale matched filtering.

With multi-scale matched filtering, the goal is to enhance the roots by magnifying the intensity difference between the root and the soil. To demonstrate the effect of our enhancement mechanism, we drew Receiver operating characteristic (ROC) curves for the entire image set, before and after the enhancement. ROC curves provide a graphical way to visualize the achieved discrimination between two classes (root and soil). The area under the curve (AUC) of ROC provides a quantitative measure of the discrimination achieved. As the area under the curve increases, the distinction achieved through enhancement also increases. The ROC curve is a plot of true positive rate (TPR) [80, 81] against the false positive rate (FPR) [82, 83] at various threshold settings. The enhanced image is binarized at different threshold levels and is compared to the manually segmented image to calculate TPR and FPR values. Figures 5.15, 5.16, and 5.17 show these ROC curves. Table 5.2 presents the AUCs for corresponding to the image set. From the figures, it is noticeable that the enhanced images have better curves than the raw images. The higher values of AUCs (Table 5.2) for enhanced images support this.

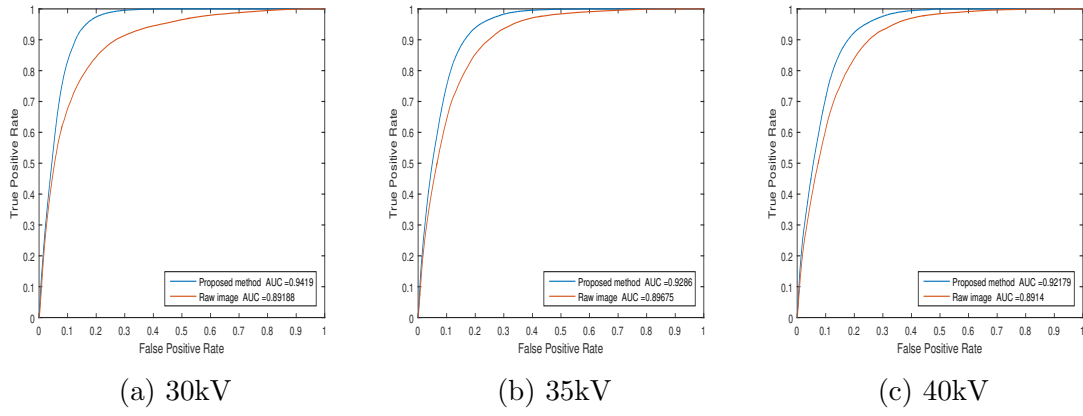


Figure 5.15: ROC curves corresponding to top soil images enhanced with multi-scale matched filtering.

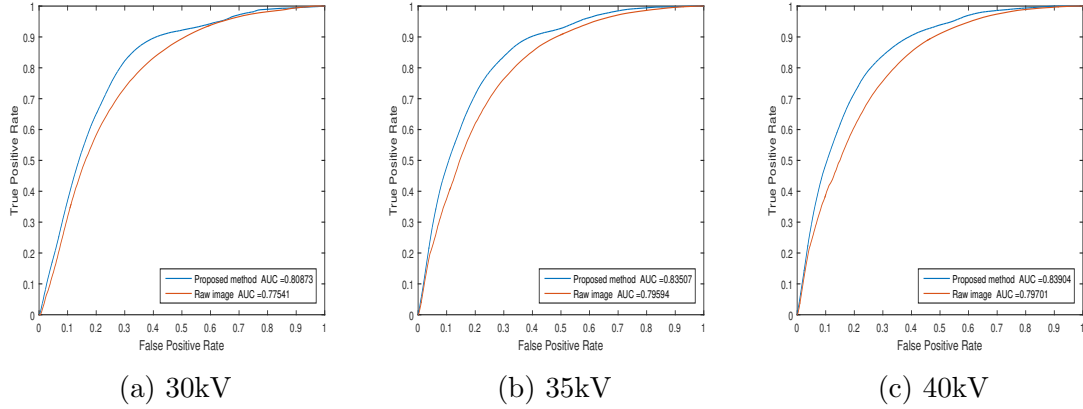


Figure 5.16: ROC curves corresponding to rolling bottom soil images enhanced with multi-scale matched filtering.

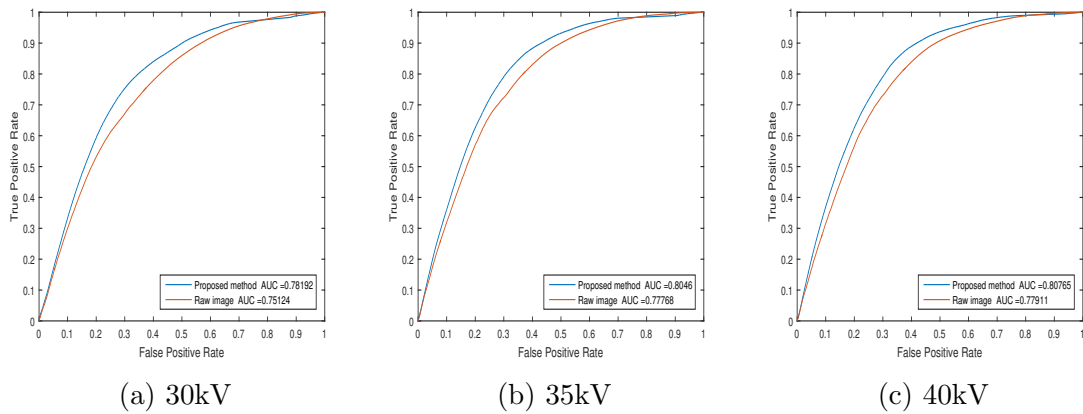


Figure 5.17: ROC curves corresponding to filtered field soil images enhanced with multi-scale matched filtering.

Soil Type	Energy Level	Area under the curve (AUC)	
		Raw image	Enhanced image
Top Soil	30kV	0.892	0.942
	35kV	0.897	0.930
	40kV	0.892	0.922
Rolling Bottom Soil	30kV	0.775	0.810
	35kV	0.795	0.835
	40kV	0.80	0.840
Filtered Field Soil	30kV	0.751	0.782
	35kV	0.778	0.805
	40kV	0.780	0.808

Table 5.2: Area under the ROC curve for raw images and images enhanced with the proposed multi-scale matched filtering method.

Soil Type	Energy Level	Otsu's thresholding			Multi-scale matched filtering		
		TPR	FPR	F1 score	TPR	FPR	F1 score
Top Soil	30kV	0.958	0.433	0.225	0.927	0.010	0.875
	35kV	0.978	0.412	0.238	0.870	0.001	0.838
	40kV	0.976	0.404	0.242	0.874	0.015	0.823
Rolling Bottom Soil	30kV	0.855	0.370	0.394	0.678	0.087	0.751
	35kV	0.845	0.321	0.423	0.800	0.106	0.764
	40kV	0.841	0.318	0.424	0.816	0.115	0.815
Filtered Field Soil	30kV	0.779	0.305	0.519	0.640	0.009	0.669
	35kV	0.808	0.268	0.562	0.686	0.016	0.720
	40kV	0.812	0.261	0.569	0.780	0.020	0.720
Average		0.872	0.344	0.4	0.786	0.042	0.775

Table 5.3: Performance measures for Otsu's thresholding and proposed multi-scale matched filtering method.

As mentioned earlier, the images have a lot of noise. Matched filtering with a Gaussian filter enhances any group of pixels exhibiting a Gaussian intensity profile, the intensity of noise pixels exhibiting such a profile is also amplified. This is evident from the enhanced images (Figures 5.12, 5.13, and 5.14), especially at the image edges. There are a large number of such noisy pixels around the image edges. This noise accounts for most of the false positives in the ROC curves. Because of this, there is only a slight gain in the AUCs (Table 5.2).

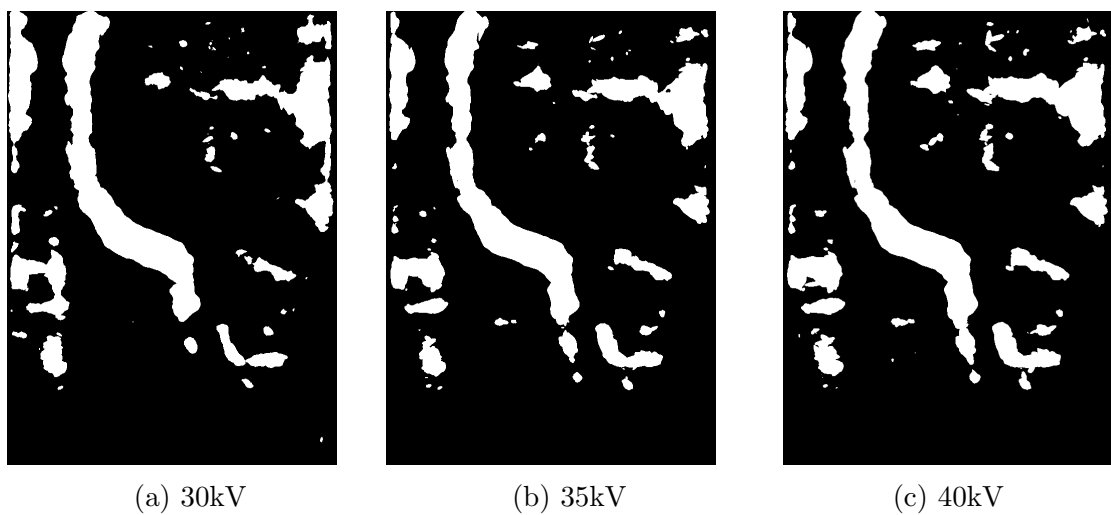


Figure 5.18: Segmented RSA from the top soil images following the proposed multi-scale matched filtering method.

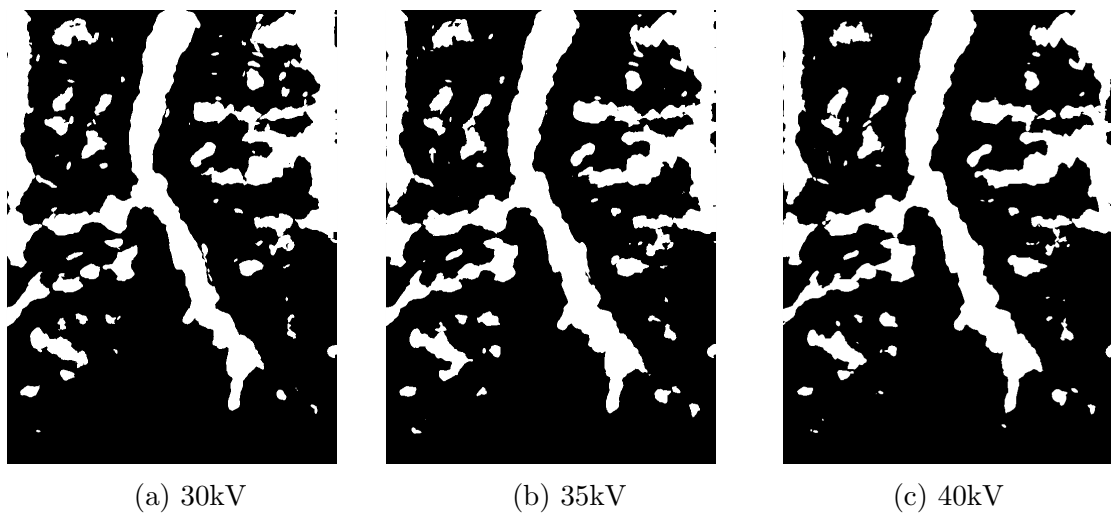
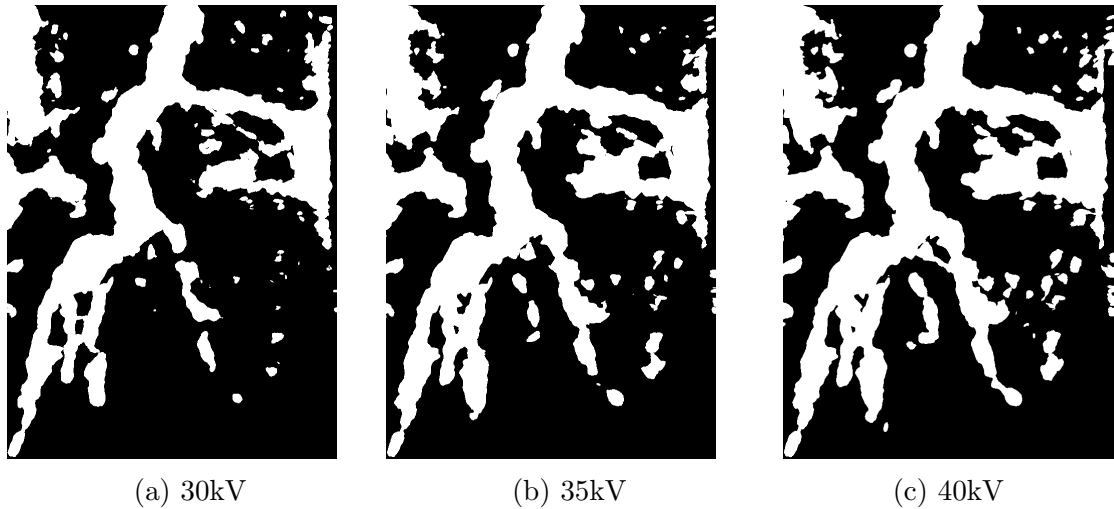


Figure 5.19: Segmented RSA from the rolling bottom soil images following the proposed multi-scale matched filtering method.

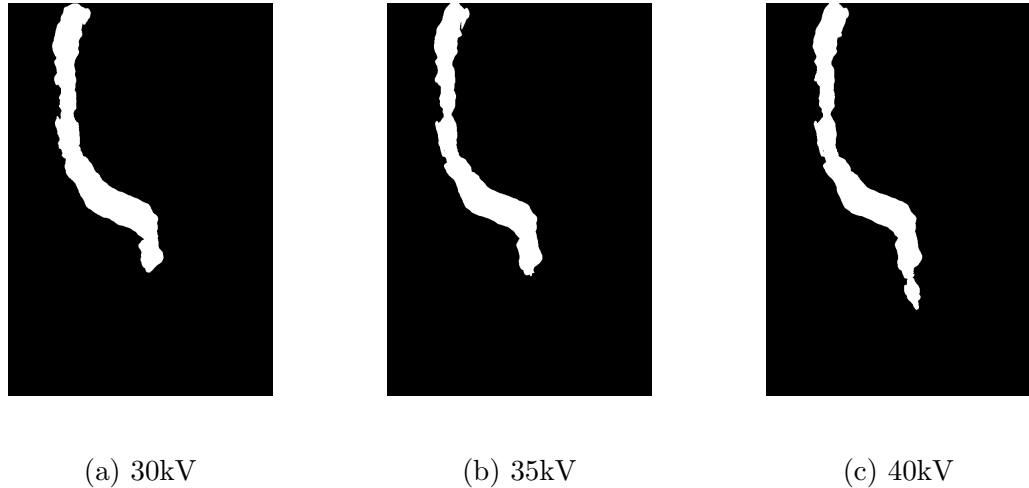


(a) 30kV

(b) 35kV

(c) 40kV

Figure 5.20: Segmented RSA from the filtered field soil images following the proposed multi-scale matched filtering method.

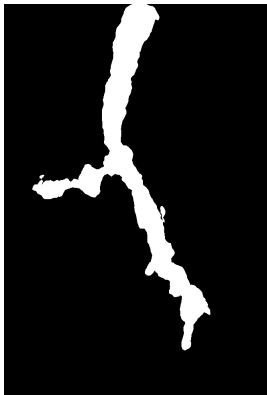


(a) 30kV

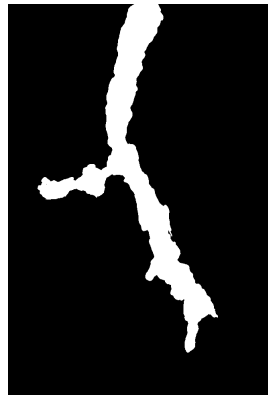
(b) 35kV

(c) 40kV

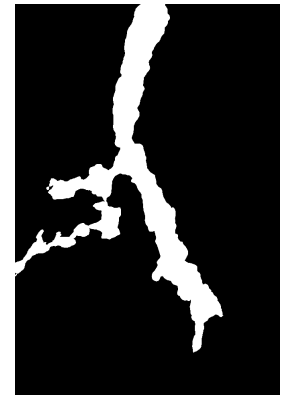
Figure 5.21: Isolated RSA from the top soil images following the proposed multi-scale matched filtering method.



(a) 30kV



(b) 35kV



(c) 40kV

Figure 5.22: Isolated RSA from the rolling bottom soil images following the proposed multi-scale matched filtering method.



(a) 30kV



(b) 35kV



(c) 40kV

Figure 5.23: Isolated RSA from the filtered field soil images following the proposed multi-scale matched filtering method.

The enhanced images are binarized by thresholding (Figures 5.12, 5.13, and 5.14) to isolate the roots from the soil. The threshold value is selected manually. The binary images contained a lot of noise along with the RSA (Figures 5.18, 5.19, and 5.20). Assuming that the root segments are larger than any noise component, and are connected to each other, the root system is extracted by keeping only the largest connected component. Figures 5.21, 5.22, and 5.23 present the obtained root struc-

tures following this approach. To provide a quantitative metric for the portion of the root system extracted, true positive rate (TPR) [80, 81] and false positive rate (FPR) [80, 83] metrics are calculated by comparing the isolated RSA from the images with the corresponding human-labeled images. For comparison purpose, the raw images (Figures 5.9, 5.10, and 5.11) are binarized through Otsu's thresholding [84] and TPR and FPR values are calculated. Table 5.3 presents the TPR and FPR values computed from both the approaches on the whole image set.

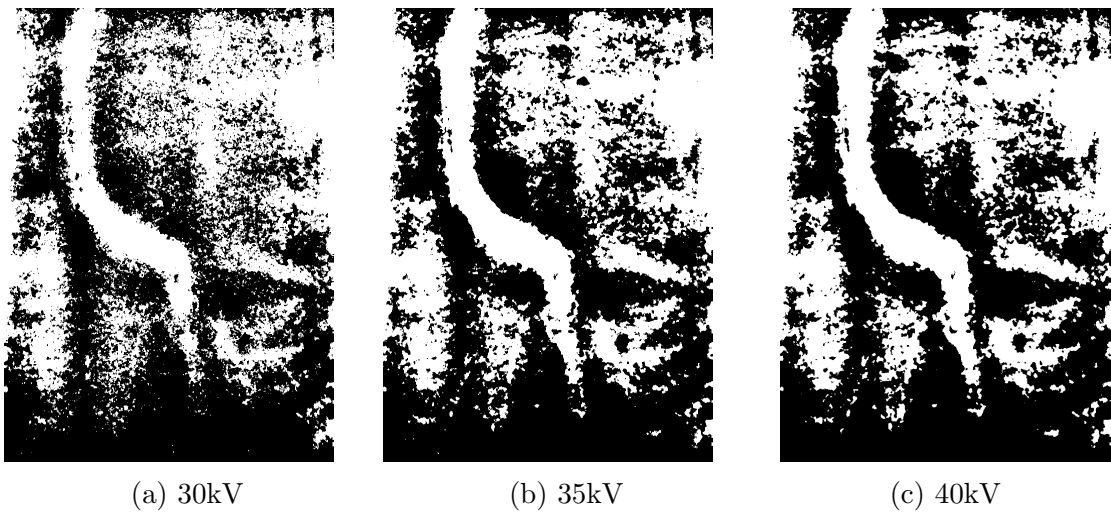


Figure 5.24: Segmentation result of top soil images obtained through Otsu's thresholding.

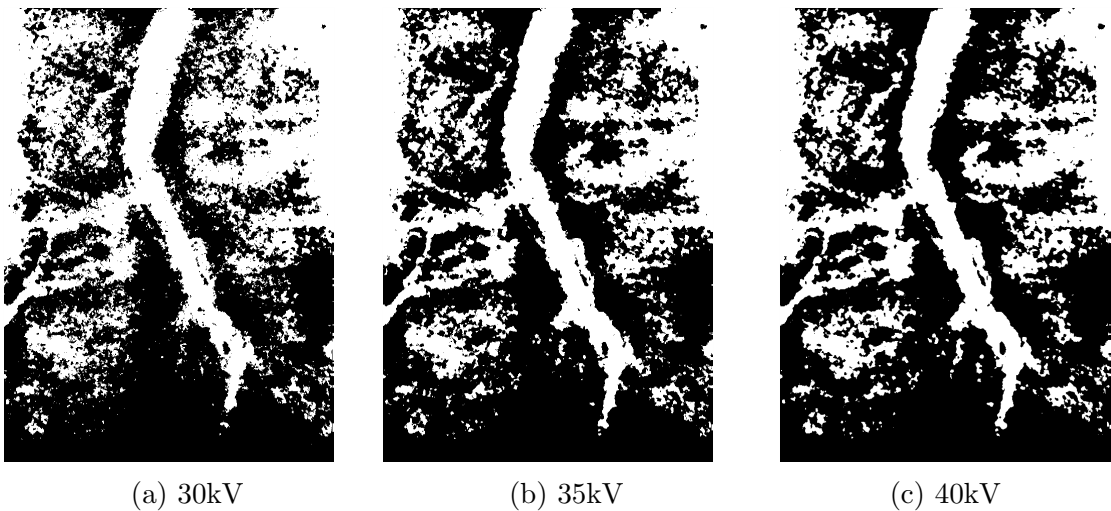


Figure 5.25: Segmentation result of rolling bottom soil images obtained through Otsu's thresholding.

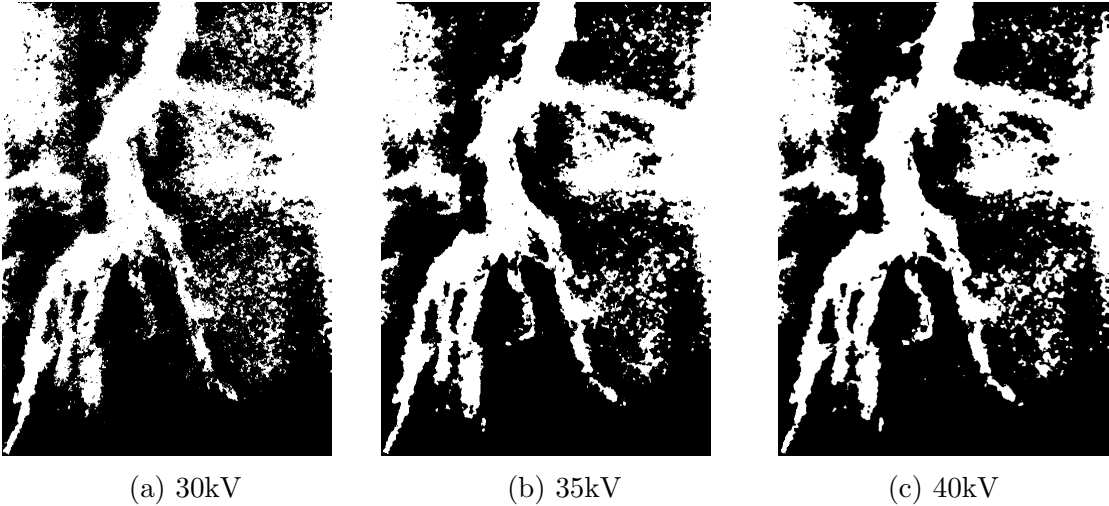


Figure 5.26: Segmentation result of filtered field soil images obtained through Otsu's thresholding.

Though Otsu's thresholding was able to extract most of the root, average TPR of 0.872, a lot of soil pixels were misclassified, average FPR of 0.344 (Table 5.3). It is clearly visible in the Figures 5.24, 5.25 5.26 that the high value of average FPR is due to the low SNR of the images and similar intensities of the root and soil pixels. Moreover, the Otsu's thresholding determines the threshold value based only on the individual pixel intensities without considering the spatial relationship between the pixels. In contrast, the proposed multi-scale matched filtering method incorporates prior knowledge of Gaussian cross-sectional intensity profile and connectivity of the root segments to isolate the RSA. Because of this, a considerable amount of root system was extracted, average TPR of 0.786, even in the low SNR images. Though the proposed method has identified less RSA compared to Otsu's approach, the false alarm rate has reduced significantly. Multi-scale matched filtering has an average FPR of 0.042, opposed to 0.344, obtained from Otsu's thresholding. As one has to consider both true positives and false alarms while comparing these methods, F_1 scores [80, 85] were calculated as well. Where the F_1 score is defined as

$$F_1 = 2 \frac{\text{precision} \times \text{recall}}{\text{precision} + \text{recall}} \quad (5.2)$$

where,

$$\text{precision} = \frac{\text{Number of correctly classified root pixels}}{\text{Number of pixels classified as root}} \quad (5.3)$$

$$\text{recall} = \frac{\text{Number of correctly classified root pixels}}{\text{Number of root pixels in the ground truth}} \quad (5.4)$$

notice that the recall is same as true positive rate. The proposed multi-scale matched filtering method has achieved an average F_1 score of 0.775 compared to 0.4 obtained from Otsu's thresholding (Table 5.3). The superior F_1 scores of proposed approach demonstrates that it outperforms Otsu's thresholding.

5.2 Experiments

The core component of the proposed matched-guided filtering and multi-scale matched filtering methods is the template matching with a two-dimensional Gaussian at different orientation and scales. Experiments are conducted to study and understand the effect of changing the number of orientational filters or angular resolution ($\Delta\theta$) and varying the filter lengths (L) on root system enhancement. This section provides the details of the experiments conducted and conclusions inferred.

5.2.1 Changing angular resolution ($\Delta\theta$)

In this set of experiments, the effect of changing the angular resolution ($\Delta\theta$) on RSA enhancement is studied. Angular resolutions $5^\circ, 10^\circ, 15^\circ, 30^\circ$, and 45° are considered for template matching in matched guided filtering and multi-scale matched filtering methods, while σ (or $\sigma_{min}, \sigma_{max}$, and $\Delta\sigma$) and L assuming constant values for the whole image set corresponding to a plant. The following subsection provides the results of experiments on plant root image datasets collected with air and soil as imaging media.

Air sample

The air sample dataset consists of 180 two-dimensional projections of a plant root, captured using the X-ray system. Air is used as an imaging media. A three-dimensional model per angular resolution under consideration is generated by applying matched-guided filtering and filtered back projection. At every angular resolution, the standard deviation (σ) and length (L) of the orientational filters are set to 9 and 11 respectively. As mentioned previously, the vital step in the proposed approach is the contrast enhancement between root and the background. So the contrast measure (Equation 5.1) is calculated from the three-dimensional models obtained at various angular resolutions. Five hundred voxels cubes of size $5 \times 5 \times 5$ belonging to the root and the background are randomly sampled to obtain the contrast measure. The sampling process is repeated a hundred times to obtain an estimate of the contrast measure. As it was not possible to generate a ground-truth three-dimensional model of the plant root, the three-dimensional model generated in the performance evaluation section (Section 5.1.1) is considered as a reference in deciding the voxels belonging to the root and the background in this experiment. Table 5.4 presents the mean(μ_{IS}) and standard deviations (σ_{IS}) of the contrast measures obtained from different three-dimensional models. It is observable that the contrast measures are very similar. The absolute difference between the maximum and minimum of the contrast measures obtained is less than 0.0007. Figure 5.27 presents the voxel intensity PDFs belonging to the root and the background. It is noticeable that the PDFs look identical. The similar contrast measures and identical PDFs at different angular resolutions indicate that the angular resolution does not have a significant effect on the root segment enhancement.

Angular resolution($\Delta\theta$)	μ_{IS}	σ_{IS}
5	0.0061	0.0024
10	0.0059	0.0023
15	0.0056	0.002
30	0.0054	0.002
45	0.0056	0.0018

Table 5.4: Contrast metrics of the three-dimensional model obtained by matched-guided filtering with the filter banks created at different angular resolutions

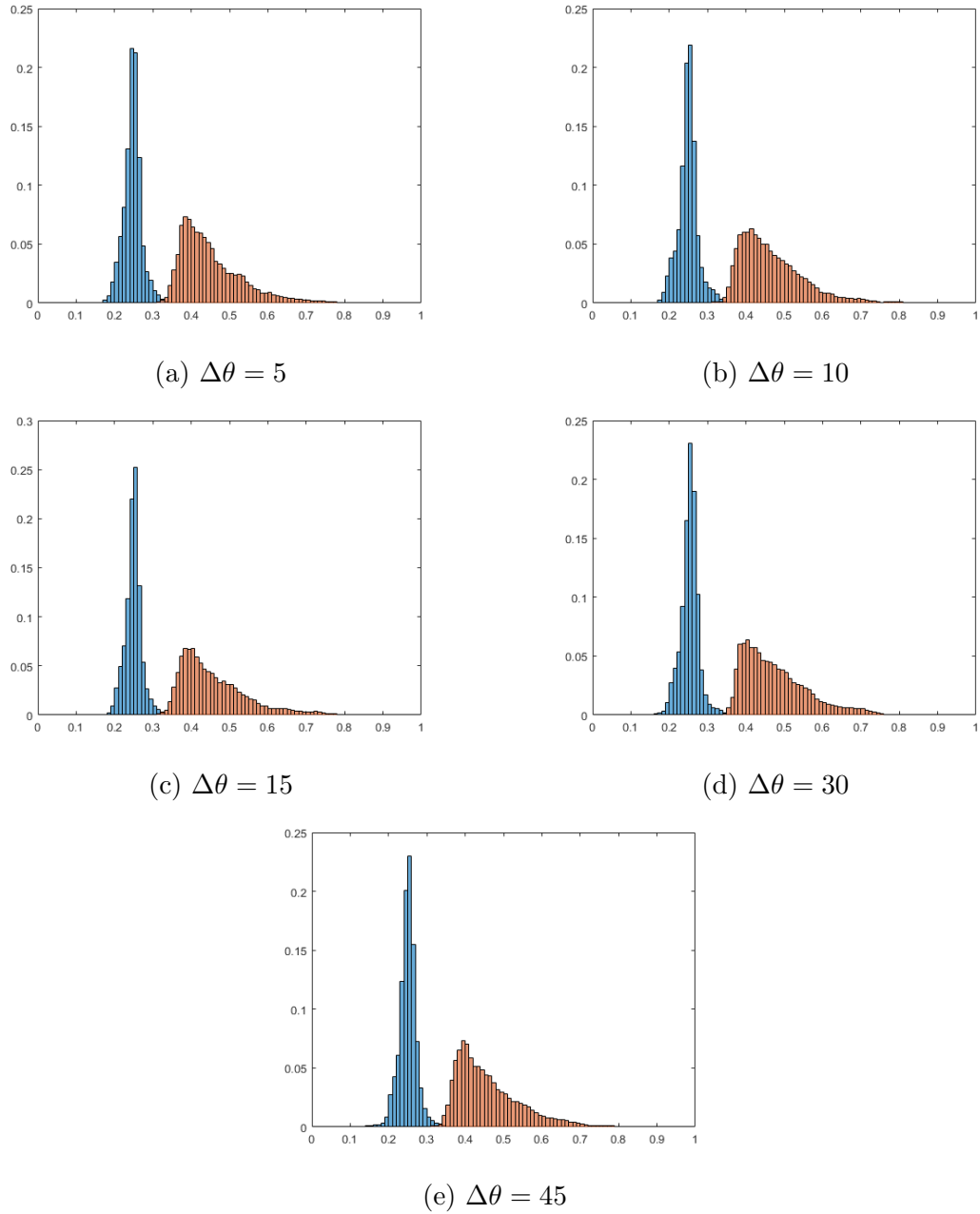


Figure 5.27: Probability density functions of voxel intensities corresponding to the root (orange) and background (blue) in the three-dimensional models obtained with various filter banks. ⁷⁵

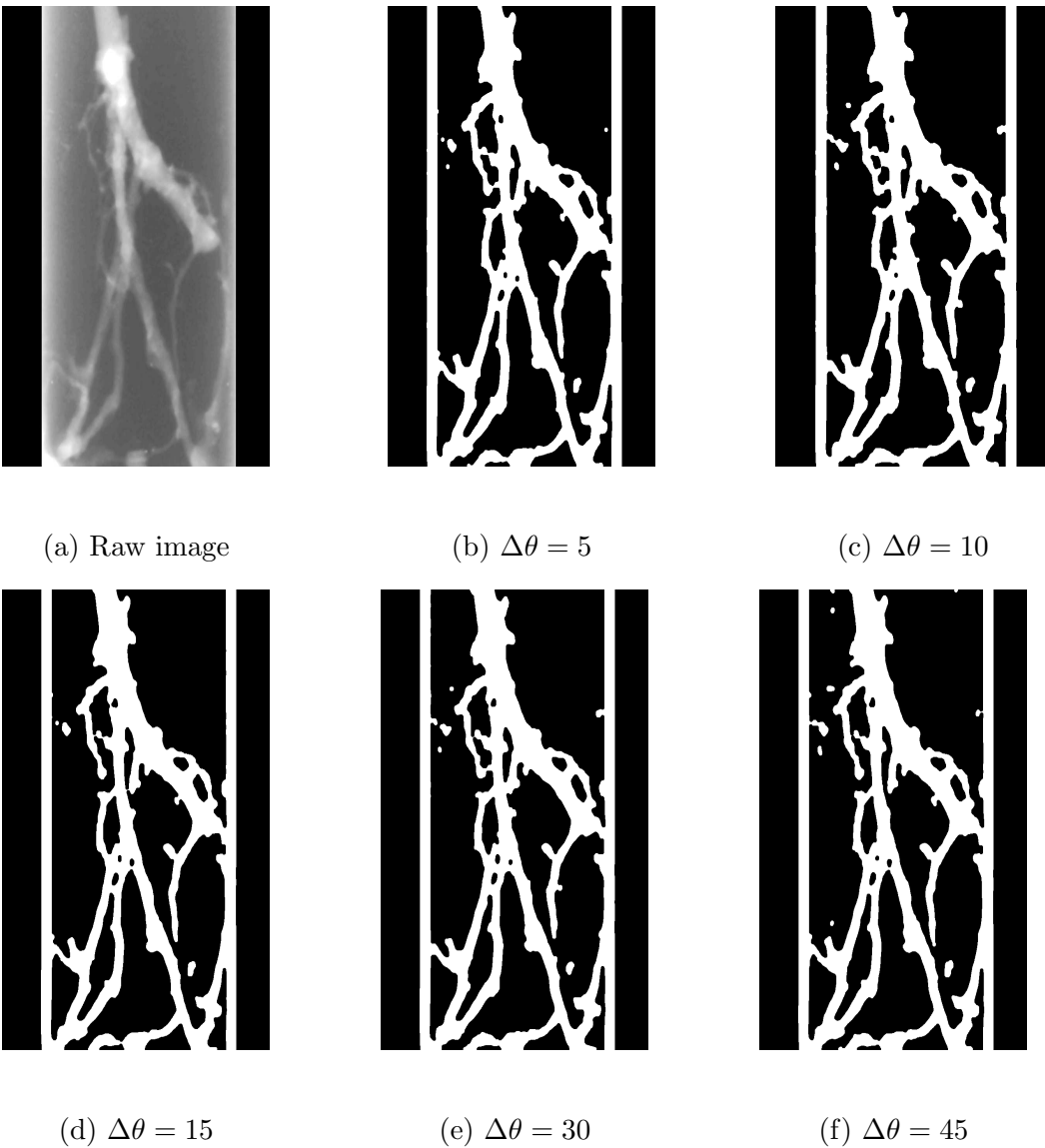


Figure 5.28: Binary masks obtained by thresholding the enhanced images from various filter banks.

The mask generation step of the matched-guided filtering decides the resultant three-dimensional model. The angular resolution employed and the manual threshold chosen affects the quality of the mask. In our experiments, the threshold values at various values at various angular resolutions are selected in a way that the foreground includes most of the RSA. Figure 5.28 presents the masks obtained at different angular resolutions. It is visible that the binary images look almost identical, giving rise to

the generation of similar contrast measures in the three-dimensional models. Hence, the proposed matched-guided filtering is robust against the angular resolution chosen for matched filtering.

Soil sample

The soil sample dataset is used in this experiment. A filter bank consisting of two-dimensional Gaussians of different scales and orientations is created for each angular resolution ($\Delta\theta$) considered. The number of filters in each filter bank depends on the angular resolution employed. A filter bank created at an angular resolution of $\Delta\theta = 5^\circ$ consists of 36 filters per scale (σ) and the filter bank created at an angular resolution $\Delta\theta = 45^\circ$ consists of 4 filters per scale (σ). The minimum scale (σ_{min}), and maximum scale (σ_{max}) for an image are set to half of the width of the thinnest and thickest roots present in the image respectively, while the scale resolution ($\Delta\sigma$) is set to 5. The filters assumed a fixed length, L , of 11 pixels.

The images in the soil sample dataset were enhanced with the 5 filter banks. For an input image, multi-scale matched filtering with the 5 filter banks produces an enhanced image per filter bank. The enhanced images are compared with manual segmentation result to draw ROC curves and provide a quantitative measure for the enhancement achieved with different filter banks. Figures 5.30, 5.31, and 5.32 presents the ROC curves drawn for the entire image set. The ROC curves corresponding to an image look similar. Table 5.5 presents the AUCs obtained for the whole image set with different filter banks. The AUCs corresponding to a plant root does not change much with an increase in angular resolution. Even, visualizing the enhanced images showed that changing the filter lengths does not have a qualitative effect. Figure 5.38 presents an example plant root image, collected with topsoil as imaging media at 30kV X-ray energy level, enhanced with the five filter banks. It can be seen that the enhanced images obtained from the five filter banks look indistinguishable. The

identical ROC curves, similar enhanced images, and comparable AUC values indicate that the proposed multi-scale matched filtering method is robust against the angular resolution chosen.

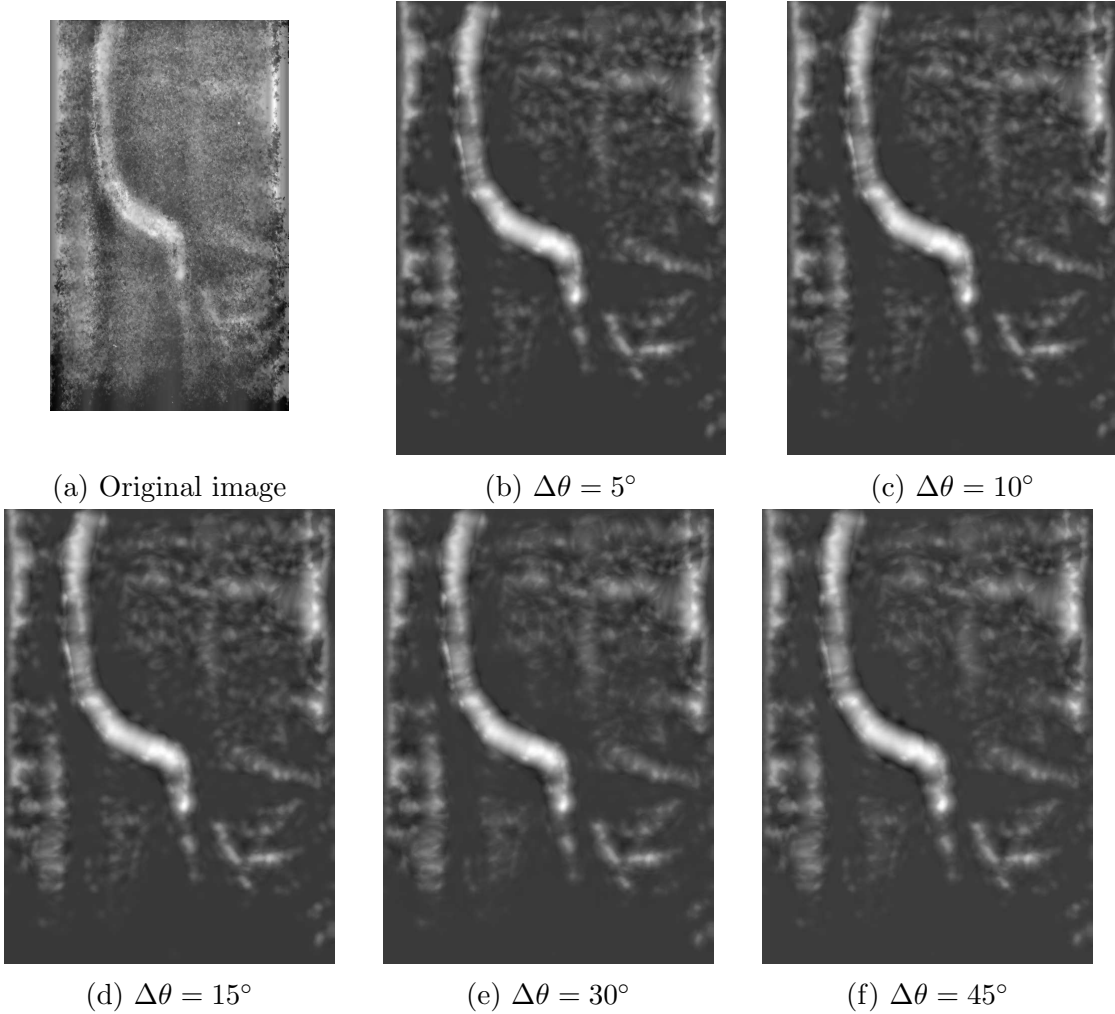


Figure 5.29: A top soil image enhanced through multi-scale matching with the filter banks consisting of filters created at various angular resolution.

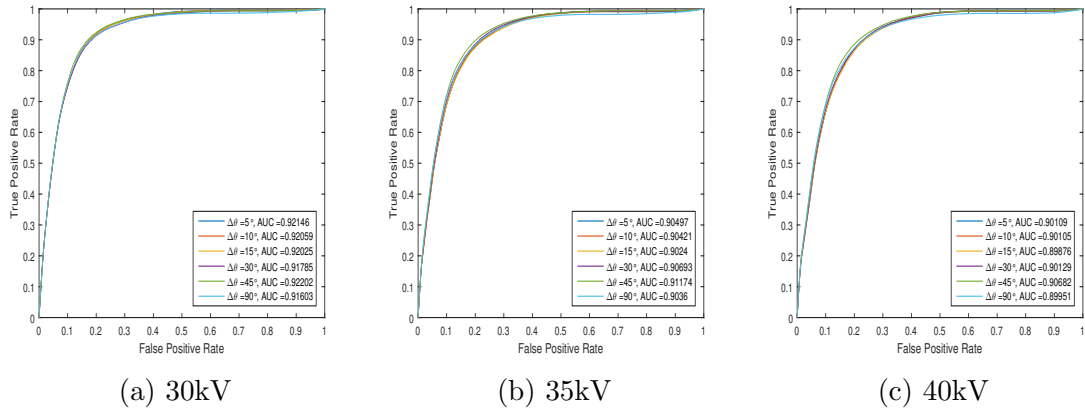


Figure 5.30: ROC curves corresponding to top soil images enhanced with the filter banks created at various angular resolution.

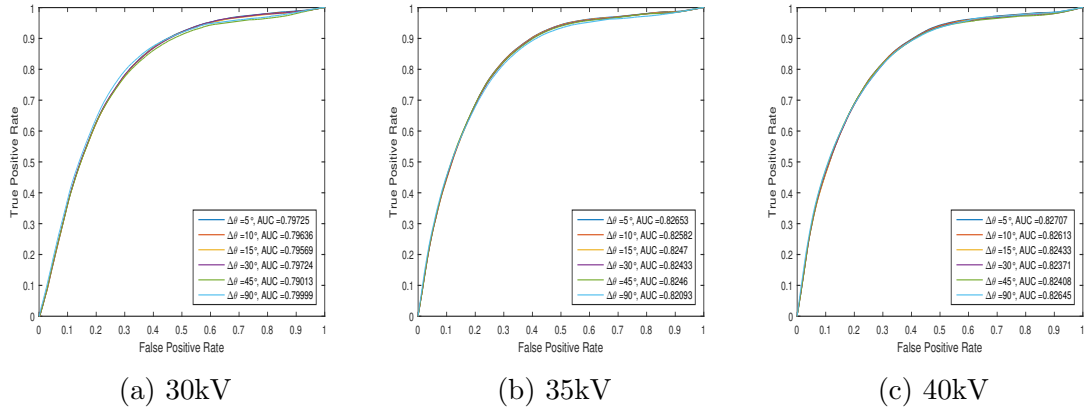


Figure 5.31: ROC curves corresponding to rolling bottom soil images enhanced with the filter banks created at various angular resolution.

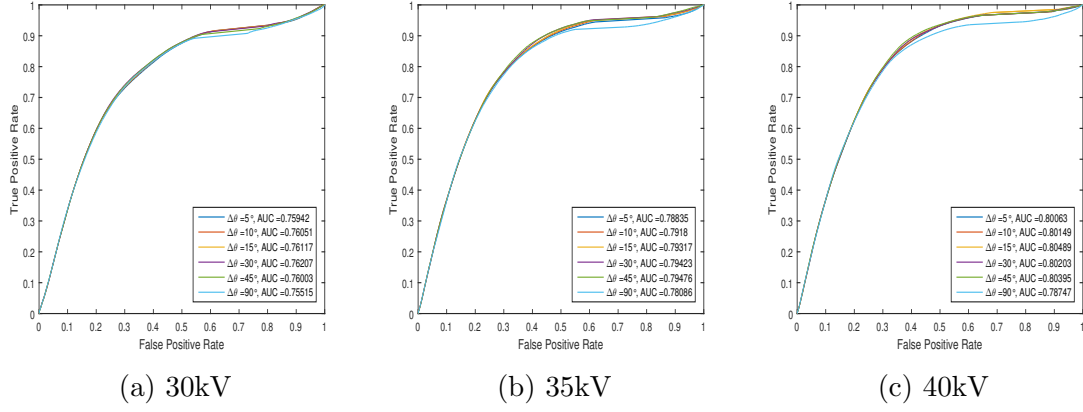


Figure 5.32: ROC curves corresponding to filtered field soil images enhanced with the filter banks created at various angular resolution.

Soil Type	Energy Level	Area under the curve (AUC)				
		$\Delta\theta = 5^\circ$	$\Delta\theta = 10^\circ$	$\Delta\theta = 15^\circ$	$\Delta\theta = 30^\circ$	$\Delta\theta = 45^\circ$
Top Soil	30kV	0.921	0.921	0.920	0.918	0.922
	35kV	0.905	0.904	0.902	0.907	0.912
	40kV	0.901	0.901	0.900	0.901	0.907
Rolling Bottom Soil	30kV	0.797	0.796	0.796	0.797	0.790
	35kV	0.826	0.826	0.825	0.824	0.825
	40kV	0.827	0.826	0.824	0.823	0.824
Filtered Field Soil	30kV	0.760	0.760	0.761	0.762	0.760
	35kV	0.788	0.792	0.793	0.794	0.795
	40kV	0.800	0.801	0.805	0.802	0.804

Table 5.5: Area under the ROC curve for the soil sample data obtained from the images enhanced through multi-scale matched filtering with the filter banks created at different angular resolution.

The results from changing the angular resolution experiments on the air sample and the soil sample datasets have shown that the performance of the proposed matched-guided filtering and multi-scale matched filtering methods is robust against the angular resolution chosen. The number of orientational filters per scale can be as few as 4, i.e., an angular resolution, $\Delta\theta$, of 45° .

5.2.2 Changing filter length (L)

In this set of experiments, the effect of changing the filter length (L) on RSA enhancement is studied. Filter lengths 5, 11, 21, 31, and 41 are considered for template matching in matched guided filtering and multi-scale matched filtering, while the standard deviation ($\sigma, \sigma_{min}, \sigma_{max}, \Delta\sigma$) and angular resolution($\Delta\theta$) assumed constant values for the whole image set corresponding to a plant. The following subsection provides the results of experiments on plant root image datasets collected with air and soil as imaging media.

Air sample

The air sample data set is used in this experiment. Matched-guided filtering is applied to the image set with five filter banks. Each filter bank consists of filters of a specific length, L , where $L \in \{5, 11, 21, 31, 41\}$. The filters are of different orientations. The angular resolution is set to 30° the standard deviation (σ) of the Gaussian is set to 9. A three-dimensional model for every filter length under consideration is generated by applying matched-guided filtering with the corresponding filter bank followed by a filtered back projection step. The contrast measure (Equation 5.1) is calculated from the three-dimensional models obtained with different filter banks. Five hundred voxels cubes of size $5 \times 5 \times 5$ belonging to the root and the background are randomly sampled to obtain the contrast measure. The sampling process is repeated a hundred times to obtain an estimate of the contrast measure. Due to the same reason mentioned in Section 5.2.1, the three-dimensional model generated in the performance evaluation section (Section 5.1.1) is considered as a reference in deciding the voxels belonging to the root and the background in this experiment. Table 5.6 presents the mean(μ_{IS}) and standard deviations (σ_{IS}) of the contrast measures obtained from different three-dimensional models. It is observable that the contrast measures does not vary significantly. Figure 5.33 presents the voxel intensity PDFs belonging to the

root and the background. It is noticeable that the PDFs look similar. However, it is noticeable from the refined mask images (Figure 5.34) that some of the root segments' intensity is spread into the background (see the halo around the root segments). The spreading of roots' intensity into the background has increased with an increase in filter length.

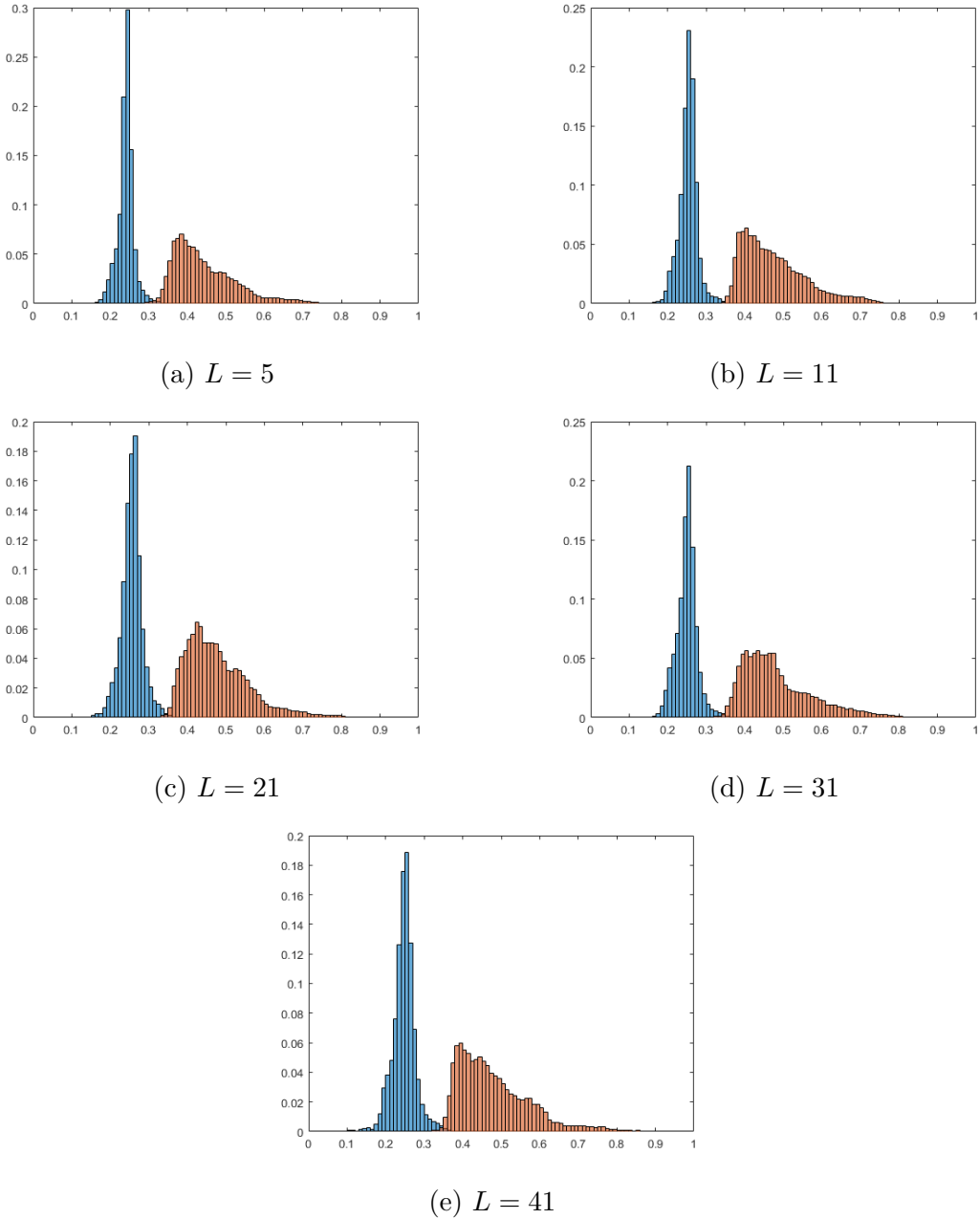


Figure 5.33: Probability density functions of voxel intensities corresponding to the root (*orange*) and background (*blue*) in the three-dimensional models obtained with various filter banks.

Filter length (L)	μ_{IS}	σ_{IS}
5	0.008	0.0031
11	0.0035	0.0017
21	0.007	0.0024
31	0.009	0.0029
41	0.008	0.0025

Table 5.6: Contrast metrics between the root and non-root from the models obtained with various filter banks.

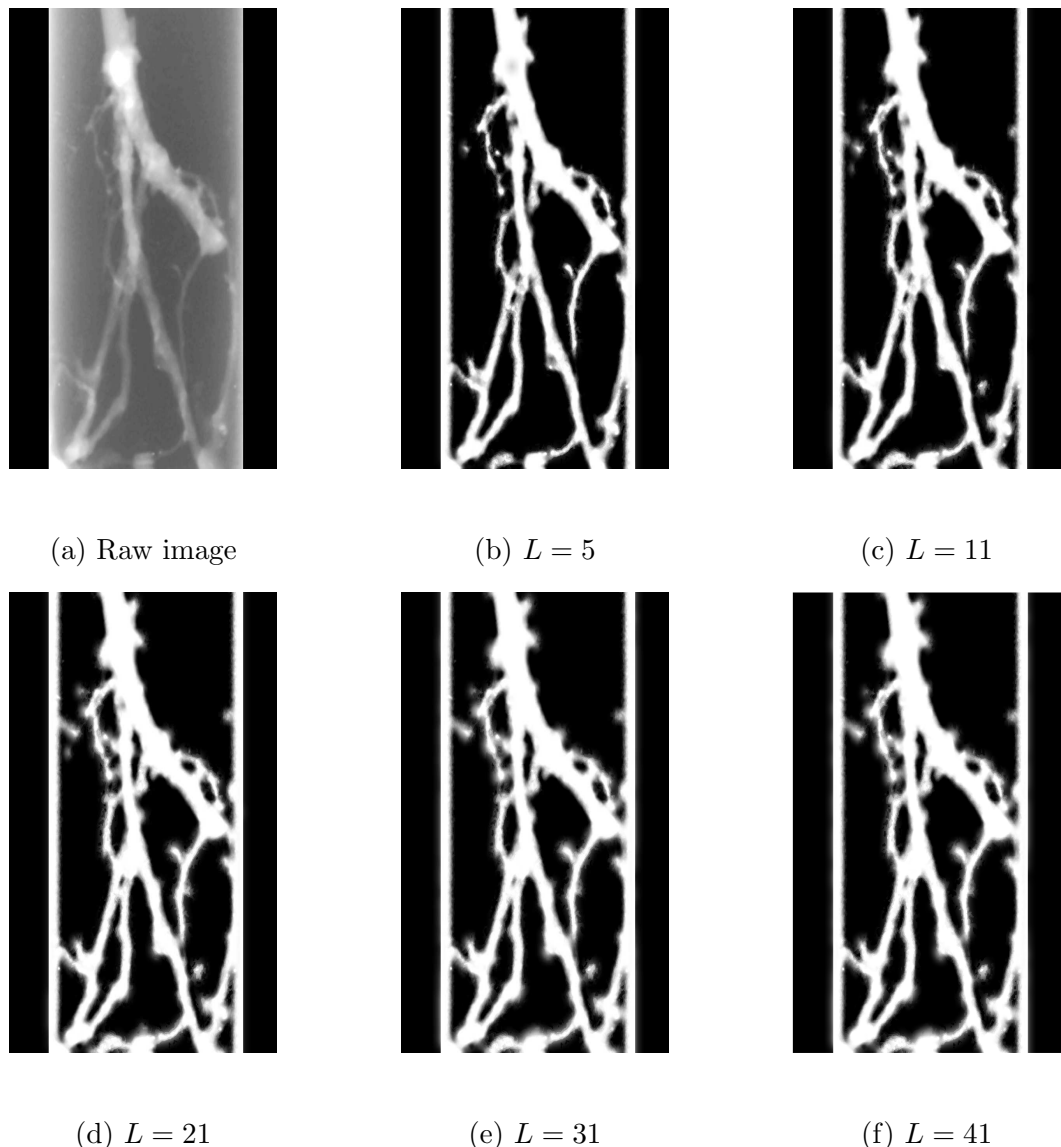


Figure 5.34: Result of structure transferring the images enhanced with various filter banks.

Filter length (L)	Average background intensity	Average root intensity
5	0.3053	0.4454
11	0.3102	0.4472
21	0.3591	0.4589
31	0.3619	0.4589
41	0.3670	0.4553

Table 5.7: Average voxel intensities of the root and background cylindrical volume of width 5 voxels around the root for various filter banks consisting of filters with length L .

As mentioned above, changing the filter length has affected the voxels around the root segments. To demonstrate the effect of varying filter length the average intensity of a cylindrical volume of 5 voxel width around the root segments was calculated. Table 5.7 the average intensities of roots and background around the roots. It is noticeable from the table that the average background voxel intensities around the root have increased with an increase in the filter length. Thus, thresholding in three-dimensions to extract the RSA might classify some of the background voxels as root and increase the noise. Hence, filters of small length are preferred.

Soil sample

In this experiment, multi-scale matched filtering is applied to the soil sample dataset with four filter banks. Each filter bank consists of filters of a specific length, L , where $L \in \{11, 21, 31, 41\}$. The filters are of different scales (σ) and orientations. The angular resolution is set to 30° . The minimum scale (σ_{min}), and maximum scale (σ_{max}) for an image are set to half of the width of the thin and thick roots present in the image respectively, while the scale resolution ($\Delta\sigma$) is set to 5. The images in the dataset were enhanced with the four filter banks. For an input image, multi-scale matched filtering with the four filter banks produces an enhanced image per filter bank. The enhanced images are compared with manually-labeled images to draw ROC curves and provide a quantitative measure for the enhancement achieved with

different filter banks. Figures 5.35, 5.36, and 5.37 presents the ROC curves drawn for the entire image set. The ROC curves corresponding to an image look similar, the AUCs does not differ much (Table 5.8). It gives an opinion that changing the filter length does not have any effect on the enhancement achieved. However, visualizing the enhanced images showed that changing the filter lengths have a quantitative effect. Figure 5.38 presents an example plant root image collected in rolling bottom soil enhanced with the filter banks. The enhanced image from the filter banks consisting of large length filters appears smooth. The noise and root details are smoothed. On the other hand, enhanced images from the filter bank consisting of small length filters preserved the root details (edges) along with the noise.

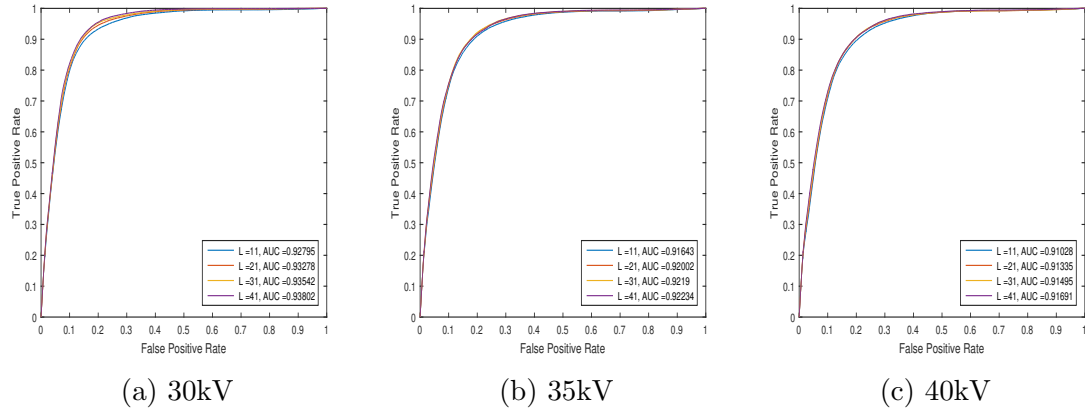


Figure 5.35: ROC curves pertaining to top soil images enhanced with various filter banks.

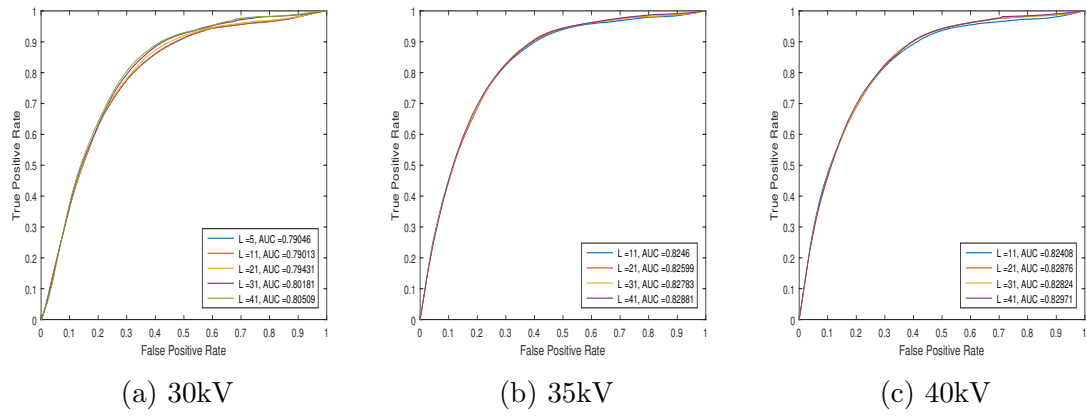


Figure 5.36: ROC curves related to rolling bottom soil images enhanced with various filter banks.

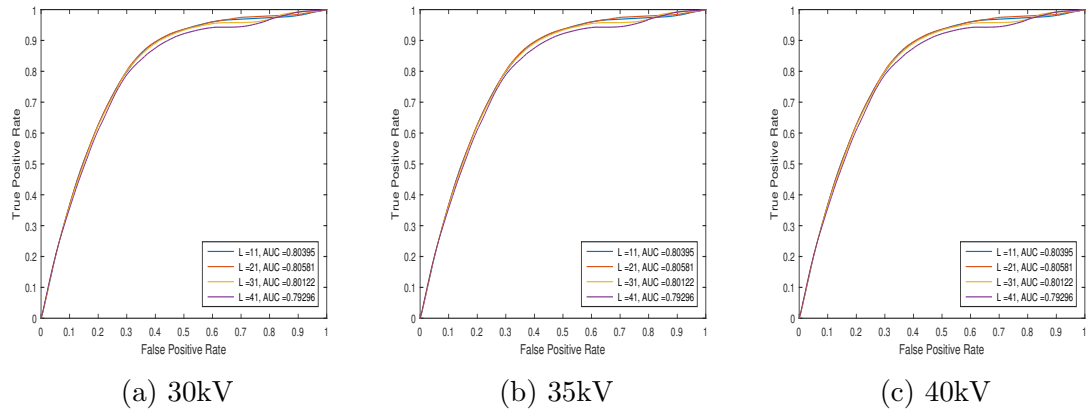


Figure 5.37: ROC curves corresponding to filtered field soil images enhanced with various filter banks.

Soil Type	Energy Level	Area under the curve (AUC)			
		$L = 11$	$L = 21$	$L = 31$	$L = 41$
Top Soil	30kV	0.928	0.932	0.935	0.938
	35kV	0.916	0.920	0.922	0.922
	40kV	0.910	0.913	0.915	0.917
Rolling Bottom Soil	30kV	0.790	0.794	0.801	0.805
	35kV	0.825	0.826	0.827	0.828
	40kV	0.824	0.828	0.828	0.829
Filtered Field Soil	30kV	0.804	0.805	0.801	0.793
	35kV	0.804	0.805	0.801	0.793
	40kV	0.804	0.805	0.801	0.793

Table 5.8: Area under the ROC curve for complete image set enhanced with different filter banks.

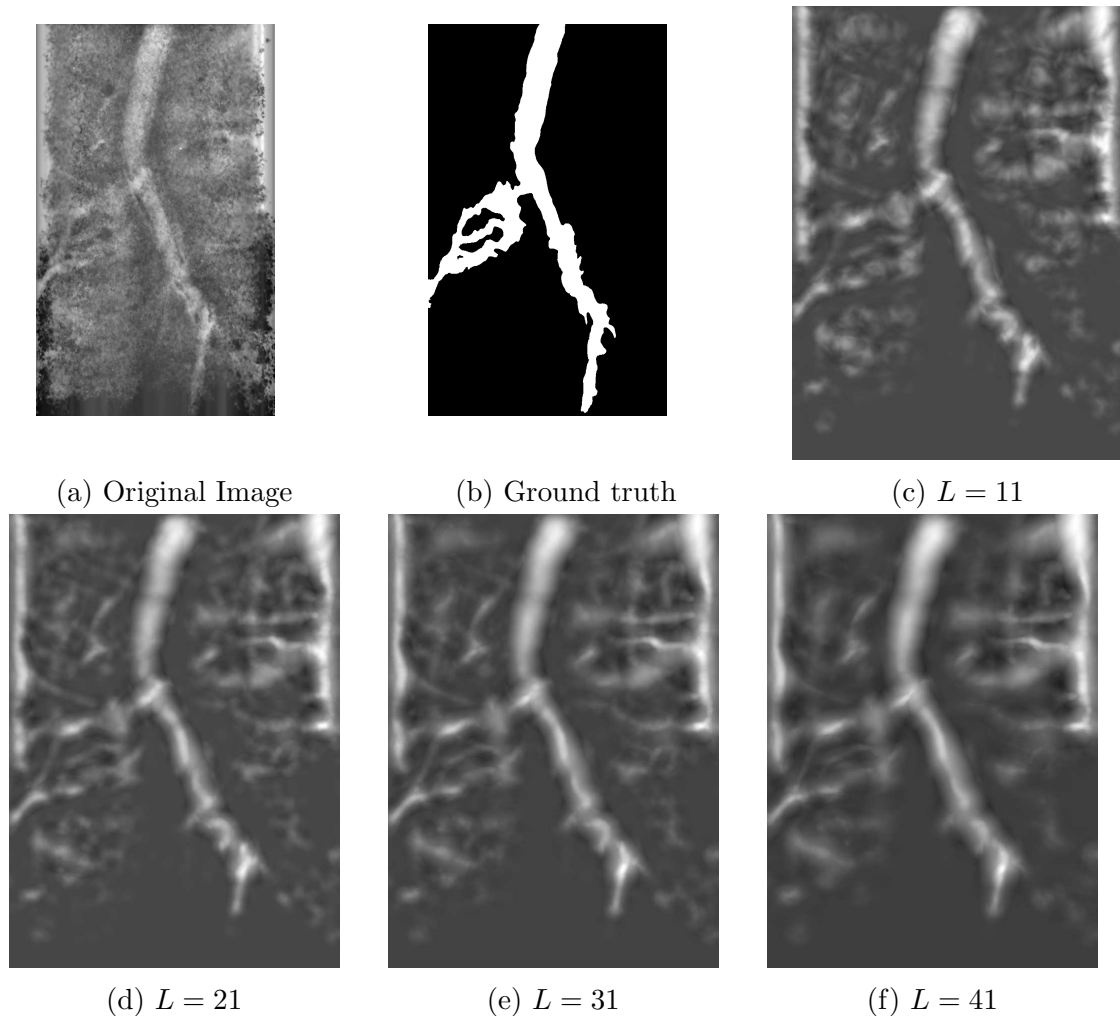


Figure 5.38: An image enhanced through multi-scale matched filtering with the filter banks consisting filters of various lengths (L)

Each filter in the filter bank is a two-dimensional Gaussian filter, convolving an image with a Gaussian smoothens the image by spreading the intensity of a pixel over its neighborhood. The degree of smoothing increases with an increase in the neighborhood size. In the case of multi-scaled matched filtering, the neighborhood size of a filter is dependent on the filter length (Equation 3.11). Filters with large length (L) have a large neighborhood, whereas the filters with small length have a small neighborhood size. Convolving with large filters produced an over smoothed version of the input image, in which noise was suppressed, root details were blurred. The noise suppression resulted in the reduction of false positives (FPs), whereas spreading the roots' intensity into background has increased the intensity of soil pixels around the root segments, hence increasing FPs. Smaller filters did not produce an over-smoothed image due to its small neighborhood. The noise was retained along with the root details in the enhanced images. The retained noise resulted in more FPs, while preserved root details reduced FPs. To illustrate the effect of changing FPs in the root and noise regions each image is divided into a root region and non-root region. The root region includes the root and the area within the 15px width from the root edges, while the rest of the image is considered as the non-root region. The ground truth images are morphologically dilated with a disk of radius 15px to obtain the root region (Figure 5.39b). The enhanced images (Figure 5.38) obtained from different filter banks were thresholded with the values that resulted in a point (0.3, 0.8) on the ROC curves (Figure 5.36a). Figure 5.40 presents the resulted binary images. The images are color-coded to demonstrate the effects of filter length. Green represents the true positives, and red represents the false positives in the root regions, dark brown represents the false positives in the non-root region, and light brown represents the classified negative pixels. The color-coded image at small filter lengths ($L = 11$) have few FPs around root segments (colored red), the number of FPs around the root has increased with an increase in the filter length. Whereas, the FPs in the

L	30kV			35kV			40kV		
	FPNR	% FPNR	FPAR	FPNR	% FPNR	FPAR	FPNR	% FPNR	FPAR
11	130927	24.39	11409	131793	24.55	11087	132098	24.61	10986
21	129674	24.16	12503	130725	24.35	11875	131415	24.48	11431
31	128547	23.95	13587	130576	24.33	12084	131353	24.47	11599
41	127604	23.77	14456	130154	24.25	12413	130842	24.38	11997

Table 5.9: False positives count in the root and non-root regions for the top soil images at FPR = 0.3

non-root region reduced with an increase in filter length ($L = 41$). Tables 5.9, 5.10, and 5.10 presents the false positives around roots (FPAR), and false positives around non-root regions (FPNR) obtained for the whole image set. It can be seen from the tables that, FPAR increases with an increase in filter length for all images, whereas, the FPNR decreases with an increase in filter length. Overall, the increase in FPs around the root compensated the decrease in FPs in non-root regions at large values of L. The decrease in FPs around the root region compensated the increase in FPs around non-root region at small values of L.

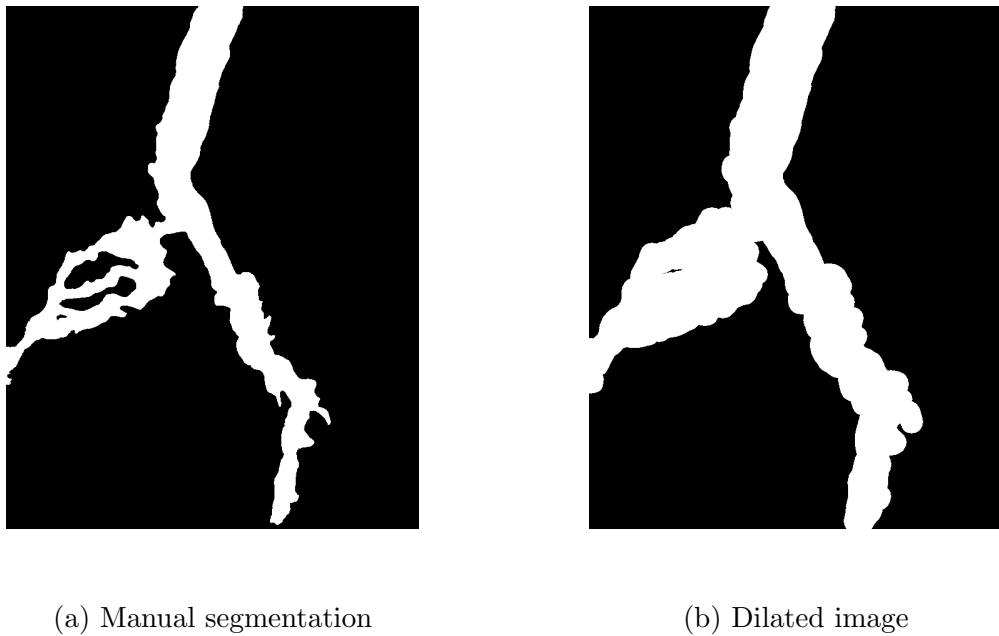


Figure 5.39: An example of manually segmented image and corresponding root and non-root regions obtained by dilating with a disk of radius 15px.

L	30kV			35kV			40kV		
	FPNR	% FPNR	FPAR	FPNR	% FPNR	FPAR	FPNR	% FPNR	FPAR
11	110553	23.63	7224	105111	22.47	10079	103984	22.23	11093
21	109104	23.32	8365	103137	22.04	11446	103236	22.07	11520
31	106888	22.85	10054	102336	21.87	12210	102628	21.94	12197
41	104378	22.31	11887	102380	21.88	12607	103082	22.03	12266

Table 5.10: False positives count in the root and non-root regions for the rolling bottom soil images at FPR = 0.3.

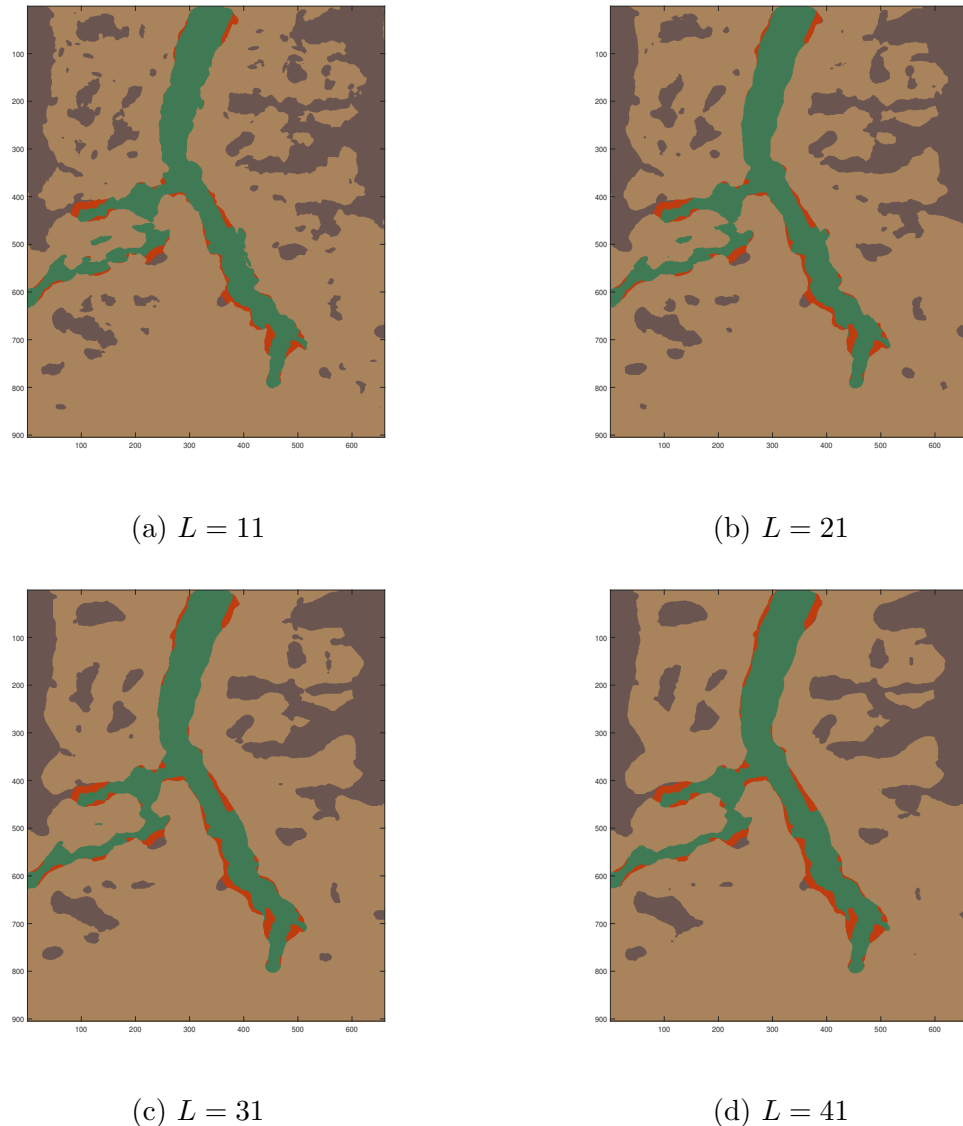


Figure 5.40: Color-coded binary images, representing true positives (green), false positives in the root (red) and non-root regions (dark brown), and classified negatives (light brown), obtained through thresholding.

<i>L</i>	30kV			35kV			40kV		
	FPNR	% FPNR	FPAR	FPNR	% FPNR	FPAR	FPNR	% FPNR	FPAR
11	78313	19.32	11020	71679	17.68	13525	71119	17.54	13432
21	75558	18.64	13199	69063	17.03	15560	68431	16.88	15367
31	74147	18.29	16816	66975	16.52	17952	65596	16.18	18204
41	73762	18.19	18335	66510	16.40	19690	64829	15.99	20220

Table 5.11: False positives count in the root and non-root regions for the filtered field soil images at FPR = 0.3.

The results from changing the filter length experiments on the air sample and the soil sample datasets have shown that the performance of the proposed matched-guided filtering and multi-scale matched filtering methods is sensitive to the choice of the filter length. Increasing the filter length has resulted in an increase in the misclassification of background pixels as root pixels. On the other hand, filters of small length did not suppress the noise and increased the false positives. However, such noise is eliminated in the post-processing phase. Thus reducing the misclassification around the root is of prime importance to obtain an accurate root structure. Hence, filters with small length (L) are preferred.

Chapter 6

Summary and concluding remarks

In this study, two methods are proposed to process plant root images acquired using an inexpensive lab-built X-ray system operating at low energy levels. Air, topsoil, Haymond silt loam soil (rolling bottom soil), and soil from the local field are used as imaging media. For the image set acquired with air as an imaging medium, the proposed matched-guided filtering enhances the roots and improve contrast between the root system and background. Additionally, a filtered back projection step is included to generate a three-dimensional model. For the image set obtained with soil as an imaging medium, the proposed multi-scale matched filtering enhances and isolates root segments.

To evaluate the accuracy of our three-dimensional reconstruction, we tried to compare it with the three-dimensional model obtained from RooTrak's tracking approach. However, RooTrak could not extract the root segments owing to the quality of low energy X-ray images. Considering that the contrast enhancement between root segments and the background is the core part of the proposed matched-guided filtering, we calculated contrast metrics from our three-dimensional model and the one obtained from the filtered back projection of raw images. It is found that the model obtained with matched-guided filtering has superior contrast metrics. For the

image set collected in the soil, we compared our root segmentation results with Otsu's segmentation approach. It is found that the proposed multi-scale matched filtering has a better F_1 score compared to Otsu's method.

Future directions for improving the proposed system include refining the three-dimensional model, and using better approaches to evaluate the accuracy of the model, and bettering the segmentation result of soil samples. Some portion of root segments is lost due to the lack of clear separation between the root edges and the container edges. Imaging the plant roots in a bigger container could avoid this problem and improves the amount of recovered root. To better evaluate the accuracy of the obtained three-dimensional model, we could extract phenotypical features from it and compare them against the manually measured traits. Reducing the porosity formation while filling the soil into the container would produce better images where the roots and soil differ in their attenuation values, could improve the segmentation result.

Bibliography

- [1] Suqin Fang, Xiaolong Yan, and Hong Liao. 3d reconstruction and dynamic modeling of root architecture in situ and its application to crop phosphorus research. *The Plant Journal*, 60(6):1096–1108, 2009.
- [2] Ying Zheng, Steve Gu, Herbert Edelsbrunner, Carlo Tomasi, and Philip Benfey. Detailed reconstruction of 3d plant root shape. In *Computer Vision (ICCV), 2011 IEEE International Conference on*, pages 2026–2033. IEEE, 2011.
- [3] Miguel A Piñeros, Brandon G Larson, Jon E Shaff, David J Schneider, Alexandre Xavier Falcão, Lixing Yuan, Randy T Clark, Eric J Craft, Tyler W Davis, Pierre-Luc Pradier, et al. Evolving technologies for growing, imaging and analyzing 3d root system architecture of crop plants. *Journal of integrative plant biology*, 58(3):230–241, 2016.
- [4] Patrick Armengaud, Kevin Zambaux, Adrian Hills, Ronan Sulpice, Richard J Pattison, Michael R Blatt, and Anna Amtmann. Ez-rhizo: integrated software for the fast and accurate measurement of root system architecture. *The Plant Journal*, 57(5):945–956, 2009.
- [5] Anjali S Iyer-Pascuzzi, Olga Symonova, Yuriy Mileyko, Yueling Hao, Heather Belcher, John Harer, Joshua S Weitz, and Philip N Benfey. Imaging and analysis platform for automatic phenotyping and trait ranking of plant root systems. *Plant physiology*, 152(3):1148–1157, 2010.
95

- [6] Michael P Pound, Andrew P French, Jonathan A Atkinson, Darren M Wells, Malcolm J Bennett, and Tony Pridmore. Rootnav: navigating images of complex root architectures. *Plant Physiology*, 162(4):1802–1814, 2013.
- [7] MG Johnson, DT Tingey, DL Phillips, and MJ Storm. Advancing fine root research with minirhizotrons. *Environmental and Experimental Botany*, 45(3):263–289, 2001.
- [8] Melinda Lontoc-Roy, Pierre Dutilleul, Shiv O Prasher, Liwen Han, and Donald L Smith. Computed tomography scanning for three-dimensional imaging and complexity analysis of developing root systems. *Botany*, 83(11):1434–1442, 2005.
- [9] Sacha J Mooney, Tony P Pridmore, Jonathan Helliwell, and Malcolm J Bennett. Developing x-ray computed tomography to non-invasively image 3-d root systems architecture in soil. *Plant and soil*, 352(1-2):1–22, 2012.
- [10] DC Bowman, DA Devitt, MC Engelke, and TW Rufty. Root architecture affects nitrate leaching from bentgrass turf. *Crop Science*, 38(6):1633–1639, 1998.
- [11] Claude Doussan, Loïc Pagès, and Gilles Vercambre. Modelling of the hydraulic architecture of root systems: an integrated approach to water absorptionmodel description. *Annals of botany*, 81(2):213–223, 1998.
- [12] Hong Liao, Zhenyang Ge, and Xiaolong Yan. Ideal root architecture for phosphorus acquisition of plants under water and phosphorus coupled stresses: from simulation to application. *Chinese Science Bulletin*, 46(16):1346–1351, 2001.
- [13] Hans Lambers, Michael W Shane, Michael D Cramer, Stuart J Pearse, and Erik J Veneklaas. Root structure and functioning for efficient acquisition of phosphorus: matching morphological and physiological traits. *Annals of botany*, 98(4):693–713, 2006.

- [14] Todd H Skaggs and Peter J Shouse. Roots and root function: introduction. *Vadose Zone Journal*, 7(3):1008–1009, 2008.
- [15] Y Al-Ghazi, B Muller, S Pinloche, TJ Tranbarger, P Nacry, M Rossignol, F Tardieu, and P Doumas. Temporal responses of arabidopsis root architecture to phosphate starvation: evidence for the involvement of auxin signalling. *Plant, Cell & Environment*, 26(7):1053–1066, 2003.
- [16] DE Miller. Root systems in relation to stress tolerance. *HortScience*, 21(4):963–970, 1986.
- [17] Melinda Lontoc-Roy, Pierre Dutilleul, Shiv O Prasher, Liwen Han, Thomas Brouillet, and Donald L Smith. Advances in the acquisition and analysis of ct scan data to isolate a crop root system from the soil medium and quantify root system complexity in 3-d space. *Geoderma*, 137(1):231–241, 2006.
- [18] Pankaj Kumar, Jinhai Cai, and Stan Miklavcic. 3d reconstruction, modelling and analysis of in situ root system architecture. In *Proceedings of the 20th international congress on modelling and simulation (MODSIM2013)*, 2013.
- [19] Guillaume Lobet, Loïc Pagès, and Xavier Draye. A novel image-analysis toolbox enabling quantitative analysis of root system architecture. *Plant physiology*, 157(1):29–39, 2011.
- [20] Randy T Clark, Robert B MacCurdy, Janelle K Jung, Jon E Shaff, Susan R McCouch, Daniel J Aneshansley, and Leon V Kochian. Three-dimensional root phenotyping with a novel imaging and software platform. *Plant physiology*, 156(2):455–465, 2011.
- [21] Kai L Nielsen, Jonathan P Lynch, and Howard N Weiss. Fractal geometry of bean root systems: correlations between spatial and fractal dimension. *American Journal of Botany*, pages 26–33, 1997

- [22] Carlos Costa, Lianne M Dwyer, Pierre Dutilleul, Kayhan Foroutan-pour, Aiguo Liu, Chantal Hamel, and Donald L Smith. Morphology and fractal dimension of root systems of maize hybrids bearing the leafy trait. *Canadian journal of botany*, 81(7):706–713, 2003.
- [23] Deo A Heeraman, Jan W Hopmans, and Volker Clausnitzer. Three dimensional imaging of plant roots in situ with x-ray computed tomography. *Plant and Soil*, 189(2):167–179, 1997.
- [24] Alain Pierret, Yvan Capowiez, Christopher J Moran, and André Kretzschmar. X-ray computed tomography to quantify tree rooting spatial distributions. *Geoderma*, 90(3):307–326, 1999.
- [25] Sacha Jon Mooney. Three-dimensional visualization and quantification of soil macroporosity and water flow patterns using computed tomography. *Soil Use and Management*, 18(2):142–151, 2002.
- [26] PJ Gregory, DJ Hutchison, DB Read, PM Jenneson, WB Gilboy, and EJ Morton. Non-invasive imaging of roots with high resolution x-ray micro-tomography. In *Roots: The Dynamic Interface between Plants and the Earth*, pages 351–359. Springer, 2003.
- [27] Anders Kaestner, Martin Schneebeli, and Frank Graf. Visualizing three-dimensional root networks using computed tomography. *Geoderma*, 136(1):459–469, 2006.
- [28] JS Perret, ME Al-Belushi, and M Deadman. Non-destructive visualization and quantification of roots using computed tomography. *Soil Biology and Biochemistry*, 39(2):391–399, 2007.
- [29] Saoirse R Tracy, Jeremy A Roberts, Colin R Black, Ann McNeill, Rob Davidson, and Sacha J Mooney. The x-factor: visualizing undisturbed root architec-

- ture in soils using x-ray computed tomography. *Journal of experimental botany*, 61(2):311–313, 2010.
- [30] Ahmad B Moradi, Andrea Carminati, Doris Vetterlein, Peter Vontobel, Eberhard Lehmann, Ulrich Weller, Jan W Hopmans, Hans-Jörg Vogel, and Sascha E Oswald. Three-dimensional visualization and quantification of water content in the rhizosphere. *New Phytologist*, 192(3):653–663, 2011.
- [31] Saoirse R Tracy, Colin R Black, Jeremy A Roberts, Craig Sturrock, Stefan Mairhofer, Jim Craigon, and Sacha J Mooney. Quantifying the impact of soil compaction on root system architecture in tomato (*solanum lycopersicum*) by x-ray micro-computed tomography. *Annals of Botany*, 110(2):511–519, 2012.
- [32] Stefan Mairhofer, Susan Zappala, Saoirse R Tracy, Craig Sturrock, Malcolm Bennett, Sacha J Mooney, and Tony Pridmore. Rootrak: automated recovery of three-dimensional plant root architecture in soil from x-ray microcomputed tomography images using visual tracking. *Plant physiology*, 158(2):561–569, 2012.
- [33] Stefan Mairhofer, Susan Zappala, Saoirse Tracy, Craig Sturrock, Malcolm John Bennett, Sacha Jon Mooney, and Tony Paul Pridmore. Recovering complete plant root system architectures from soil via x-ray μ -computed tomography. *Plant Methods*, 9(1):8, 2013.
- [34] Nicolai Koebernick, Ulrich Weller, Katrin Huber, Steffen Schlüter, Hans-Jörg Vogel, Reinhold Jahn, Harry Vereecken, and Doris Vetterlein. In situ visualization and quantification of three-dimensional root system architecture and growth using x-ray computed tomography. *Vadose Zone Journal*, 13(8), 2014.
- [35] Richard J Flavel, Chris N Guppy, Sheikh MR Rabbi, and Iain M Young. An image processing and analysis tool for identifying and analysing complex

plant root systems in 3d soil using non-destructive analysis: Root1. *PloS one*, 12(5):e0176433, 2017.

- [36] Isaac. Zachary. X-ray system property effects on plant root imaging contrast, 2018.
- [37] John C Trinder and Yandong Wang. Automatic road extraction from aerial images. *Digital Signal Processing*, 8(4):215–224, 1998.
- [38] Peter J Gregory. *Plant roots: growth, activity and interactions with the soil*. John Wiley & Sons, 2008.
- [39] Albert L Smit, A Glyn Bengough, Christof Engels, Meine van Noordwijk, Sylvain Pellerin, and SC van de Geijn. *Root methods: a handbook*. Springer Science & Business Media, 2013.
- [40] Andrew French, Susana Ubeda-Tomás, Tara J Holman, Malcolm J Bennett, and Tony Pridmore. High-throughput quantification of root growth using a novel image-analysis tool. *Plant physiology*, 150(4):1784–1795, 2009.
- [41] PL Bragg, G Govi, and RQ Cannell. A comparison of methods, including angled and vertical minirhizotrons, for studying root growth and distribution in a spring oat crop. *Plant and Soil*, 73(3):435–440, 1983.
- [42] Ronald L Hendrick and Kurt S Pregitzer. Applications of minirhizotrons to understand root function in forests and other natural ecosystems. *Plant and Soil*, 185(2):293–304, 1996.
- [43] HM Taylor, DR Upchurch, and BL McMichael. Applications and limitations of rhizotrons and minirhizotrons for root studies. *Plant and Soil*, 129(1):29–35, 1990.

- [44] Laura Stingaciu, Hannes Schulz, Andreas Pohlmeier, Sven Behnke, Herwig Zilken, Mathieu Javaux, and Harry Vereecken. In situ root system architecture extraction from magnetic resonance imaging for water uptake modeling. *Vadose zone journal*, 12(1), 2013.
- [45] James Albert Sethian. *Level set methods and fast marching methods: evolving interfaces in computational geometry, fluid mechanics, computer vision, and materials science*, volume 3. Cambridge university press, 1999.
- [46] Rafael C Gonzalez and Richard E Woods. *Digital image processing*. Upper Saddle River, NJ: Prentice Hall, 2012.
- [47] Thomas Bäck, David B Fogel, and Zbigniew Michalewicz. *Handbook of evolutionary computation*. CRC Press, 1997.
- [48] Wikipedia contributors. Genetic algorithm — Wikipedia, the free encyclopedia. https://en.wikipedia.org/w/index.php?title=Genetic_algorithm&oldid=833749342, 2018. [Online; accessed 14-June-2018].
- [49] Darrell Whitley. A genetic algorithm tutorial. *Statistics and computing*, 4(2):65–85, 1994.
- [50] Christopher R Houck, Jeff Joines, and Michael G Kay. A genetic algorithm for function optimization: a matlab implementation. *Ncsu-ie tr*, 95(09):1–10, 1995.
- [51] Wikipedia contributors. Genetic algorithm — Wikipedia, the free encyclopedia. https://en.wikipedia.org/w/index.php?title=Genetic_algorithm&oldid=849425439, 2018. [Online; accessed 13-July-2018].
- [52] James E Baker. Reducing bias and inefficiency in the selection algorithm. In *Proceedings of the second international conference on genetic algorithms*, volume 206, pages 14–21, 1987.

- [53] Tania Pencheva, Krassimir Atanassov, and Anthony Shannon. Modelling of a stochastic universal sampling selection operator in genetic algorithms using generalized nets. In *Proceedings of the Tenth International Workshop on Generalized Nets, Sofia*, pages 1–7, 2009.
- [54] Wikipedia contributors. Stochastic universal sampling — Wikipedia, the free encyclopedia. https://en.wikipedia.org/w/index.php?title=Stochastic_universal_sampling&oldid=782272950, 2017. [Online; accessed 16-June-2018].
- [55] George Turin. An introduction to matched filters. *IRE transactions on Information theory*, 6(3):311–329, 1960.
- [56] Wikipedia contributors. Matched filter — Wikipedia, the free encyclopedia. https://en.wikipedia.org/w/index.php?title=Matched_filter&oldid=841333957, 2018. [Online; accessed 18-June-2018].
- [57] Subhasis Chaudhuri, Shankar Chatterjee, Norman Katz, Mark Nelson, and Michael Goldbaum. Detection of blood vessels in retinal images using two-dimensional matched filters. *IEEE Transactions on medical imaging*, 8(3):263–269, 1989.
- [58] AD Hoover, Valentina Kouznetsova, and Michael Goldbaum. Locating blood vessels in retinal images by piecewise threshold probing of a matched filter response. *IEEE Transactions on Medical imaging*, 19(3):203–210, 2000.
- [59] Michal Sofka and Charles V Stewart. Retinal vessel centerline extraction using multiscale matched filters, confidence and edge measures. *IEEE transactions on medical imaging*, 25(12):1531–1546, 2006.
- [60] Bob Zhang, Lin Zhang, Lei Zhang, and Fakhri Karray. Retinal vessel extraction by matched filter with first-order derivative of gaussian. *Computers in biology and medicine*, 40(4):438–445, 2010.

- [61] Kaiming He, Jian Sun, and Xiaoou Tang. Guided image filtering. *IEEE transactions on pattern analysis and machine intelligence*, 35(6):1397–1409, 2013.
- [62] Zhenguo Li and Jinghong Zheng. Edge-preserving decomposition-based single image haze removal. *IEEE Transactions on Image Processing*, 24(12):5432–5441, 2015.
- [63] Qingsong Zhu, Jiaming Mai, Ling Shao, et al. A fast single image haze removal algorithm using color attenuation prior. *IEEE Trans. Image Processing*, 24(11):3522–3533, 2015.
- [64] Yuanyuan Gao, Hai-Miao Hu, Shuhang Wang, and Bo Li. A fast image dehazing algorithm based on negative correction. *Signal Processing*, 103:380–398, 2014.
- [65] Ning Xu, Brian Price, Scott Cohen, and Thomas Huang. Deep image matting. In *Computer Vision and Pattern Recognition (CVPR)*, 2017.
- [66] Rodney A Brooks and Giovanni Di Chiro. Beam hardening in x-ray reconstructive tomography. *Physics in medicine & biology*, 21(3):390, 1976.
- [67] Sarah Abdulla. Ct artefacts Radiology Cafe. <https://www.radiologycafe.com/radiology-trainees/frcr-physics-notes/ct-artefacts>, 2018. [Online; accessed 18-June-2018].
- [68] Gabor T Herman. Correction for beam hardening in computed tomography. *Physics in Medicine & Biology*, 24(1):81, 1979.
- [69] Yuranga Weerakkody and Murphy Andrew. Beam hardening — Radiopaedia. <https://radiopaedia.org/articles/beam-hardening>, 2018. [Online; accessed 18-June-2018].
- [70] Peter Kovesi. Phase preserving denoising of images. *signal*, 4(1), 1999.

- [71] Yves Meyer. *Wavelets and operators*, volume 1. Cambridge university press, 1995.
- [72] Robi Polikar. The wavelet tutorial. https://cseweb.ucsd.edu/~baden/Doc/wavelets/polikar_wavelets.pdf, 2006. [Online; accessed 12-July-2018].
- [73] Wavelet denoising. <https://www.mathworks.com/help/wavelet/ug/wavelet-denoising.html>, 2018. [Online; accessed 12-July-2018].
- [74] Wikipedia contributors. Wavelet — Wikipedia, the free encyclopedia. <https://en.wikipedia.org/w/index.php?title=Wavelet&oldid=849444747>, 2018. [Online; accessed 13-July-2018].
- [75] S Grace Chang, Bin Yu, and Martin Vetterli. Adaptive wavelet thresholding for image denoising and compression. *IEEE transactions on image processing*, 9(9):1532–1546, 2000.
- [76] Boualem Boashash. *Time-frequency signal analysis and processing: a comprehensive reference*. Academic Press, 2015.
- [77] Wikipedia contributors. Fourier transform — Wikipedia, the free encyclopedia. https://en.wikipedia.org/w/index.php?title=Fourier_transform&oldid=849527869, 2018. [Online; accessed 14-July-2018].
- [78] F Edward Boas and Dominik Fleischmann. Ct artifacts: causes and reduction techniques. *Imaging Med*, 4(2):229–240, 2012.
- [79] Bw. <https://www.mathworks.com/help/images/ref/bwconncomp.html>, 2018. [Online; accessed 12-July-2018].
- [80] David Martin Powers. Evaluation: from precision, recall and f-measure to roc, informedness, markedness and correlation. 2011.

- [81] Wikipedia contributors. Sensitivity and specificity — Wikipedia, the free encyclopedia. https://en.wikipedia.org/w/index.php?title=Sensitivity_and_specificity&oldid=843939485, 2018. [Online; accessed 6-July-2018].
- [82] Donald S Burke, John F Brundage, Robert R Redfield, James J Damato, Charles A Schable, Pamela Putman, Robert Visintine, and Howard I Kim. Measurement of the false positive rate in a screening program for human immunodeficiency virus infections. *New England Journal of Medicine*, 319(15):961–964, 1988.
- [83] Wikipedia contributors. False positive rate — Wikipedia, the free encyclopedia. https://en.wikipedia.org/w/index.php?title=False_positive_rate&oldid=811547375, 2017. [Online; accessed 6-July-2018].
- [84] Nobuyuki Otsu. A threshold selection method from gray-level histograms. *IEEE transactions on systems, man, and cybernetics*, 9(1):62–66, 1979.
- [85] Wikipedia contributors. F1 score — Wikipedia, the free encyclopedia. https://en.wikipedia.org/w/index.php?title=F1_score&oldid=841695054, 2018. [Online; accessed 6-July-2018].